

Pyrolysis oil evaporation including liquid phase polymerization reaction

S. Chantal Sital

Technical University Delft

DELFT UNIVERSITY OF TECHNOLOGY

Pyrolysis oil evaporation including liquid phase polymerization reaction

Author:

S. Chantal Sital

Supervisor:

Prof. Dr. D. J. E. M. Roekaerts

Report number:

2925

Readers:

Prof. Dr. ir. W. de Jong

Dr. ir. C. A. Infante Ferreira

*A thesis submitted in partial fulfillment of the requirements
for the degree in Master of Science in Mechanical Engineering*

Faculty of Mechanical, Maritime and Materials Engineering, Process & Energy
department

October 17, 2018

An electronic version of this thesis is available at <http://repository.tudelft.nl/>

Abstract

Pyrolysis oil (BPO), derived from biomass via the fast pyrolysis process is a potential substitute for petroleum fuels. Due to its distinct physical and chemical properties (highly oxygenated, chemically reactive), the possible range of stable and clean operation in combustion devices is smaller than for petroleum fuel and to enable use of pyrolysis oil in a wider range of applications more insight in pyrolysis heating and evaporation behaviour is required. A surrogate oil of 6 discrete components (water, acetic acid, hydroxypropanone, phenol, eugenol and levoglucosan) is formulated to represent certain aspects of the real pyrolysis oil for computational means. A liquid phase thermal polymerization reaction is formulated to investigate the effect this reaction has on the evaporation process. In this reaction, levoglucosan undergoes a dimerization reaction to form a solid dimer. For the evaporation, the Rapid Mixing Model (RMM) is applied, which (mainly) assumes infinitely fast liquid phase thermal conductivity. The RMM is adapted for the multicomponent case and the evaporation process is numerically solved for a single stagnant droplet with initial diameter of $100\ \mu\text{m}$ in still air ($T_\infty = 800\ \text{K}$, $p_\infty = 1\ \text{atm}$). Results of both the model without and with polymerization reaction show continuous variations of the mass fractions of individual components and (pure species) thermophysical properties. At the early stage of evaporation most of the vapor contains the lighter components, i.e. water, acetic and hydroxypropanone. At the end of the vaporization process, only levoglucosan is left in the drop. Furthermore, the results show that the multicomponent fuel does not match the $d^2\ \text{law}$; there is a high evaporation rate during early evaporation process, while a slower evaporation rate is observed in the further process. Validation with literature experimental data of a real BPO shows a disagreement in trend between model and experiment, with experiment showing a more rapid decrease of diameter over time. However, a better agreement with an experiment on a two-component fuel is observed. To improve the qualitative and quantitative predictions of evaporation rate, a model including gradients inside the droplet and representing the effects of internal bubbling would be required. The model including the polymerization reaction predicts that the effect of the proposed reaction of levoglucosan is very small, with only 0.4% lower evaporated mass of levoglucosan.

Acknowledgements

I would like to thank Prof. dr. D. J. E. M. Roekaerts for giving me this thesis opportunity and for the supervision and guidance during this period. You patiently clarified all my concerns and provided me support whenever I encountered a problem.

I also would like to thank Prof. Dr. ir. W. de Jong and Dr. ir. C. A. Infante Ferreira for accepting to be part of the thesis committee and their time during that period.

I am thankful for the unconditional love, patience and support of my beloved family, which helped me to come so far.

Chantal Sital

October 17, 2018

Contents

Abstract	ii
Acknowledgements	iii
Contents	iv
Nomenclature	v
List of figures	viii
List of tables	xi
1 Introduction	1
1.1 Biomass feedstock	1
1.1.1 Biomass resources and constituents	1
1.1.2 Biomass characterization	3
1.2 Pyrolysis oil production process	3
1.2.1 Process description	3
1.2.2 Biomass pyrolysis analysis techniques	4
1.2.3 Pyrolysis oil collection	6
1.3 Pyrolysis oil characterization	7
1.3.1 Elemental analysis and physiochemical properties	7
1.3.2 Pyrolysis oil analysis	9
1.3.3 Pyrolysis oil and conventional fuels	10
1.4 Pyrolysis oil applications	11
1.5 Pyrolysis oil combustion	12
1.5.1 Combustion characterization techniques	12
1.5.2 BPO combustion	13
1.6 Research objective	15
1.6.1 Thesis outline	16
2 Surrogate oil formulation	17
2.1 Formulation methods	19
2.2 Characteristics of the surrogate oil	20
2.3 Surrogate component selection	20
3 Thermal polymerization reaction	26
3.1 Reaction types in BPO	27
3.2 General polymerization reaction kinetics	28
3.3 Literature data on polymerization reaction kinetics for BPO components	29
3.4 Reaction formulation	30

4	Theoretical model	35
4.1	Introduction existing evaporation models	36
4.2	Effects and assumptions	38
4.3	Theoretical model	39
4.3.1	Physical model	39
4.3.2	Droplet environment	41
4.3.3	Evaporation Model	41
4.3.4	Abramzon-Sirignano model	46
4.4	Evaluation of thermophysical properties	47
4.4.1	Thermodynamic properties	47
4.4.2	Transport properties	52
4.5	Development and implementation of evaporation model	53
5	Results and Discussion	56
5.1	Thermophysical properties estimation methods	56
5.1.1	Thermodynamic properties	56
5.1.2	Transport properties	63
5.2	Evaporation in absence of polymerization reaction	67
5.2.1	Stagnant droplet in still air	67
5.2.2	Validation against literature experimental data	71
5.3	Evaporation including polymerization reaction	75
5.3.1	Stagnant droplet in still air	75
5.3.2	Influence ambient temperature	75
6	Conclusions and Recommendations	80
6.1	Conclusions	80
6.1.1	Conclusions on formulation of the surrogate oil	80
6.1.2	Conclusions on determination of the thermal physical properties	80
6.1.3	Conclusions on the formulation of the evaporation model	81
6.2	Recommendations	81
6.2.1	Recommendations on formulation of the surrogate oil	81
6.2.2	Recommendations on determination of the thermal physical properties	82
6.2.3	Recommendations on the formulation of the evaporation model	82
	Appendix A Relevant properties of air and dimer	83
	Appendix B Property estimation methods	84
B.1	Mixing rules for thermophysical properties of the liquid- and gas mixture	84
B.2	Joback group contribution method	85
B.3	Chueh and Swanson group contribution data for specific heat liquid phase calculations	86
B.4	The Reichenberg method for vapor phase viscosity calculations	86
B.5	Roy and Thodos method for vapor phase thermal conductivity calculations	89
B.6	Fuller-Schettler-Giddings atomic diffusion volumes data for binary diffusion coefficient calculations	90
B.7	Schroeder's Method atomic contribution volumes data for latent heat at boiling calculations	91
	Bibliography	92

Nomenclature

Dimensional Parameters

C_p	Specific heat [kJ/kg K]
D	Mass diffusivity [m^2s^{-1}]
d	Droplet diameter [m]
h_T	Convective heat transfer coefficient [m^2K]
J	Diffusive mass flux [$\text{kg m}^{-1}\text{s}^{-1}$]
k	Thermal conductivity [$\text{kWm}^{-1}\text{K}^{-1}$]
L	Latent heat [kJ kg^{-1}]
M	Molar Mass [kg/kmol]
\dot{m}	Droplet evaporation rate [kg s^{-1}]
p	Pressure [kPa]
Q	Heat flow rate [kJ/s]
R	Droplet radius [m]
r	Radial direction [m]
T	Temperature [K]
t	Time [s]
u	Velocity [m/s]

Non-Dimensional Parameters

B_M	Spalding mass transfer number
Bi	Biot number
Le	Lewis number
Nu	Nusselt number
Pe	Peclet number
Pr	Prandtl number
Re	Lewis number
Sc	Schmidt number
Sh	Sherwood number
Y	Mass fraction
G	Heat transfer correction factor
N	Number contribution group
n	Number polymer molecules

Greek Symbols

β	Non-dimensional evaporation parameter [-]
χ	Mole fraction [-]
δ	Gas film thickness [m]
μ	Viscosity [cP]
μ_{dp}	Dipole moment [debye]
ρ	Density [kg/m^3]
v	Atomic diffusion volume [m^3]

ε Evaporation rate [-]

Subscripts

∞ Far away condition for droplet
 i, j Species numbering
0 Initial conditions
b Boiling point
D Diffusion
d Droplet
e Evaporation
eq Equilibrium
g Gas
k Contribution group numbering
L Liquid
M Mass transfer
m Gas-Vapor mixture surrounding the droplet
mp Melting point
ref Reference conditions
S Droplet surface
V Vapor

Acronyms

BPO Biomass Pyrolysis Oil
C Carbon
DLM Diffusion limit model
DP Degree of Polymerization
DSC Differential Scanning Calorimetry
DTG Differential Thermo-Gravimetric analysis
ECM Effective conductivity model
FCM Finite conductivity model
GC-MS Gas Chromatography–Mass Spectrometry
HHV Higher Heating Value
ICM Infinite Conductivity Model
LHV Lower Heating Value
N Nitrogen
O Oxide
PDF Probability Density Function
pH potential of Hydrogen - Acidity
RMM Rapid Mixing Model
S Sulfur
STP Standard Temperature and Pressure
TGA Thermo-Gravimetric Analysis

List of figures

1.1	Left: Process flow diagram of the pyrolysis process. Adapted from [12]. Right: Schematic for pyrolysis process [11].	4
1.2	Product distributions of biomass pyrolysis on PCR: (A) on dry feedstock basis. (B) on dry ash free feedstock basis. [37].	5
1.3	Left: TGA and DTG curves for micro-algal biomass with decomposition stages included [24]. Right: DTG curve for lignocellulosic biomass with decomposition of main constituents included [17]	5
1.4	Representative pyrogram (switchgrass pyrolysis) with major chemical species found in products of sample biomass GC/ MS analysis [103]	6
1.5	GC-MS method representation	9
1.6	GC-MS spectra of the aqueous-phase and oily-phase bio-oils [28].	9
1.7	The variation of water content and viscosity with aging time of BPO. Figure constructed with experimental data from [82].	11
1.8	Applications of pyrolysis products [5].	11
1.9	The mass fraction Y (left) and time derivative of the mass fraction $-\frac{KdY}{dt}$ (right) curves over time t and temperature T [26].	13
1.10	Direct color image of single droplet combustion with internal convection effect [28].	13
2.1	Definitions of terms (above) used in this study for the followed formulating process (below) to create the surrogate oil.	18
2.2	Basic principle representation of continuous thermodynamics	19
2.3	Chemical composition of BPO's including the most abundant molecules of each of the components and the biomass fraction from which the com- ponents were derived [75].	22
2.4	TGA and DTG for BPO divided in the identified main six zones. Slightly adapted from [76] from the Dynamotive BPO sample.	23
2.5	Molecular structures of the selected components	25
3.1	DSC curves of kerosene mixed with the dissimilar compositions of the bio-oil [28]. Slightly adapted.	27
3.2	General pathways of occurring reactions generating larger molecules in which R stands for a ring. The figure is constructed with information from reference [82].	28
3.3	Typical sigmoidal curve for a component which undergoes polymerization	30
3.4	Representation of a single Levoglucosan molecule (top), a dimer (mid) and a trimer (bottom) with a 1,4 linkage and a 1,6 linkage respectively. This figure is constructed with information from [81].	31
3.5	Concentration vs rate graph for a second order reaction.	33

4.1	Schematic representation of an evaporating droplet surrounded by gas with vapour mass fraction and temperature distributions along the radial direction.	35
4.2	Schematic representation of the mass transfer during evaporation of a droplet.	40
4.3	Schematic representation of the heat transfer during evaporation of a droplet.	40
4.4	Flowchart of the droplet evaporation model.	55
5.1	Latent heat variation with temperature of the pure components.	58
5.2	Latent heat variation with temperature of pure acetic acid.	58
5.3	Vapor pressure of the pure components variation with temperature.	59
5.4	Vapor pressure of pure water variation with temperature.	60
5.5	Vapor pressure of pure acetic acid variation with temperature.	60
5.6	Vapor pressure of pure levoglucosan variation with temperature.	61
5.7	Liquid density variations with temperature of pure components.	61
5.8	Liquid density variations with temperature of pure acetic acid.	61
5.9	Vapor phase specific heat of pure components.	62
5.10	Left: Vapor phase specific heat of pure acetic acid. Right: Vapor phase specific heat of pure phenol.	63
5.11	Vapor phase viscosity of pure components.	63
5.12	Vapor phase viscosity of pure acetic acid.	64
5.13	Vapor phase thermal conductivity of pure components.	64
5.14	Vapor phase thermal conductivity of pure acetic acid.	65
5.15	Binary diffusion coefficient of water vapor into the other species in the vapor-gas mixture.	65
5.16	Left: Binary diffusion coefficient of acetic acid vapor into the other species in the vapor-gas mixture. Right: Binary coefficient of hydroxypropanone vapor into the other species in the vapor-gas mixture.	66
5.17	Left: Binary diffusion coefficient of phenol vapor into the other species in the vapor-gas mixture. Right: Binary coefficient of eugenol and levoglucosan vapor into the other species in the vapor-gas mixture.	66
5.18	Species mass fractions variations with time.	68
5.19	Variation of liquid mass fractions with time.	69
5.20	Variation of droplet temperature with time.	70
5.21	Variation of diameter squared ratio with time.	70
5.22	Variation of heat transfer rate at the droplet surface with time.	71
5.23	Definition of the internal bubbling interval during the vaporization process of a binary-component 50–50% volume percentage heptane-hexadecane droplets, $d_0 = 1.1 \text{ mm}$, $T_\infty = 673 \text{ K}$, $T_{d_0} = 300 \text{ K}$, $p_{1\infty} = 1 \text{ atm}$ [87].	71
5.24	Normalized droplet diameter squared as a function of residence time in the reactor [27]. The points are experimental data points, while the solid line is the best fit.	73
5.25	Temperature and droplet lifetime comparison between predicted and experimental data from Torres et. al. [106].	74
5.26	Species mass fractions variations with time including polymerization reaction.	76
5.27	Variation of species mass fraction inside the droplet with time including polymerization reaction.	77
5.28	Species mass fractions variations with time including polymerization reaction.	78

5.29	Variation of heat terms with time. Left: over the whole time range. Right: a close up of the time range where the reaction is most active.	78
5.30	Influence of ambient temperature on droplet evaporation including polymerization reaction.	79

List of tables

1.1	Overview of main algal and lignocellulosic biomass constituents.	2
1.2	Typical pyrolysis oil and conventional fuel properties [6, 28]	10
2.1	Design properties and approximate targets of BPO's which can figure as target oil	21
2.2	Weight loss (WL) in wt.% for the different temperature zones as measured using TGA and predicted values based on oil composition and boiling points. Data (Dynamotive, BTG, Pyrovac, Ensyn) reproduced from Branca et al. [76] and (VTT) from van Rossum et al. [29].	23
2.3	Selected components for the surrogate oil. $T_{b,i}$ stands for boiling temperature, $Y_{L,i}$ stands for (initial) species i liquid mass fraction and M_i for molecular weight. Superscript numbering stands for species i numbering.	24
3.1	Polymer properties. The -P stands for -phenol, T_b for boiling point, MW for molecular weight, ΔH_{vap} for heat of vaporization (latent heat) and T_m for melting point and the number between brackets stands for the amount of groups identified. Data obtained from Appendix B.2.	33
4.1	Liquid mole fraction and critical temperature of each component as obtained by the Joback method. $T_{c,i}$ and $\chi_{L,i,init}$ stands for the critical temperature and liquid mole fraction of species i	38
5.1	Boiling point temperatures [K]	56
5.2	Critical point data estimated by the Joback method. In between the brackets are values found from databases.	57
5.3	Latent heat at boiling point [kJ/kg].	57
5.4	Liquid phase specific heat [kJ/kgK].	62
5.5	Main differences between assumptions/ effects of the model of Torres et al. [106] and the model of the current study.	73
A.1	Relevant properties air at 1.01325 bar [97].	83
A.2	Relevant properties solid dimer at 1.01325 bar [89].	83
B.1	Mixing rules applied to obtain properties for the liquid and gas phase.	84
B.2	Contributing groups of selected components.	85
B.3	Relevant property estimation functions obtained from table C.1 from [55].	85
B.4	Property estimation data obtained from table C.1 from [55].	86
B.5	Chueh and Swanson group contributions data [$kJ/kmol \cdot K$] for liquid heat capacity at 293.15 K [95].	87
B.6	Values of the Group Contributions C_k for the Estimation of a^* (Reichenberg, 1971) [55]	88

B.7 Dipole moments of the selected components in vapor phase [89].	88
B.8 Recommended $fn(T_r)$ equations for the Roy-Thodos Method [55].	89
B.9 Roy and Thodos group contribution data [55].	90
B.10 Atomic diffusion volumes [cm^3] [90].	90
B.11 V_b Contributions in Schroeder's Method [94].	91

Chapter 1

Introduction

1.1 Biomass feedstock

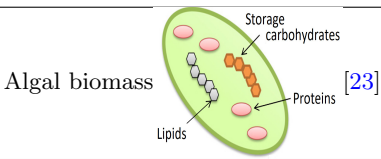
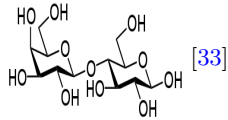
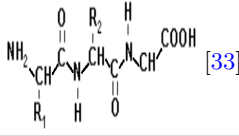
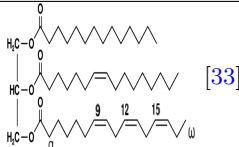
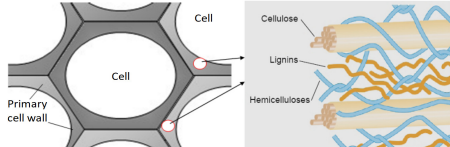
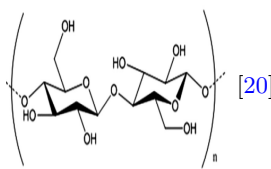
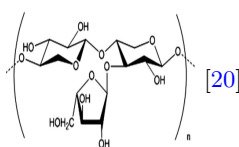
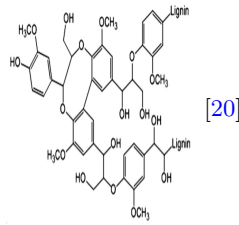
1.1.1 Biomass resources and constituents

Biomass sources include wood wastes, energy crops, aquatic plants, agricultural crops, and their waste products and municipal and animal wastes; and are considered as potential sources of fuels and chemical feedstock's [5]. The inherent properties of the biomass source determine both the choice of conversion process and any subsequent processing difficulties that may arise. Equally, the choice of biomass source is influenced by the form in which the energy is required and it is the interplay between these two aspects that enables flexibility to be introduced into the use of biomass as an energy source. Dependent on the energy conversion process selected, particular material properties become important during subsequent processing [14].

Pyrolysis is, amongst others, a thermochemical process of biomass decomposition into various useful products with a higher energy density, either in the absence of an oxidation medium, or with a small presence which does not enable gasification to an appreciable extent. During pyrolysis, large and complex biomass hydrocarbon molecules break down to relatively smaller and simpler gas, liquid and solid molecules [12]. It is difficult to divide pyrolysis oil feedstocks into different categories, because such classifications are dependent on the biomass species, growth conditions, age, portion of the plant selected, and many other variables [9]. Conventional biomass, is generally divided into two groups: lignocellulosic biomass (dry feedstock) and algal biomass (wet feedstock). Lignocellulosic biomass (e.g. agricultural residues, forest resources and energy crops) is mainly composed of macromolecular substances – cellulose, hemicellulose and lignin. Algal biomass (e.g. micro- and macro algae and non-food oil crops) is mainly composed of carbohydrates, proteins and lipids [6, 9, 20, 32]. Up till now, in the context of biomass valorization, lignocellulosic biomass has been studied much more broadly than algal biomass [23]. Smaller amounts of low molecular weight substances: extractives and inorganics (salts or minerals) are also present in biomasses. Extractives are organic compounds and inorganics are the species that form the ashes. The main inorganic constituents being compounds of potassium, calcium, sodium, silicon, phosphorus, and chlorines [5, 23].

Table 1.1 gives a short overview of the main constituents of biomass feedstocks with main chemical structures included (specific structure varies with the parent biomass).

Table 1.1: Overview of main algal and lignocellulosic biomass constituents.

		
Substance	Description	Chemical structure
Carbohydrates	Carbohydrates are a wide category encompassing sugars (monosaccharides) and their polymers. Carbohydrate fraction consists mostly of cellulose and starch without any lignin residue. The most abundant carbohydrates are glucose, rhamnose, xylose, and mannose. Carbohydrates act as structural components in the cell walls, and as storage components inside the cell. Moreover, their polymers are easily decomposed [9].	 [33]
Proteins	Proteins are the most complex macro molecules and are important structural components of the cell wall. They consists of several chains of peptide which reduces to polymers of amino acids and are as easily decomposed as carbohydrates [9].	 [33]
Lipids	Lipids are hydrophobic non-polar compounds with aliphatic characteristics that include fatty acid, fats and triglycerides. Lipids decompose under higher temperatures than carbohydrates and proteins [9, 33].	 [33]
		
Substance	Description	Chemical structure
Cellulose	Cellulose is a straight glucose polymer. Having a higher molecular weight, higher degree of polymerization, higher crystal strength and stronger intra - and inter molecular interactions amongst hydrogen bonds results in having a less conducive nature to decomposition than hemicellulose. It is a non-polar compound at ambient temperature, but tends to be soluble with increasing temperature [9, 32].	 [20]
Hemicellulose	Hemicellulose is an amorphous polymer containing several different types of sugars [32]. Having a degree of polymerization much lower than cellulose, it surrounds the cellulose fibers and stands as a connecting link between cellulose and lignin. Compared to cellulose and lignin, it possesses a weaker structure and is less resistant to intra-molecular hydrogen bonding. Hemicellulose is the least thermally stable component due to its amorphous nature Hence, the conducive nature to decomposition of it is severe and prone to easy miscibility characteristic [9].	 [20]
Lignin	Lignin, an amorphous polymer, possesses similar morphological characteristic of amorphous form as hemicellulose, less solubility similar to cellulose and the peculiar behaviour of hydrophobic nature. The significant feature of lignin encompasses the higher energy content, compared to the other two compounds, that leads to higher heating value to the product. Since it is a very complex polymer, it is more thermally stable compared to the other two components [9, 32].	 [20]

1.1.2 Biomass characterization

In theory, all biomass can undergo pyrolysis, but not all biomass is suitable for a particular end product, therefore characterization of biomass is essential. Ganesh [10] developed criteria for evaluating the suitability of biomass for a conversion process to obtain solid, liquid and gaseous fuels. As is shown in earlier publications different biomass, on pyrolysis, gave different product yields with different product properties [5, 10]. Characteristics of biomass include its moisture content, percentage ash, volatile matter, fixed carbon, heating values, compositional analysis (e.g. lignin and structural carbohydrates) and elemental composition (carbon C , hydrogen H , nitrogen N , sulphur S and oxygen O). Carbon represents the major contribution to the overall heating value. Atomic ratios (H/C) and (O/C) shows that biomass has very high relative amounts of oxygen and hydrogen resulting in relatively low heating values; this can also be seen from the main constituents chemical structures in 1.1. Characterization is also based on physical, chemical and mechanical properties. Physical properties of biomass include shape and size of biomass particles, aspect ratio of biomass particles, sphericity of particles, particle size distribution, density, porosity and densification of biomass. Chemical properties of biomass include chemical composition, elemental composition and equilibrium moisture content. Mechanical properties include other properties having a role in biomass collection, handling, transportation, and storage [12, 14].

Studies in which biomass characterization is carried out for for lignocellulosic biomass are [5, 21, 37, 71], and for algal biomass [2, 14, 15, 28, 37].

1.2 Pyrolysis oil production process

1.2.1 Process description

Pretreatment of the biomass feed is required, i.e. dewatering (wet biomass), drying and grinding. Dewatering ($\leq 25\%$ water) and drying ($\leq 10\%$ water) is usually essential as all the water contained in biomass will increase pyrolysis oil water content.

The general changes that occur during pyrolysis are summarized below [3], see figure 1.1:

- Heat transfer from a heat source, to increase the temperature inside the biomass;
- The initiation of primary pyrolysis reactions at this higher temperature releases volatiles and forms char;
- The flow of hot volatiles toward cooler solids results in heat transfer between hot volatiles and cooler unpyrolyzed biomass;
- Condensation of some of the volatiles in the cooler parts of the fuel, followed by secondary reactions, can produce tar;
- Autocatalytic secondary pyrolysis reactions proceed while primary pyrolytic reactions (item 2, above) simultaneously occur in competition;
- Further thermal decomposition, reforming, water gas shift reactions, radicals recombination, and dehydrations can also occur, which are a function of the process's residence time/ temperature/pressure profile.

Biomass particles have to be very small to allow rapid heating and to achieve high liquid yields. Particle size depends on the pyrolysis reactor used. The fluidizing bed reactor uses the smallest size of 2 mm and is used most because of the ease of operation and scale up. The essential features of a fast pyrolysis reactor are high heating and heat transfer rates, moderate and carefully controlled temperature and rapid cooling or

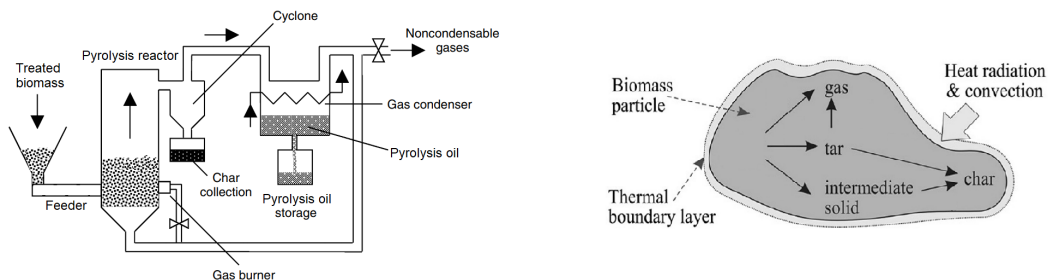
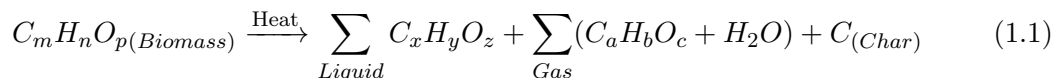


Figure 1.1: Left: Process flow diagram of the pyrolysis process. Adapted from [12]. Right: Schematic for pyrolysis process [11].

quenching of the pyrolysis vapours. Pyrolysis reactors have two important requirements for heat transfer; *i*) heat transfer to the reactor medium and *ii*) heat transfer from the medium to the biomass. These heat transfers could be gas-solid where heat is transferred from the hot gas to the pyrolysis biomass particles through convection, and solid-solid where conductive heat transfer occurs. About 90% of heat transfer in fluid bed reactors occurs by conduction, with a small contribution of convection heat transfer of up to 10%, because of utilizing of good solid mixing. Along with convection and conduction, some radiation heat transfer also occurs in all types of reactor. The use of a catalyst may redirect the chemical reactions during the pyrolysis process resulting in the in situ upgrading of the end product(s). Generally, the pyrolysis process can be described by reaction expressed in equation (1.1) [12].



in which m , n and p are subscripts for species on the source side, while x , y , z , a , b and c are subscripts for species on the product side.

Two main streams are formed from biomass decomposition in the reactor, i.e. a solid stream (char) and a gas (vapors and noncondensables) stream, see figure 1.1. Almost all of the ash in the biomass is retained in the char, so successful char removal (occurring in the cyclones) gives successful ash removal. A condenser is included in the process to separate the noncondensable and condensable gases and to convert the condensable gases to liquid, from which pyrolysis oil is extracted. Liquid collection trough condensation of the vapors contained in the gas stream is further explained in 1.2.3. Char contributes to secondary cracking by catalyzing secondary cracking reactions in the vapour phase. Rapid and complete char separation is therefore desirable. Some fine char transported with the gas phase will remain in the cooled collected liquid product and contribute to instability problems, accelerating the slow polymerization processes. Figure 1.2 gives an overview of the products and yields generated by pyrolysis of four biomass types.

1.2.2 Biomass pyrolysis analysis techniques

Biomass pyrolysis analysis techniques give insight about the thermal degradation mechanisms and kinetics of biomass. It also gives insight about the components which are contained in the pyrolysis oil.

Thermogravimetric analysis

Thermogravimetric analysis (TGA) is carried out during biomass pyrolysis in which the non-decomposed biomass (wt. %) vs. its temperatures are detected. It is an established method for studying the thermal degradation mechanisms and kinetics of biomass and

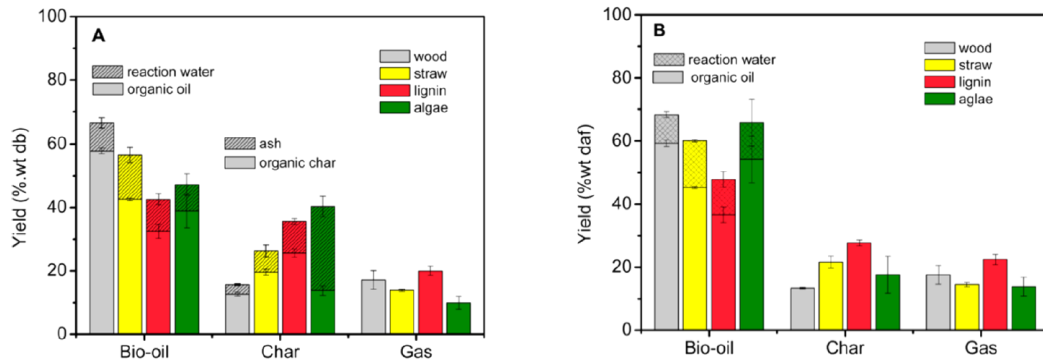


Figure 1.2: Product distributions of biomass pyrolysis on PCR: (A) on dry feedstock basis. (B) on dry ash free feedstock basis. [37].

provides semi-quantitative information about the pyrolysis temperature and kinetics, and phase distribution of the products. Moisture removal occurs in the first stage while most of the pyrolysis occurs in the second stage in which most of the organic material is decomposed and remaining solid slowly decomposes in the third stage. The differential thermogravimetric (DTG) is a derivative of the TGA curve, see figure 1.3. The latter makes small boulders on the TGA curve more clear as peaks. The left graph displays both the TGA curve and DTG curve for algal biomass, while the right graph displays the TGA curve for lignocellulosic biomass (in which dehydration already took place). Based on the main DTG peaks, temperature and decomposition ranges, thermal degradation of the algae differs distinctly from that of the lignocellulosic biomass.

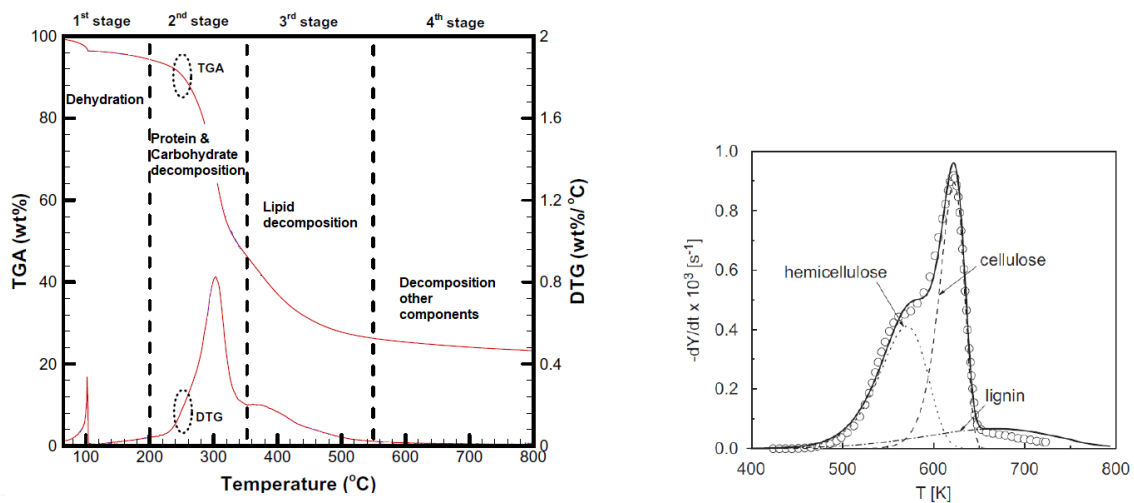


Figure 1.3: Left: TGA and DTG curves for micro-algal biomass with decomposition stages included [24]. Right: DTG curve for lignocellulosic biomass with decomposition of main constituents included [17]

Pyrolysis-GC/MS

Pyrograms obtained from pyrolysis gas chromatography–mass spectrometry (GC-MS) of biomass provide information about the amount and types of pyrolysates generated from biomass. The peaks from the total pyrogram for each compound created during pyrolysis provide a reasonable estimate of the relative abundance of those compounds within the pyrolysis product mixture, see figure 1.4. Not only can a GC-MS separate the volatile components of complex mixtures, but it can also record a mass spectrum of

each component. Only a portion of the pyrolysis oil can be detected via GC; in addition, the pyrolysis oil contains polar nonvolatile components that are only accessible via other techniques. Different types of pyrolysis can be distinguished based on the heating rate,

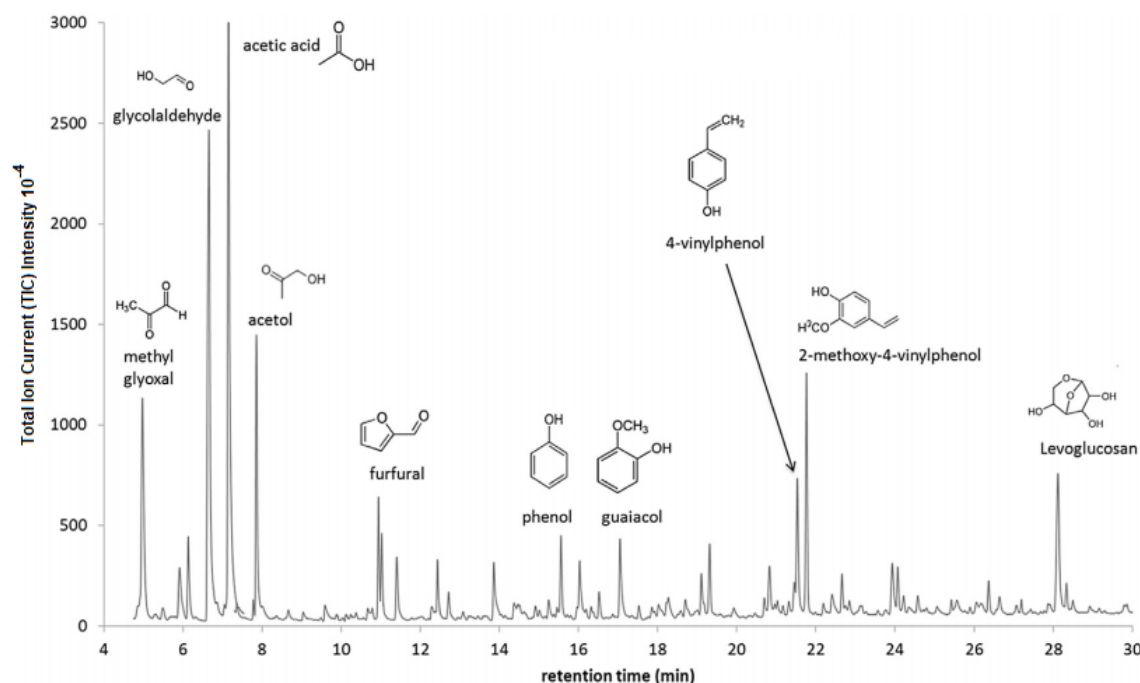


Figure 1.4: Representative pyrogram (switchgrass pyrolysis) with major chemical species found in products of sample biomass GC/ MS analysis [103]

process temperature, process pressure, vapor residence time and the composition and yields of products formed. However, short vapor residence times (≤ 2 s), relatively high process temperatures (450-600 °C) and high heating rates (1000-10,000 °C/s [12]) are required for higher and more stable pyrolysis oil yields (typically 75% wt.) [3, 30, 100]. These requirements make it a fast pyrolysis process. Studies like [100] go more into detail about the various process effects on the end products, while studies like [3, 5], go more into detail about pyrolysis process and types. Studies like [2], have carried out experiments of pyrolysis of algal, [2, 16] and lignocellulosic biomass.

1.2.3 Pyrolysis oil collection

The pyrolysis vapours can be characterized as a combination of true vapours, micron sized droplets and polar molecules bonded with water vapour molecules [101]. The time and temperature profile between formation of pyrolysis vapours and their quenching in the condenser influences the composition and quality of the liquid product. High temperatures will continue to crack the vapours and the longer the vapours are at higher temperatures, the greater the extent of cracking. Although secondary reactions become slow at lower temperatures, some secondary reactions will continue down to room temperature which contributes to liquid separation and layering in the pyrolysis oil. The time-temperature envelope that the pyrolysis vapours endure will affect the oil quality. Vapour residence (for fuel as an end product) in the condenser are around 2 s. Longer residence times result in significant reductions in organic yields due to cracking reactions. Condensation under controlled temperatures with a condensing solvent separates uncondensable and condensable vapors into gasses and liquids. After solvent and (large part of) loose water removal, the liquid product is obtained, i.e. the biomass pyrolysis oil (BPO).

The latter is a homogenous hydrophilic (oleophobic) mixture of polar organics and some (loose and chemically bound) water from both the biomass pyrolysis reaction and the original water in the feedstock. Further water separation can concentrate the organics from original pyrolysis oils. To obtain a higher organic yield, further solvent extraction is necessary to gather and remove the more weak-polarity organics, however if too much water is removed, the oil tends to behave inhomogeneously [28, 37, 100, 32, 34, 101]. BPO is the only end product of pyrolysis on which this study focuses.

1.3 Pyrolysis oil characterization

BPO is composed of differently sized molecules derived primarily from the depolymerization and fragmentation reactions of three key biomass building blocks as previously discussed in 1.1 [3].

1.3.1 Elemental analysis and physiochemical properties

The physiochemical properties of BPO, vary significantly from those of conventional mineral oils (mainly because of their different elemental composition). The oil properties and composition are dependent on several factors such as feed biomass, moisture content in the feed, process parameters (vapor phase residence time, temperature, and pressure), reactor type, recovery design unit and the scale of operation. Pyrolysis oils contain extensive moisture content, suspended solids, char, oxygen and acidic compounds. These constituents have low heating/calorific values. While mineral oils have oxygen content at ppm level, pyrolysis oils comprise of 35 - 40 wt.% oxygen, present in several organic functional groups. These functional groups are also responsible for highly polar nature of the pyrolysis oil. Element analysis (*C*, *H*, *N*, *S*, *O*, ash and moisture content) and physiochemical properties are summarized below.

Moisture content

Water in pyrolysis oils result from the original moisture in the feedstock and as a product of the dehydration reactions occurring during pyrolysis. Therefore, the water content varies over a wide range (15-30 wt.%) depending on the feedstock and process conditions. Water is homogeneously dissolved in the oil and cannot be eliminated by a drying process/ solvent without losing volatile hydrocarbon compounds. The presence of water lowers its heating value (*LHV*) and flame temperature, increases its ignition delay and leads to decrease of the combustion rate and the viscosity [17, 30].

Oxygen content

The presence of oxygen is one of the major differences between the pyrolysis oils and the hydrocarbon fuel, leading to low energy density (less than 50 wt. %) and immiscibility with conventional fuels, chemical instability and leads to a wide range of both boiling point temperature and viscosity. Oxygen content up to 35 - 40 wt.% distributed over 300 compounds has been reported in the literature. The oxygen content is dependent on the *O* atoms from the pyrolysis oil's water content and from other components [30].

Fixed carbon content

The fixed carbon content in BPO is between 30-60 wt. % and carbon represents the major contribution to the overall heating value [9].

Hydrogen content

Hydrogen is another major constituent of biomass, as can be expected from the chemical structure of the carbohydrate and phenolic polymers. The content is between 5-10 wt.% for BPO. During combustion, hydrogen is converted to H_2O , significantly contributing to the overall heating value [9].

Ash and char

Ash derived from the parent feedstock is present in the pyrolysis oil at variable concentrations. Inorganic elements in the ash are known to catalyze char forming reactions during combustion or aging of BPO [36]. These reactions lead to the formation of larger quantity and change in composition of solid residue and a decrease of the amount of gas. [35]. Furthermore, some ash components present in BPO lower the heating value.

Nitrogen and sulfur contents

Since sulfur content generally is insignificant, no SO_x emissions are generated and decreases corrosion properties. Nitrogen contents are also lower compared to fossil fuels; BPO generate more than 50% lower NO_x emissions than e.g. diesel oil in a gas turbine. [35] (if operated under same conditions). However, nitrogen content influences the overall heating values [9].

Viscosity

The viscosity of the pyrolysis oil can vary from 35 to 1000 *cP* (at 40 °C), depending strongly on the nature of feedstock, processing, and pre-processing conditions, and also on the efficiency of collection of low boiling components. The viscosity of pyrolysis oil tends to increase with storage time, as a result of chemical reactions taking place in-between the BPO constituents [17].

Density

The specific gravity of the liquid is about 1.10 to 1.25, which means it is slightly heavier than water, heavier than fuel oil and significantly heavier than the bulk density of the original biomass [80]. Typically, pyrolysis oils are single-phase liquids with a density of about 1.1–1.3 kg/m^3 .

Molecular weight

The complex mixture comprises both polar and non-polar chemical components of different molecular weights. In BPO more polar than non-polar components are present[3].

Thermal stability

BPO is thermally unstable and when heated, undergoes polymerization processes leading to the formation of char and in-homogeneity layering or partial separation of phases [9]. Pyrolysis oil evaporation is always coupled to the formation of char. This represents one of the most severe obstacles for a direct use of pyrolysis oils in furnaces or diesel engines [18].

Acidity

The, oxygen, water and carboxylic acids, such as acetic acid and formic acid present in the oil, increase its acidity ($2 \leq pH \leq 3.8$) and make it corrosive for the handling equipment and storage vessels, essentially at high temperatures and high water content [3].

Boiling point

Due to its strongly multicomponent composition, BPO has a very wide boiling range [17].

Heating value

As mentioned before, the presence of water which is always present in BPO, leads to low heating values and [3, 17]. An empirical expression for the Higher Heating Value (HHV) based on the elemental composition mass fraction is given in equation 1.2 [104].

$$HHV [MJkg^{-1}] = (3.55C^2 - 232C - 2230H + 51.2C \cdot H + 131N + 20600) \cdot 10^{-3} \quad (1.2)$$

1.3.2 Pyrolysis oil analysis*Thermogravimetric analysis*

As explained for biomass pyrolysis, see section 1.2.2, the TGA and DTG methods can also be used to investigate thermal decomposition of BPO, which will be explained in more detail in section 1.5.1.

Chemical composition analysis

GC-MS is the most commonly used characterization method reported in the literature for analysis of the organic fraction of BPO to provide further information on the composition of the BPO. The GC section of the equipment separates the individual components of the pyrolysis oil vapor through the GC column, followed by identification of these components at MS. For analysis of the aqueous fraction use of high-pressure liquid chromatography (HPLC) has been reported. Pyroprobe gas chromatography-mass spectrometer (Py-GC-MS) is a state of art characterization technique for effective research in the field of biomass pyrolysis, see figure 1.5. It enables an online analysis of the products from the pyroprobe and thus identifying all evolved species over a particular temperature range. A pyroprobe is a small reactor for pyrolysis of a biomass sample under very well controlled conditions. Figure 1.6 illustrates the GC-MS results of the of cedar bio-oil samples.

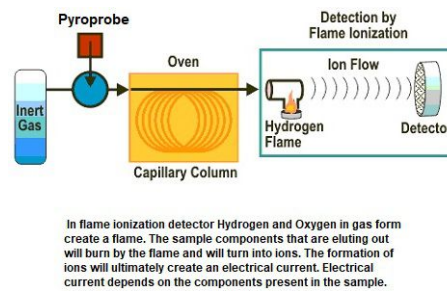


Figure 1.5: GC-MS method representation

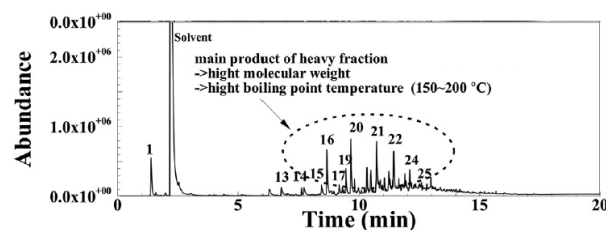


Figure 1.6: GC-MS spectra of the aqueous-phase and oily-phase bio-oils [28].

Only the volatile part of the oil can be detected and of this part only the captured part of the volatile components for further analysis is studied. Using the GC/MS technique, Branca et al. [52] experimentally quantified 40 components of bio-oil produced from fast pyrolysis of wood and classified the components according to the component detection temperature. The 40 components correspond to 62-65% of the total liquid. Tsekos [61] carried out an experimental study on fast pyrolysis of woody biomass in a pyroprobe reactor to study the effect of torrefaction on the pyrolysis products for his Master's thesis.

1.3.3 Pyrolysis oil and conventional fuels

Dissimilar liquid fuels exhibit distinct physical and chemical properties, such as volatility, boiling point, latent heat of vaporization, specific heat capacity, and thermal conductivity [28]

Relative to petroleum-based liquid fuels, as discussed in section 1.3, BPO contains large amounts of water and organic oxygenates, is quite acidic and undergoes polymerization reactions due to aging but also during heating. The components of the biomass oils also span a wide range of volatilities. The viscosities of the biomass oils differ substantially, as do their physical states [27].

The presence of large amounts of oxygen in plant carbohydrate polymers means the pyrolytic chemistry differs sharply from fossil feeds. Biomass pyrolysis products are a complex combination of the products from the individual pyrolysis of each of the constituents presented in 1.1, each of which has its own kinetic characteristics. In addition, secondary reaction products result from cross-reactions of primary pyrolysis products and between pyrolysis products and the original feedstock molecules [3]. Table 1.2 gives a summary of typical values for BPO, diesel and Heavy Fuel Oil (HFO) properties. BPO resembles more with HFO, but still has a lower heating value, a higher moisture content and a very high oxygen content.

Table 1.2: Typical pyrolysis oil and conventional fuel properties [6, 28]

Property	BPO	Diesel	Heavy Fuel Oil
HHV	15.7	49.0	37.5
LHV	13.9	46.0	35.6
Density at 293.15 $[kg/m^3]$	1200	800	900
Viscosity at 313.15 $K [Pa \cdot s]$	0.04-0.01	0.004	0.13
Water content (wt. %)	27.8	0.007	1.6
pH	2 - 3	n.a.	5
Elemental composition (d.b.):			
C (wt. %)	39.95	86.4	79.0
H (wt. %)	8.00	13.7	9.0
N (wt. %)	0.04	0.0	n.a
O (wt. %)	52.05	0.0	12.0

Figure 1.7 gives experimental data of the change in water content and viscosity vs aging time of BPO. The increase of water suggests that some condensation or dehydration reactions occurred in the oil during storage, especially when exposed to higher temperatures. The viscosity of the oil increased with the length of storage. The changes resulting from storage at higher temperatures were greater than those occurring at 37 °C. The viscosity of pyrolysis oils strongly depends on their water content. Normally dilution with water makes the oils less viscous. However, the increase in water concentration of the stored oil was accompanied by an increase in its viscosity. Because viscosity is related

to the molecular weight of the material, these measurements indicate that condensation reactions have occurred in the oil, especially when exposed to higher temperatures.

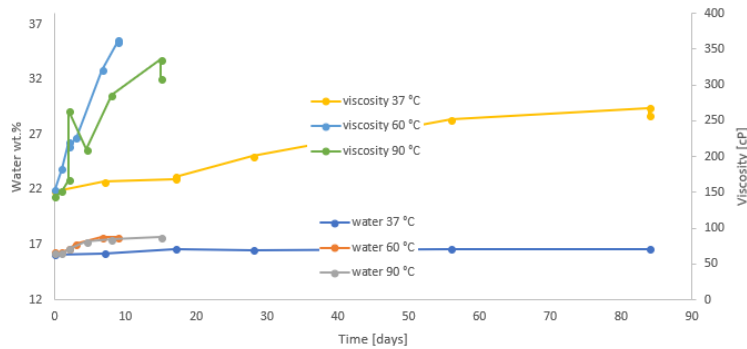


Figure 1.7: The variation of water content and viscosity with aging time of BPO. Figure constructed with experimental data from [82].

1.4 Pyrolysis oil applications

Figure 1.8 gives an overview of BPO applications (so far) [5]. The red bordered applications are the type this study focuses on, i.e. combustion applications however end use of BPO may not only be electricity and heat production.

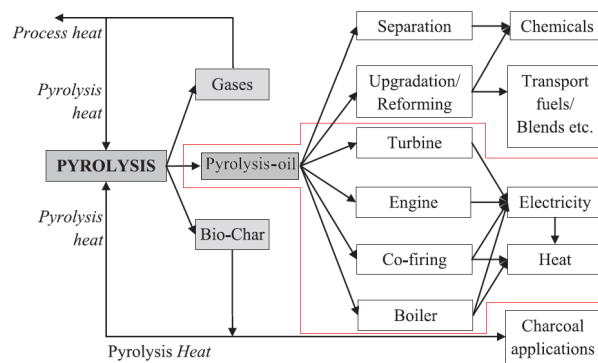


Figure 1.8: Applications of pyrolysis products [5].

Gas turbines are relatively fuel-flexible and are capable of generating power on both large and small scales, suiting the demands of the future energy system. Pyrolysis oil combustion in gas turbines has therefore been subject of a few experimental studies in the past years[58, 64]. These studies, conducted in both scientific and industrial test rigs, have shown that the use of pure pyrolysis oil often leads to major problems. Reported issues include high CO emissions, flame instability, fuel deposits in the hot section and unburned particles in the exhaust gas. The poor burning characteristics of pyrolysis oil are related to their characteristics as discussed in section 1.3.

Industrial fuel

Pyrolysis oil can serve as a substitute for fuel oil or diesel in many static applications, including boilers, furnaces, engines, and turbines for electricity generation.

Heat Production

The heating value of pyrolysis oil is lower than that for fossil fuel, because of the large

number of oxygenated compounds and a significant portion of water. Nevertheless, combustion tests showed that fast pyrolysis oils could replace heavy and light fuel oils in industrial boiler applications.

Power generation

The use of a pyrolysis oil requires engine modifications mainly due to its high acidity. The most important changes involve the fuel pump, the linings, and the injection system. Slight modifications of both the pyrolysis oil and the diesel engine can render pyrolysis oils an acceptable substitute for diesel fuel in stationary engines. Pyrolysis oil blends with standard diesel fuels or bio-diesel fuel is also possible.

Recently, a quantitative assessment was conducted of the economic competitiveness of pyrolysis oil standard applications in 14 European countries. A competitive factor (cF) was developed that represented the total annual cost of a conventional alternative relative to pyrolysis oil application. A wide variation was observed across Europe. A total of six countries had at least one pyrolysis oil application, which was economically competitive now. Overall, heat-only applications were determined to be the most economically competitive, followed by combined heat and power (CHP) applications, with electricity-only applications being only very rarely competitive. With the recent increase in the crude oil price, these quantitative assessments should be continuously updated in the search for commercial opportunities [3].

1.5 Pyrolysis oil combustion

As discussed in section 1.3, due to its elemental composition and physiochemical properties, which is distinct from conventional fuels, BPO combustion behaviour will not be the same.

1.5.1 Combustion characterization techniques

TGA, as used for the decomposition of biomass, is also widely used in the literature to characterize the different mechanisms occurring during combustion of BPO (thermal decomposition). This methodology is limited to rather low heating rates. The related process of weight loss is indicated as devolatilization because, in addition to evaporation, it is likely that cracking reactions also take place. The weight loss during this stage is very high due to evaporation and cracking reactions. Polymerization reactions are also presumably active, ultimately leading to the formation of coke, which in this study is indicated as secondary char (to make a distinction with the primary char, generated from fast pyrolysis). Figure 1.9 gives the TGA and DTG curves of BPO (woody biomass) for just a qualitative indication. Here, Y stands for the sample mass fraction, and KdY/dt for the time derivative of the mass fraction. It is likely that polymerization reactions occur simultaneously with component evaporation and cracking [26].

Three main zones of the DTG curve can be distinguished [35]:

- (i) At first, the water contained in the BPO vaporizes together with light volatile matters. This region shows a steep decrease of the mass fraction;
- (ii) As the temperature of BPO continues to increase, pyrolysis occurs, leading to the release of so-called primary volatile matters and to the formation of char (a less steep decrease of the mass fraction). The primary volatiles undergo secondary reactions through two competitive pathways, re-polymerizing to form char and

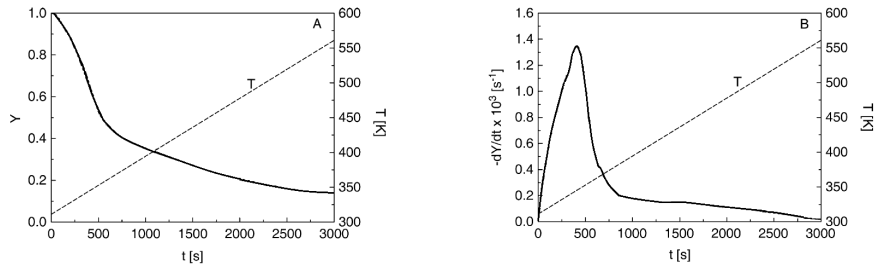


Figure 1.9: The mass fraction Y (left) and time derivative of the mass fraction $-\frac{KdY}{dt}$ (right) curves over time t and temperature T [26].

cracking to form lighter volatiles. The re-polymerization pathway is favored by lower heating rates leading to longer volatiles residence times inside the sample, and favor secondary reactions of re-polymerization to form solid residue;

- (iii) Finally the collected products are the solid residue (char) and permanent gases. The major gas species classically identified during pyrolysis are H_2 , CO , CO_2 , C_2H_2 , C_2H_4 . Tars: the condensable volatile organic compounds, and water which is originating both from the water initially present in pyrolysis oil and from the pyrolysis reaction.

1.5.2 BPO combustion

Combustion tests carried out by Yang et al. [28] on single droplets demonstrated a very unique, multi-step process comprised of the phases as represented in figure ??.

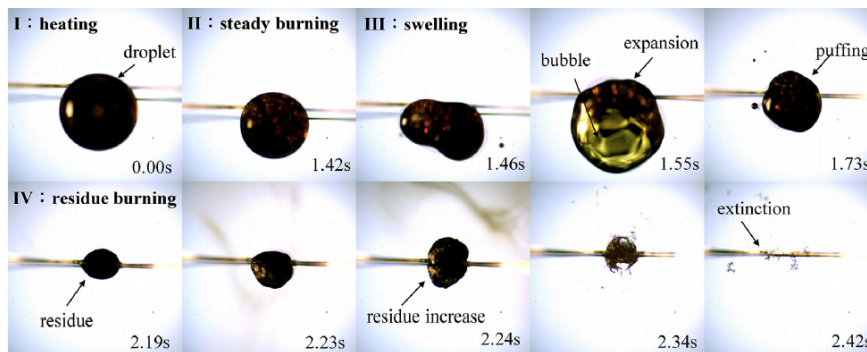


Figure 1.10: Direct color image of single droplet combustion with internal convection effect [28].

If the single droplet is inserted in the hot gas environment, the preheat stage starts which is dominated by a transient processes. Heat flows from the hot surrounding gas to the droplet, causing the droplet temperature to rise.

The ignition of a droplet occurs in the gaseous mixture of fuel and oxidizer surrounding the droplet. BPO is combustible but not flammable; because of the high content of nonvolatile components, pyrolysis oil requires significant energy for ignition, but once ignited, it burns with a stable self-sustaining flame [26, 27, 30].

Quiescent burning (blue flame) follows in which the spherical shape of the droplet is not perturbed. This is the regime where light volatiles diffuse to the surface and evaporate

[26, 27, 30, 36].

Microexplosions are known to exist in rapidly heated mixtures with chemical species of varying volatility. After the initial heat-up period, the droplets evaporate in approximate agreement with the d^2 -law relationship until undergoing explosion. The microexplosion phenomenon is thought to occur by one of two mechanisms that trap volatile components within the droplet. The first mechanism considers the formation of a viscous outer liquid layer (shell) around the lighter volatile components remaining in the core which happens during late droplet evaporation. This shell acts as a barrier to the transfer of lighter components, which allows the droplet temperature to increase beyond the vaporization temperatures of the volatile core. The core is then superheated and rapidly flashes, causing a nearly instantaneous expansion and subsequent microexplosion.[36]. The second mechanism proposes that due to the reactivity of the oil, a polymer shell forms around the volatile core, also occurring during late droplet evaporation. This results in hindering the more volatile species to diffuse to the droplet surface and to evaporate. As the droplet temperature exceeds the boiling temperatures of light components still trapped inside the droplet, droplet swelling and droplet micro-explosion occurs [36]. Rupture of the droplet surface is accompanied by the release of fuel vapor and small droplet fragments observed during the microexplosion [36, 37, 40]. For low temperature range is the predicted volatile evaporation time significantly less than the observed bubbling period. A possible explanation for this anomaly lies in a conversion of some light species to heavier fractions through polymerization, which would reduce evaporation rates and prolong bubbling. Since the droplet temperatures during the bubbling period are very similar regardless of the ambient temperature, polymerization will proceed at roughly the same rate in all cases; however, because of slow evaporation at low temperatures, the time available is much longer, and the degree of polymerization will therefore be larger [49, 66].

After the release of vapor during the microexplosion, oil droplets merge after coalescence, due to high surface tension. Burning at this stage occurs again in a blue flame, fainter than the first, with the release of occasional small bright luminous bursts. The droplet can now have a nonspherical shape and small yet identifiable regions of transparency in the droplet indicating that vapor is still trapped inside droplets at this stage, although droplet swelling is not as pronounced at this longer residence time. Quiescent burning of the oil occurs until the temperature at some position within the droplet reaches the local homogeneous nucleation temperature [27].

Disruptive sooty burning of droplet fragments (bright yellow flame) with formation of cenosphere particles and soot can occur. [26, 27, 30]. Cenospheres are hollow glassy spheres that are often found in solid combustion residue, resulting from the incomplete combustion of fuel droplets. The soot derives from secondary pyrolysis of gas-phase species and visibly forms at late droplet residence times when the heavy volatile fraction evaporates. When mass transfer limitations exist within the droplet, liquid-phase pyrolysis dominates and cenospheres are formed. The remaining solid residuals, however, contain dense glassy solids that are still highly oxygenated [36]. The weight loss during this stage is very high due to evaporation and cracking reactions. Polymerization reactions are also presumably active, ultimately leading to the formation of coke, which in this study is indicated as secondary char (to make a distinction with the primary char, generated from wood pyrolysis) [26]. However, the majority of the droplet lifetime was dominated by a slow even bubbling of hundreds of small bubbles until it formed a dark spherical droplet that slowly shrinks and collapses into a porous char particle. The

droplet keeps its roughly spherical shape throughout its lifetime.

The physical properties of biomass oil also change during a droplet's combustion lifetime, as volatile species evaporate and remaining species undergo thermally induced chemical transformations that could lead to higher viscosity [27]. Properties have an important impact on the behavior of pyrolysis oils during combustion and consequently on the applications for energy production in standard equipment [30].

1.6 Research objective

BPO majorities tend to have considerable affect on power equipment (e.g. pH value, viscosity and moisture) and various studies have been conducted to determine how their undesirable effect can be decreased; the most notable solutions proposed include physical, catalytic, and chemical upgrading. From section 1.5.2, experimentally it is clear that polymerization reactions are active during late evaporation and have a large impact in droplet microexplosion and char formation, but also on droplet evaporation rate.

There are two studies found in literature modeling the heating and evaporation behaviour of BPO. Salleveld et al. [7] applied CFD techniques to model the combustion of pyrolysis oil in a new burner geometry to investigate the influence of the initial droplet size and to evaluate different combustion models. Zhang et al. [41] modeled the vaporization of a single BPO drop and also mixtures of BPO and other practical fuels to investigate the droplet life time of BPO against conventional fuels. These studies do not take into account polymerization reactions thereby neglect the effects in their studies.

Tsekos [61] carried out an experimental study on fast pyrolysis of woody biomass in a pyroprobe reactor to study the effect of torrefaction on the pyrolysis products for his Master's thesis. Currently he is also studying algal biomass. Unfortunately, the biomass components he is focussing on, do not give a (full) overview of the BPO formed. In literature more experiments and more detailed data on components contained in BPO are carried out for lignocellulosic biomass than of algal biomass. Decided is therefore to work with lignocellulosic biomass data from Branca et al. [52].

A first step towards modeling a complete combustion of pyrolysis oil is the ability to model a single isolated heating and vaporizing oil droplet. The focus of this study is to investigate the effect the polymerization reaction on the droplet heating and evaporation but in the absence of droplet microexplosion. Relevant aspects are the multicomponent nature of fuel and the changing thermophysical properties during evaporation. The objectives are as follows:

- (i) Formulation of a surrogate oil to represent a real BPO for computational means;
- (ii) Formulation of thermal polymerization reaction;
- (iii) Model the heating and evaporation behaviour of a single BPO droplet without polymerization reaction and validate against literature data;
- (iv) Model the heating and evaporation behaviour of a single BPO droplet with polymerization reaction and investigate the effects.

1.6.1 Thesis outline

Chapter 2 introduces the theory on surrogate oil formulation and surrogate component selection. Chapter 3 introduces the theory on polymerization reactions of BPO components and the reaction formulation. Chapter 4 gives an overview of existing evaporation models, explains which model is applied for this study and how it is adapted for the multicomponent case. Chapter 5 validates the methods used to estimate thermophysical properties for the BPO droplet and also discusses the results obtained by the evaporation model without and with polymerization reaction. Finally in Chapter 6 conclusion are drawn and an outlook for further developments is provided.

Chapter 2

Surrogate oil formulation

BPO's are complex mixtures of hundreds of organic compounds that belong to the main key functional groups found, i.e. acids, aldehydes, ketones, alcohols, aromatics, esters, (anhydro)sugars, furans, phenols, guaiacols, syringols, water, nitrogen containing compounds and other minor species. See reference [31, 51] for algal biomass derived BPO and [8, 67] for lignocellulosic biomass derived BPO. For the purpose of this study, i.e. modeling the heating and evaporation behaviour of BPO, a surrogate oil must be defined consisting of a few selected organic components such that this oil mimics certain behaviour to be studied of the real BPO because modeling the real BPO is too complex. Two main conditions on the surrogate oil come from the computational and from the experimental viewpoint. Solving the governing equations (for heat and mass transfer) for tens or even hundreds of individual compounds is too computationally expensive while on the other hand not all compounds of BPO can be analyzed by experiments as explained in 1.3.2. And a surrogate should enable testing of the same fuel in different experimental devices, geographic locations and using different analysis techniques so that comparisons can be made without fuel variability complicating interpretation of the results.

A good compromise is to use only a few groups or fractions to represent BPO to capture the most relevant properties for the evaporation behaviour to represent the behaviour of the actual complex fuel. Consequently, due to the complex composition of BPO, it is not feasible to choose a single component to represent the oil, and vaporization modeling needs to be performed using a multicomponent approach based on its actual components and composition. The definition of the surrogate composition for the oil is a challenging task because of the complexity of the original BPO, whose chemical characterization is not known completely. The surrogate oil component selection should be based on two aspects, i) specific physical and chemical targets properties needs to be matched by a particular surrogate mixture [8] and ii) at least one of the selected component must be able to polymerize. The quantities used to compare the performance of a surrogate fuel to the real oil are often termed targets. Figure 2.1 includes terms and the procedure used for formulating the surrogate oil. The term property targets refers to fundamental physical and chemical fuel properties, development targets refers to kinetic and fluid dynamic processes that are important for validating surrogate mixture behavior (typically evaluated on experimental devices) and application targets refers to results obtained from engine experiments. As represented in figure 2.1, verification by experimental techniques (to match development and application targets) is also required, however that is out of scope of this study. Especially for experimental testing of the surrogate oil, aspects in selecting the components such as low components costs (in both buying and for

the purpose for testing), readily obtainability and low toxicity and flammability should be considered as well [8, 51].

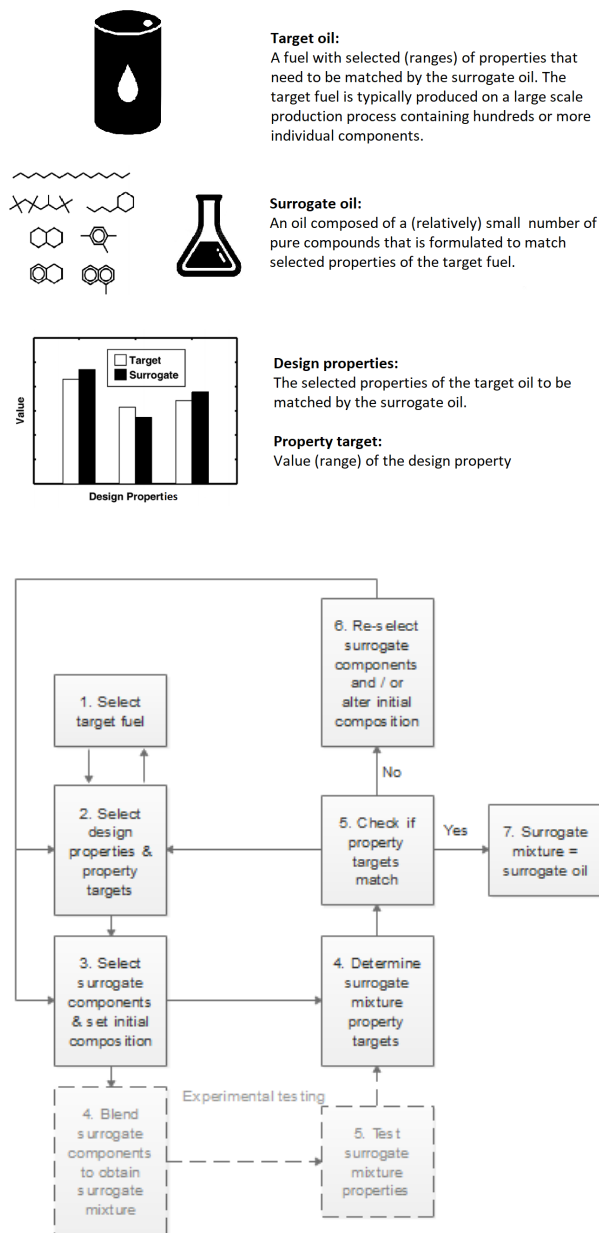


Figure 2.1: Definitions of terms (above) used in this study for the followed formulating process (below) to create the surrogate oil.

Developed surrogates, to characterize multiphase, thermophysical properties and the resulting fuel evaporation processes, are viewed as “physical” surrogates. On the other hand, components selected to mimic fuel chemical kinetics (e.g. chemical reactions, ignition delay and laminar flame speed) are “chemical” surrogate. However, some commonly used chemical surrogates cannot match the physical properties, such as the distillation curve, and are not suitable for analyzing the complex behavior of droplet heating and evaporation. The majority of current surrogate models for hydrocarbon fuels focus on predicting and simulating the distillation curve, evaporation behavior, and kinetics mechanism separately [54]. For the purpose of modeling a multicomponent oil evaporation and combustion process, a “unified” surrogate, that is capable of emulating the physical

and chemical (kinetics) properties of the real liquid fuel at the same time, would be required.

2.1 Formulation methods

There are two types of approaches to formulate a surrogate oil, the continuous thermodynamic (distribution function) model or the discrete component model.

Continuous thermodynamics model

In continuous thermodynamics, a fuel mixture is represented by a probability density function (PDF), $f(I)$, corresponding with a distribution variable I , which could be component molecular weight, carbon number, or boiling point so that the distribution mean is the average molecular mass of the fuel. The continuous thermodynamics theory for multiple distribution functions is developed by Hallett et al. [49, 68, 69]. A representation is given in figure 2.2, where the actual mixture (left) contains a large number of components, far more than one can conveniently measure or make calculations for, shown here as concentrations plotted versus I . These concentrations are represented in continuous thermodynamics with a continuous function y_i (right), so that the concentration of a component with a particular value of I is given by a thin slice out of the $f(I)$. Instead of requiring the concentrations of dozens of components and solving the transport equation for each component, with this principle only the distribution parameters (mean θ and standard deviation σ) of the distribution are required to characterize the fuel as a mixture. Transport equations which are necessary to describe the fuel vapour composition around the droplet allow the distribution function to diffuse rather than the individual fuel components thereby enabling the use of a typical fuel consisting of hundreds of components.

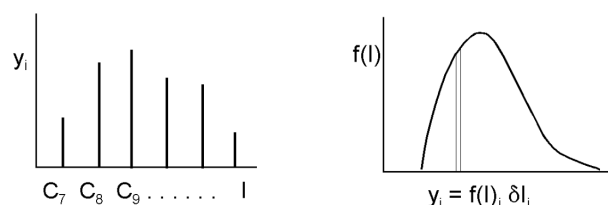


Figure 2.2: Basic principle representation of continuous thermodynamics

Discrete model

The second possibility is to represent the mixture as a finite number of discrete components, which represent a surrogate fuel mixture. A discrete representation easily allows to expand the model with internal chemistry. In an actual BPO droplet, such chemistry includes polymerization of the heavier compounds, which can result in spatial variations of fuel properties, and the break-down of components to form gasses, and char in combustion cases.

Previous studies

For instance, four fractions, namely organic acids, aldehydes/ ketones, water, and pyrolytic lignin, have been successfully used in modelling of evaporation of biomass pyrolysis oil droplets by Hallett and Clark [49] based on the continuous thermodynamic approach. Brett et al. [50] formulated a surrogate based on 12 components to study the effect of internal diffusion on an evaporating bio-oil droplet. Sallevelt et al. [7] developed a 7 component discrete surrogate oil based on the pyrolysis oil devolatilization

characteristics reported by Branca et al. [17], who proposed to divide the devolatilization curve into six main temperature zones. It was shown that the measured weight loss in the zones could be correlated with the mass fractions of the compounds identified in the oil samples of which the boiling points fell within the corresponding temperature ranges. The total weight loss in each of the six temperature zones is lumped into a single organic compound that is typically found in pyrolysis oils. Hossain et al. [51] developed (experimentally) a 5 component surrogate oil based on the chemical compounds contributing the most to the total weight of the real oil, to assess diesel engine performance and exhaust emissions. Pozarlik et al. [18] selected a simple water-phenol surrogate oil to assess the effect of the solid char on the combustion characteristics.

Model selection

It is decided not to use the continuous thermodynamics technique to model the vaporization of BPO, because it is not reasonable to simply relate the physical properties of the components to only one parameter. Furthermore, for a multicomponent fuel composed of only a few components, the discrete component approach is preferred. Therefore, for the purpose of this study, this approach will be used to model for formulating the surrogate oil.

2.2 Characteristics of the surrogate oil

This section describes the BPO behaviour aspects of the real BPO the surrogate oil has to reproduce. From figure 2.1, a target BPO with design properties and targets must be formed from data available in literature. Targets for the surrogate formulation differ depending on the intended application of the surrogate. For studying the heating and evaporation behaviour, a surrogate oil is developed that represents e.g. the volatility, water content, elemental composition, heating value, density and elemental composition of a typical pyrolysis oil. The aforementioned discusses the surrogate characteristics from a property point of view, however a second characteristic includes that at least one of the components from the surrogate oil should be able to undergo a chemical reaction, i.e. thermal polymerization, to form a larger molecule. The latter will be discussed in section 3. Table 2.1 includes obtained literature data for the design properties and targets for the target oil, representing BPO from different sources.

In the table 2.1, for the heating values, only BPO derived from feedstock on dry basis is included, however some sources even determined the heating values from feedstock as received. Also as mentioned in section 1.2.1, the BPO properties are dependent on process operating conditions (e.g. temperature, pressure and pyrolysis reactor type) which are not included in table 2.1. However, the range of targets included in the table are based on typical operating parameters and thus a typical BPO can be derived.

2.3 Surrogate component selection

Literature data on identified main components

Huber et al. [75] have summarized the chemical composition of BPO's, as reported in figure 2.3; this analysis is consistent with a more recent study by Branca et al. [76]. Branca et al. [76] is the most detailed study (till now) regarding chemical composition analysis of BPO from woody biomass originating from four suppliers (BTG - Enschede Netherlands, Dynamotive - Vancouver Canada, Ensyn - Ottawa Canada and Pyrovac - Quebec Canada) at about the same pyrolysis operating conditions. They identified

Table 2.1: Design properties and approximate targets of BPO's which can figure as target oil

Design property	Target range	BPO source	Source	
<i>HHV</i> [<i>MJ/kg</i>]	19.8 - 20.6	forestry residue, pine	[70, 73]	
	22.1 - 24.3	wood, plant waste	[34, 73]	
	18 - 22.5	tropical wood	[71]	
	24.0, 23.7, 29.7, 25.7	wood, straw, lignin, algae	[37]	
<i>LHV</i> [<i>MJ/kg</i>]	14.1 - 17.6	forestry residue, pine	[70]	
	20.9 - 22.2	wood, plant waste	[34]	
	13 - 18	typical BPO	[72, 73]	
<i>LHV</i> dry [<i>MJ/kg</i>]	20 - 21	forestry residue, pine	[70]	
<i>pH</i>	2.4 - 3.5	forestry residue, pine	[70]	
	2.1 - 3.4	wood, plant waste	[34, 73]	
	2.80 - 3.31	tropical wood	[71, 74]	
	3.2, 3.8, 3.9, 4.3	wood, straw, lignin, algae	[37]	
	2.64- 3.44	softwood bark	[74]	
	2 - 3	typical BPO	[72, 73]	
kin. viscosity at 40 °C [<i>cSt</i>]	35 - 135	forestry residue, pine	[70]	
	35 - 100	wood, plant waste	[34, 73]	
	5.7 - 17.4	tropical wood	[71]	
	(80 °C)	11 - 14	softwood bark	[74]
	15 - 35	typical BPO	[72, 73]	
	(90 °C)	15 - 21	softwood bark	[74]
density (15 °C) [<i>kg/dm³</i>]	1.20 - 1.24	forestry residue, pine	[70]	
	1.18 - 1.22	wood, plant waste	[34, 73]	
	1.04 - 1.11	tropical wood	[71]	
	(28 °C)	1.09 - 1.22	softwood bark	[74]
	1.1 - 1.3	typical BPO	[72, 73]	
	specific gravity	1.16 - 1.22	wood, plant waste	[34]
water <i>wt%</i>	16.3 - 32	forestry residue, pine	[70]	
	14 - 31	wood, plant waste	[34, 73]	
	29.99 - 37.10	tropical wood	[71]	
	27.3, 25.7, 27.4, 26.6	wood, straw, lignin, algae	[37]	
	3.5 - 14.6	softwood bark	[74]	
	20 - 30	typical BPO	[72, 73]	
<i>C wt%</i>	38.2 - 46.7	forestry residue, pine	[70]	
	55.10 - 63.5	wood, plant waste	[34, 73]	
	35.01- 44.73	tropical wood	[71]	
	61.3 - 74.1	softwood bark	[74]	
	57.0., 58.8, 65.6, 59.5	wood, straw, lignin, algae	[37]	
	32 - 60	typical BPO	[73]	
<i>H wt%</i>	7.0 - 7.8	forestry residue, pine	[70]	
	5.2 - 7.2	wood, plant waste	[34, 73]	
	7.42 - 8.05	tropical wood	[71]	
	6.5 - 8.0	softwood bark	[74]	
	7.2, 7.6, 8.0, 7.2	wood, straw, lignin, algae	[37]	
	5.9 - 8.6	typical BPO	[73]	
O (difference) <i>wt%</i>	46 - 53	forestry residue, pine	[70]	
	34.81 - 37.70	wood, plant waste	[34, 73]	
	41.93 - 50.27	tropical wood	[71]	
	17 - 31.3	softwood bark	[74]	
	35.3, 31.9, 24.5, 28.5	wood, straw, lignin, algae	[37]	
	30-45	typical BPO	[73]	
<i>N wt%</i>	0.4 - 0.1	forestry residue, pine	[70]	
	0.1 - 2	wood, plant waste	[34, 73]	
	0.5 - 1.25	tropical wood	[71]	
	0.05 - 0.07	softwood bark	[74]	
	0.5, 1.62, 1.7, 4.0	wood, straw, lignin, algae	[37]	
	0.4	typical BPO	[72, 73]	

more than 400 organic compounds of which more than 80 components, according to TGA and DTG curves, have been grouped on the basis of the corresponding boiling temperatures. Figure 2.3 shows the range of compositions that can be found in BPO's. Main families found are organic acids, esters, alcohols, ketones, aldehydes, miscellaneous oxygenates, sugars furans, phenols, guaiacols and syringols. The multicomponent mixtures are derived primarily from depolymerization and fragmentation reactions of the three key building blocks of lignocellulose: cellulose, hemicellulose, and lignin.

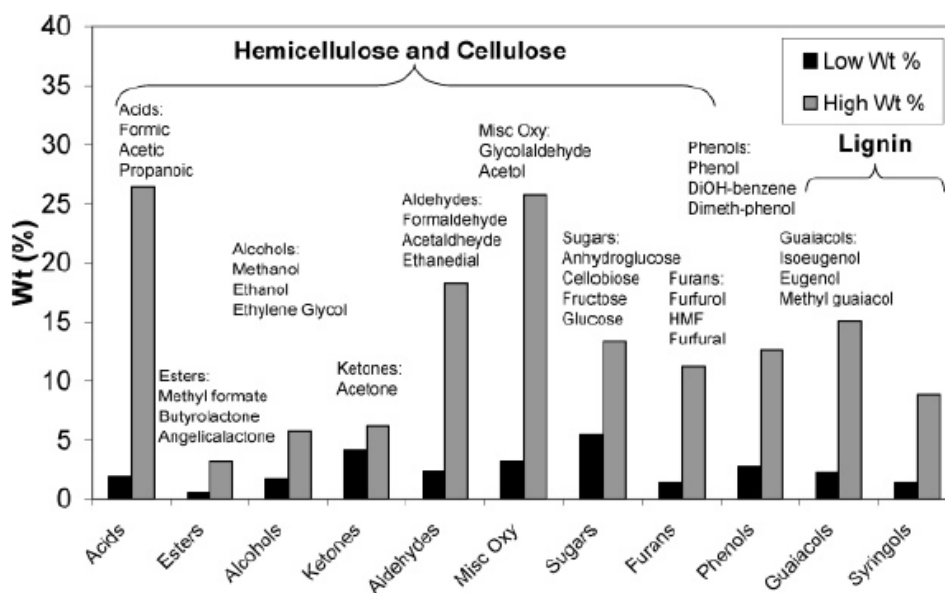


Figure 2.3: Chemical composition of BPO's including the most abundant molecules of each of the components and the biomass fraction from which the components were derived [75].

Component selection

Two ways to select the surrogate components are presented below.

The use of model compounds

Each selected component represents a main organic family, not necessarily a major compound found in that family. The selection of compounds is based on their commercial availability, toxicity and the H/C/O balance of the mixture but also to produce an equilibrium balance between the different classes in the model bio-oil and the required fuel properties [8].

The use of lumped components

The use of lumped components is a more precise model, based on the TGA and DTG data of BPO. Accordingly the peaks and shoulders (temperature) from TGA and DTG data zones can be identified and species, as Branca et al. [76] did, can be grouped based on their boiling temperatures. Then, the species with the largest mass decomposition in each zone can be selected to form the surrogate BPO. Figure 2.4 and table 2.2 gives an illustration of the six main zones in the TGA and DTG curve. All components identified for all four supplied BPO's grouped in six according to the species boiling point temperatures falling in the six identified zones are included in table 1 from reference [76]. This method will be used in this study, since it represents the real BPO more accordingly.

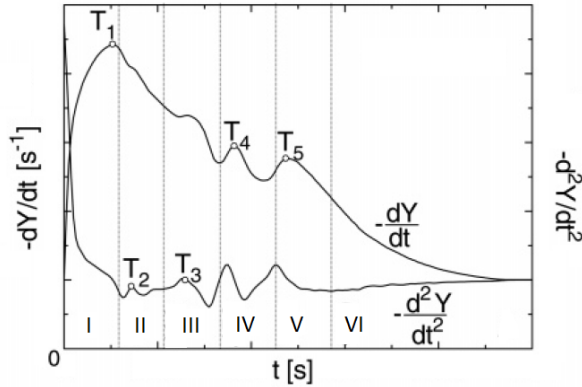


Figure 2.4: TGA and DTG for BPO divided in the identified main six zones. Slightly adapted from [76] from the Dynamotive BPO sample.

The selected components included in table 2.3 are a result from an iterative procedure according to figure 2.1. Step four and five of this procedure are evaluated simultaneously with the procedure as mentioned in section 4.5 only, since evaluating the target properties is also required in the latter section. Iteratively, it is checked if target properties as in table 2.1 are met. Table 2.2 gives an overview of the weight loss of each BPO in each zone including TGA data from woody biomass, reference [29]. For initial mass fraction of the selected component from each zone, the average of the TGA data from all the BPO's from the zone accordingly is taken from table 2.2. In the surrogate fuel developed for this study, the total weight loss in each of the six temperature zones is lumped into a maximum of two organic compounds, having the highest decomposition (as from Table 1 of [76]), and that is typically found in pyrolysis oils. Initial mass fractions of the surrogate fuel components is estimated from table 2.2.

Table 2.2: Weight loss (WL) in wt.% for the different temperature zones as measured using TGA and predicted values based on oil composition and boiling points. Data (Dynamotive, BTG, Pyrovac, Ensyn) reproduced from Branca et al. [76] and (VTT) from van Rossum et al. [29].

Zone	BTG ¹		Dynamotive ²		Ensyn ³		Pyrovac ⁴		VVT ⁵
	TGA	Pred.	TGA	Pred.	TGA	Pred.	TGA	Pred.	TGA
1 [$< 360\text{ K}$]	0.276	0.079	0.167	0.078	0.089	0.040	0.082	0.045	0.28
2 [$360\text{-}400\text{ K}$]	0.166	0.444	0.133	0.332	0.130	0.306	0.108	0.224	0.15
3 [$400\text{-}450\text{ K}$]	0.131	0.065	0.137	0.084	0.121	0.054	0.126	0.054	0.11
4 [$450\text{-}500\text{ K}$]	0.083	0.016	0.097	0.029	0.094	0.026	0.139	0.026	0.08
5 [$500\text{-}550\text{ K}$]	0.057	0.031	0.089	0.047	0.093	0.035	0.088	0.033	0.04
6 [$> 550\text{ K}$]	0.042	0.049	0.060	0.072	0.087	0.041	0.048	0.049	0.16
Full range	0.76	0.68	0.68	0.64	0.61	0.50	0.59	0.43	0.82

¹ 30% water, heating rate 5 K/min up to 600 K based on oil temperature.

² 21% water, heating rate 5 K/min up to 600 K based on oil temperature.

³ 20% heating rate 5 K/min up to 600 K based on oil temperature.

⁴ 15% water, heating rate 5 K/min up to 600 K based on oil temperature.

⁵ Only TGA data; 24% water, heating rate 1 K/min up to 1073 K based on sample cup temperature.

In table 2.3, the molecular weight and the boiling temperature are determined by the Joback method which predicts eleven important and commonly used pure component thermodynamic properties from molecular structure only, see Appendix B.2 more detail on this method follows in section 4.4.1). Figure 2.5 shows the molecular structure of

each selected component. The properties obtained by the Joback method are valid from the melting temperature up to 70% of the critical temperature. If the temperature to be reached by the droplet is exceeding the 70% of the critical temperature of species i , the properties of species i are then set to be as a constant equalling its prior value.

In the modeled bio-oil composition, the mass fraction of water is kept the same as the original water content in bio-oil to best account for the effect of water. The mass fractions of the other nine components are scaled up in order to account for the components neglected. It is thought that the components listed in the table can reasonably represent bio-oil produced from wood pyrolysis. Among the major components considered, the acid compounds, i.e., propionic acid and acetic acid, can account for the low pH value of bio-oil. Levoglucosan is the major product of cellulose degradation. Phenol, syringol, and isoeugenol are the products of lignin pyrolysis. It is noted that the neglected minor components only have trace amounts. Moreover, the minor components in the same group have similar physical properties and each group is already represented by (or lumped into) its dominant component. For instance, (5H)-furan-2-one is chosen to represent the furans. Solid content (less than 1 wt.%) is not considered and it may not affect vaporization because it does not dissolve in the liquid to change the liquid properties [42].

Table 2.3: Selected components for the surrogate oil. $T_{b,i}$ stands for boiling temperature, $Y_{L,i}$ stands for (initial) species i liquid mass fraction and M_i for molecular weight. Superscript numbering stands for species i numbering.

Zone	Component ^{i}	Formula	$T_{b,i}$ [K]	M_i [g/mol]	$Y_{L,i}$ [%]
2 [360-400 K]	Water ¹	H_2O	373	18.02	29
	Acetic acid ²	CH_3COOH	391	60.05	20
3 [400-450 K]	Hydroxypropanone ³	CH_3COCH_2OH	418	74.08	16
4 [450-500 K]	Phenol ⁴	C_6H_5OH	455	94.11	5
5 [500-550 K]	Eugenol ⁵	$C_{10}H_{12}O_2$	527	164.20	11
6 [$>$ 550 K]	Levoglucosan ⁶	$C_6H_{10}O_5$	603	162.14	19

Zhang et al. [41], Frassoldati et al. [8] and Sallevelt et al. [7] are good references which also follow a somewhat similar procedure in selecting components for their surrogate oils.

The, in this case 7th component, resulting from the polymerization, reaction will be discussed in section 3.12.

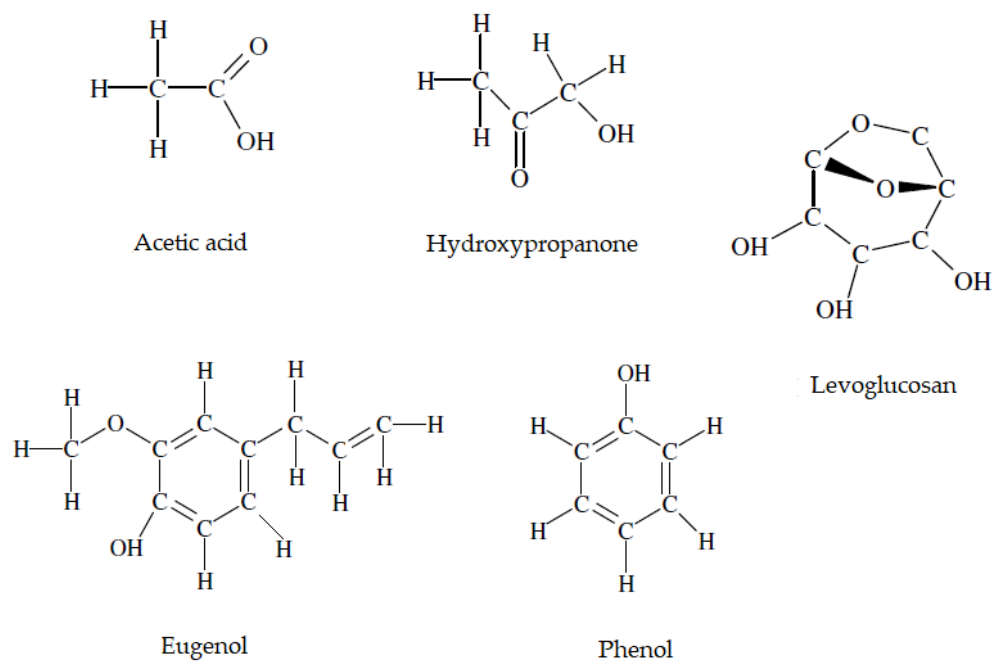


Figure 2.5: Molecular structures of the selected components

Chapter 3

Thermal polymerization reaction

Polymerization of the liquid can take place at temperatures around ≥ 100 °C, which can adversely affect thermophysical properties of the BPO such as increased viscosity (thickening of the BPO is observed) and increased molar mass due to formation of larger molecules, phase separation (water formed as byproduct generates an aqueous phase which tends to separate from the rich oily phase), and formation of solid coke like products (secondary char to distinct with the primary char generated from wood pyrolysis) [3, 5, 17, 18, 26, 29, 73]. The term thermal polymerization stands for polymerization due to temperature increase and not due to catalysis; a purely thermal polymerization is one in which monomer is converted to polymer by thermal energy alone. At low heating rates (1–100 *K/min*), pyrolysis oils show a high tendency to form nonvolatile material under influence of polymerization reactions once the water and light components have evaporated; the amount of solid residue after evaporation decreases with the drop size [7, 25]. However, nearly a third of the mass fraction can not be identified, because analyses of the chemical composition of pyrolysis oil are mainly based on GC-MS, only allowing the determination of vaporizable molecules. It is assumed that many of the unidentified components are sugar oligomers and polymers [13]. This results in difficulty in studying the reactants (BPO components) and products of the polymerization reactions and the reaction itself as mentioned in ref. [17].

These chemical reactions observed are exothermic as can be seen in the differential scanning calorimetry (DSC) curve, figure 3.1, which can be used to observe the changes in energy during a phase transition [28]. DSC is one of the techniques used to determine the heat flow through a sample of BPO with respect to temperature. DSC analysis provides quantitative and qualitative information about physical and chemical changes that involve endothermic or exothermic processes. The thermal decomposition peaks are endothermic for evaporation and exothermic for polymerization reactions (formation heavier compounds) and ultimately char formation. Therefore, in this context the analysis can also be used to detect exothermic chemical reactions based on the provided detailed information on temperature and mass of a BPO sample by the DSC curve.

The DSC curve in figure 3.1 exhibits an increasing trend between 30 - 160 °C, indicating the presence of endothermic reactions and that the primary evaporation of the droplets occurred during this stage. During the stage of liquid-phase pyrolysis, minor endothermic reactions occurred. When the temperature exceeded 300 °C, in the cases with BPO, notable exothermic reactions were observed [28]. Figure 3.1 represents a clear difference in the exothermic region between pure kerosene and a mixture of kerosene with gradually increased BPO. Even though kerosene is a light hydrocarbon fuel, the DSC

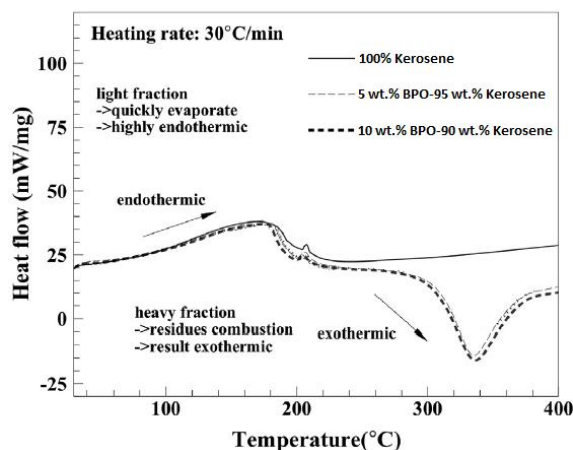


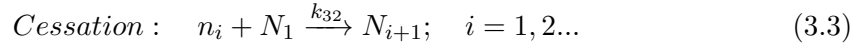
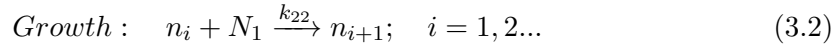
Figure 3.1: DSC curves of kerosene mixed with the dissimilar compositions of the bio-oil [28]. Slightly adapted.

curve represents a much deeper exothermic peak for the mixture with the highest BPO content. This is due to the liquid thermal polymerization reactions in the BPO to formation of larger molecules; combustion of BPO in this region occurs thus for both its initial components and the formed heavier liquid compounds. Frassoldati et al. [8], and Yang et al. [66] have obtained a similar pattern in their DSC curves.

3.1 Reaction types in BPO

There are essentially two types of polyreactions leading to the formation of polymers, namely, (poly)condensation reactions and polymerization reactions in a more restricted sense. The chemical reactions are mainly polymerization of double-bonded compounds, as well condensation reactions occurring between hydroxyl (-OH), carbonyl (C=O), and carboxyl groups (-COOH), to form a larger molecule while simultaneously producing a small molecule (generally water) [5, 17, 26].

Main condensation reactions include esterification (alcohol + organic acid \rightarrow ester + water), transesterification (alcohol + ester \rightarrow different alcohol + different ester), phenol/aldehyde condensation (phenols + aldehyde \rightarrow larger molecule + water), etherification (alcohols \rightarrow ether + water) and homopolymerization (aldehydes \rightarrow polyacetal, oligomers and polymers) [82]. Polymerization mainly occurs between sugar components. The aforementioned reactions are not all the reactions occurring BPO components, but they give an overview of main reactions generating a larger molecule; some of them are included in in figure 3.2 in which only the main pathway is represented. The aforementioned reactions are not a one step mechanism. However it is not the purpose of this study to go into the very detail of the reaction in their step wise mechanisms because defining a reaction in detail is a whole study itself while on the other hand not much is known in literature about these thermally driven reactions (if there is then they are focused on the degradation reactions of larger molecules to smaller ones and not vice versa). Also, the focus of this research is to study the influence of the formation of larger molecules on the BPO evaporation behaviour. In addition of the latter, the ultimate products of polymerization reactions during heating and evaporation of BPO are char and gas.



Equations 3.4 express the change of the relative frequency of each species with time.

$$\left\{ \begin{array}{l} \frac{dN_1}{dt} = -k_{11}N_1 - k_{22}N_1 \sum_{i=1}^{\infty} n_i - k_{32}N_1 \sum_{i=1}^{\infty} n_i \\ \frac{dn_1}{dt} = +k_{11}N_1 - k_{22}N_1 n_1 - k_{32}N_1 n_1 \\ \frac{dn_i}{dt} = +k_{32}N_1 n_{i-1} - k_{22}N_1 n_i - k_{32}N_1 n_i, \quad i \geq 2 \\ \frac{dN_i}{dt} = +k_{32}N_1 n_{i-1}, \quad i \geq 2 \end{array} \right. \quad (3.4)$$

This system satisfies the law of the conservation of mass since equations 3.5 - 3.7 holds.

$$\frac{d}{dt} \sum_1^{\infty} (n_i + N_i) = 0 \quad (3.5)$$

$$\frac{d}{dt} \sum_{i=1}^{\infty} n_i = +k_{11}N_1 - k_{32}N_1 \sum_{i=1}^{\infty} n_i \quad (3.6)$$

$$\frac{d}{dt} \sum_{i=1}^{\infty} N_i = -k_{11}N_1 - k_{22}N_1 \sum_{i=1}^{\infty} n_i \quad (3.7)$$

3.3 Literature data on polymerization reaction kinetics for BPO components

There are only a few studies found concerning thermal polymerization of components found in BPO.

Hu et al. [78] studied experimentally the polymerization of model compounds of BPO in different media (water, acid, methanol, phenol) at temperatures between 90-190°C. It is found that 4 of their model compounds can polymerize to larger compounds: i) levoglucosan to glucose in a water medium, however as temperature is increased glucose tends to degrade to smaller compounds, ii) hydroxyl acetone + guaciol \rightarrow 1-(-4-hydroxyl-3-methoxyphenyl)-2 propanone (PHMP) in water and methanol medium at about 170 °C, iii) levoglucosan/ glucose \rightarrow methyl α -D-glucopyranoside (MGP) only in methanol medium at about 90 °C. Amongst others, the conversion of LG follows a sigmoidal curve.

Bai et al [80] investigated experimentally if LG undergoes polymerization reactions during pyrolysis of BPO. In a molar mass analysis at temperatures between 200 - 310 °C, they detected components with gradually increased molar masses and related that to

dimer (a polymer consisting of 2 LG molecules), trimer and so on.

Houminer et al. [81] also experimentally investigated the disappearance of LG due to polymerization at temperatures between 190 - 210 °C. The rate of disappearance of LG is also follows a sigmoidal curve, see figure 3.3, and they proposed a kinetic reaction to fit that curve. Same trend for sigmoidal curve is found for polymerization by Ginell et al. [79].

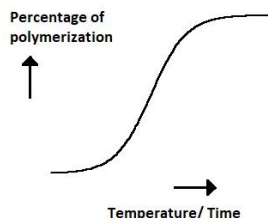


Figure 3.3: Typical sigmoidal curve for a component which undergoes polymerization

Since in most relevant (experimental) studies regarding the polymerization levoglucosan (LG) is only found and since this component is included in the surrogate oil, the reaction will be formulated based on these studies for thermal polymerization of this component only.

Levoglucosan (1,6-anhydro- β -D-glucopyranose), which is one of the major products formed in the thermal depolymerization of cellulose is also known to polymerize both in the presence and absence of acidic catalysts. The polymers obtained from it are branched and contain different glucosidic linkages (a type of covalent bond that joins a carbohydrate (sugar) molecule to another group, which may or may not be another carbohydrate) having α -D or β -D configuration. The dimerization process, in which two LG molecules bond, may proceed through a nucleophilic (nucleophile is a chemical species that donates an electron pair to a reagent attracted to electrons to form a chemical bond in relation to a reaction) attack by a hydroxyl group (-OH) of one LG molecule on the C-1 of another, via a 1,4 linkage. Accordingly, once the dimer has been formed, its primary hydroxyl will be the most reactive group in it and will be preferred for the attack on the C-1 of a third LG molecule, resulting in the formation of (1,6) glucosidic linkage, the dimer. Figure 3.4 gives a representation of the LG molecule, and the formation of its dimer and trimer. The dimer is formed between a -1,4 linkage while the trimer is formed between a α -1,6 linkage. Dimers as well as the higher polymers contain both α -D- and β -D-glucosidic linkages, with unknown type of configuration but polymers obtained from levoglucosan contain about 50% of (1,6) glucosidic linkages. A single chemical reaction is said to be autocatalytic if one of the reaction products is also a catalyst for the same or a coupled reaction. The polymerization reaction, characterized by sigmoid curves, indicates that the process is an autocatalytic one [81].

3.4 Reaction formulation

The scarce quantitative information currently available does not permit the formulation of detailed reaction mechanisms for the reactions described above. Moreover, as already pointed out, even global kinetics is lacking. The global devolatilization mechanism proposed here consists of second order polymerization reaction based on the discussion in section 3.3; it is to be mentioned that such a kinetic reaction model does not show in-

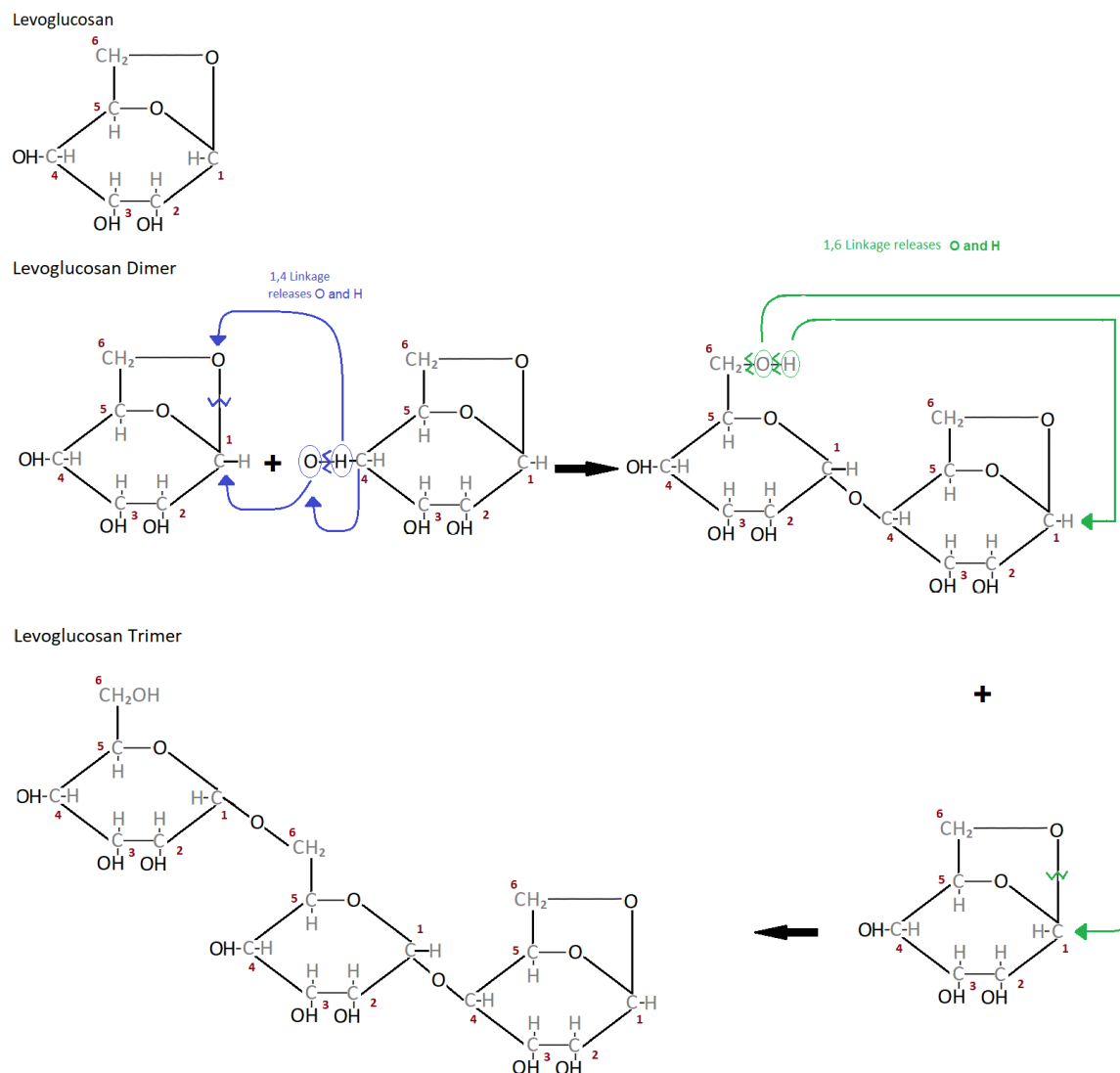


Figure 3.4: Representation of a single Levoglucosan molecule (top), a dimer (mid) and a trimer (bottom) with a 1,4 linkage and a 1,6 linkage respectively. This figure is constructed with information from [81].

sights into the elemental reactions involved.

Temperature of reaction

The temperature of reaction is set to $T_{react} = 180^{\circ}C$.

Assumptions of reaction

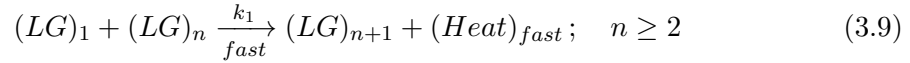
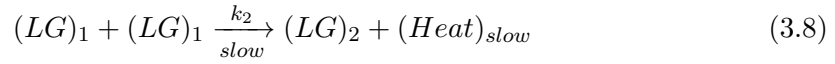
- Reaction occurs between LG molecules only;
- For simplification, organic acids or phenols present in the surrogate BPO will not (catalyze) influence reaction pathway, although these two components are known to catalyze such reactions;
- Irreversible reaction: products will not form reactants again under influence of increased temperatures [77];
- Products will not react with the other components contained in the surrogate oil;

- The reaction is autocatalytic.

Formulation of reaction

A highly simplified mathematical model confirms the explanation is explained below. To follow a sigmoidal curve, a second order reaction is sufficient, without specifying directly if it is a 1 step or 2 step reaction [81, 83].

The polymerization process consists of two different types of reactions (when $n \geq 2$): i) a relatively slow reaction when firstly the dimer is formed, see equation 3.8, and ii) a faster reaction when the dimer proceeds to grow to a trimer and so on, see equation 3.9. Here $(LG)_1$, $(LG)_2$ and $(LG)_n$ are the LG monomer (molecule), dimer and n -polymer respectively and k_1 and k_2 are the reaction rates for the fast and slow reaction respectively. Therefore, the initially slow reaction becomes faster as oligomers are formed. Obviously, at the later stages of the reaction, when the concentration of levoglucosan falls strongly, the rate falls again.



Second order one step reaction: $n = 2$

A one step second order reaction describing the decay of $[LG]$ can be formulated as in equation 3.10. The term $-\frac{d[LG(t)]}{dt}$ is the conversion rate of LG consumption in $mol\ m^{-3}s^{-1}$ and $[LG(t)]^2$ is the concentration of LG at time t in $mol\ m^{-3}$.

$$-\frac{d[LG(t)]}{dt} = k_2[LG(t)]^2 \quad (3.10)$$

The integral form of equation 3.10 results in equation 3.11.

$$\frac{1}{[LG(t)]} = \frac{1}{[LG_0]} + k_2t \quad (3.11)$$

Second order one step reaction with initial first order regime: $n > 2$

The reaction of the form of a one step second order can be formulated as in equation 3.12 where $[LG(t)]$, $[LG_0]$ are the concentration of LG at time t and time $t = 0$ initial concentration. The term $[LG_0] - [LG(t)]$ stands for the amount of LG units that were incorporated into the polymer at time t . This is a reaction that is of a first order reaction in its initial time interval and then transitions to a second order reaction.

$$-\frac{d[LG(t)]}{dt} = k_2[LG(t)]^2 + k_1[LG(t)]([LG_0] - [LG(t)]) \quad (3.12)$$

The integral form of equation 3.12 results in equation 3.13. $\frac{[LG(t)]}{[LG_0]}$ is equal to the percentage of levoglucosan remaining in the reaction mixtures since the volume of the mixture does not change with the conversion.

$$k_1[LG_0]t = \underbrace{2.3 \log \left[1 + \left(\frac{k_2}{k_1} - 1 \right) \frac{[LG(t)]}{[LG_0]} \right]}_Y - \underbrace{2.3 \log \frac{[LG(t)]}{[LG_0]}}_Z - 2.3 \log \frac{k_2}{k_1} \quad (3.13)$$

Reaction rates

Houminer et al. [81] obtained different values for $\frac{k_2}{k_1}$ by plotting $(Y - Z)$ for a variety of $\frac{k_2}{k_1}$ ratios versus t . Straight lines were obtained for all temperatures when $\frac{k_2}{k_1}$ was between 0.1 and 0.3, thus only those ranges for the ratios do count. For the ratio of 0.2 at $T = 210^\circ\text{C}$, a value for k_1 of $4.1 \cdot 10^{-4} \text{ m}^3 \text{ mol}^{-1} \text{ s}^{-1}$ is obtained [81]. The average value thereby for k_2 is $0.82 \cdot 10^{-4} \text{ m}^3 \text{ mol}^{-1} \text{ s}^{-1}$.

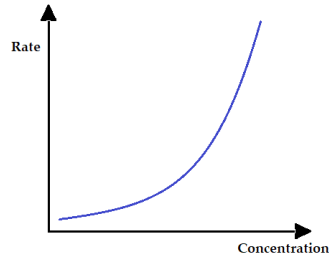


Figure 3.5: Concentration vs rate graph for a second order reaction.

Polymer length

A length n of the polymer should be specified such that the difference in thermophysical properties of the monomer and the n -polymer are notable different. Thermophysical properties might include molar mass, boiling point and heat of evaporation. For the selected surrogate oil components, except for water and methanol, there are no property data bases; experimental data of their physical properties are not (widely) available. The group contribution method, by Ambrose and Joback, described in Reid et al. [55], is used to estimate the properties based on the identified chemical bonds of the molecular structure of each n^{th} polymer, see table 3.1.

Table 3.1: Polymer properties. The -P stands for -phenol, T_b for boiling point, MW for molecular weight, ΔH_{vap} for heat of vaporization (latent heat) and T_m for melting point and the number between brackets stands for the amount of groups identified. Data obtained from Appendix B.2.

n	Formula	Chemical bonds	T_b [K]	M [g/mol]	ΔH_{vap} [kJ/mol]	T_m [K]
1	$C_6H_{10}O_5$	OH-P(3), -O-(2), >CH-(5), -CH ₂ -(1)	603.44	162.141	97.37	
2	$C_{12}H_{20}O_{10}$	OH-P(6), -O-(4), >CH-(10), -CH ₂ -(2)	1025.82	324.28	262.59	840.82
3	$C_{18}H_{30}O_{15}$	OH-P(10), -O-(6), >CH-(15), -CH ₂ -(3)	1688.66	486.423	465.49	1307.59

The critical point data of the dimer, which is needed for further calculations, are $T_c = 1261.71 \text{ K}$ and $p_c = 55.53 \text{ bar}$. Three aspects should be taken into account: i) the state of the polymers (solid/ liquid) according to their melting points, ii) the decomposition of LG at about $\geq 523.15 \text{ K}$ and iii) the decomposition of the polymers before their boiling points.

As can be seen from table 3.1, the melting points of the dimer and trimer are relatively high, higher than the boiling temperature of the monomer which indicates that if the surrogate oil will be heated to a temperature below T_m of at least the dimer, a product of polymerization will occur as a solid. Since temperatures above the T_m of the dimer are unusual in droplet heating and evaporation, for this study it is assumed that only dimers are being formed which are in the solid state (no intermediate and other gradually increased lengths are formed). Furthermore, any decomposition of the selected surrogate components are not taken into account into this study.

Heat of polymerization

The heat of polymerization reaction, ΔH_p , is the enthalpy change that takes place during the formation of the polymer from its monomer (contributed on the right hand side) by the bond enthalpy, at standard pressure and temperature *STP* and the enthalpy from *STP* to the the reaction temperature respectively. The latter is added since the reaction occurs at a higher temperature than surroundings, the calculation is as in equation 3.14 which follows the Kirschhoff's Law (can only be applied to small temperature changes, 100K, because over larger temperature changes, the heat capacity is not constant). The specific heat term $C_{p\tau}$ on the right hand side is assumed to be constant and is determined based on the group-contributions method, i.e. the Chueh and Swanson method as described in section 4.4.1. Conditions for *STP* are $T = 298.15\text{ K}$ and $p = 101.3\text{ kPa}$.

$$\Delta H_p = (\Delta H_{\text{bonds broken}} - \Delta H_{\text{bonds formed}})_{STP} + \int_{T_{STP}}^{T_{drop}} C_{p\tau} \cdot dT \quad (3.14)$$

The T_{drop} and ΔH_p in equation 3.14 stand for the droplet temperature and the bond energies respectively. The latter is determined based on the bonds broken and linkages created in LG polymerization in figure 3.4. For the dimer, the bonds broken are: *C-O*, *H-O* and *H-C* and the bonds formed are: twice a *C-O* bond and once a *H-O* bond. If a bond is formed and then broken again, the energy released in forming a new bond equals the energy needed to break the bond. The first term on the right hand side of equation 3.14 equals thus the bond energy released from breaking the *C-H* bond ($413\text{ kJ} \cdot \text{mol}^{-1}$) minus the *C-O* bond formed ($358\text{ kJ} \cdot \text{mol}^{-1}$) resulting in a $\Delta H_p = 55\text{ kJ} \cdot \text{mol}^{-1}$. For the solid phase isobaric specific heat of the dimer, constant properties are assumed, i.e. specific heat, thermal conductivity and density, listed in table A.2.

Chapter 4

Theoretical model

In understanding the evaporation mechanism, the key parameters such as transient reduction in the droplet size and the time dependent concentration and temperature profiles need to be quantified. There are many single droplet evaporation models reported in literature which are also experimentally and/ or numerically validated.

The mass transfer from the surface of the liquid drop to the ambient is analogous to heat transfer. From the bulk surroundings, hot air flows towards the liquid surface. This hot air warms the liquid layer (where concentration of vapor ≈ 1) and evaporation takes place. Generally it is assumed that gas is not soluble in liquid so the air returns to the bulk flow carrying the fresh vapor along with it. The radius of the drop reduces as evaporation occurs and in this case if radius is zero the mass transfer stops. A schematic of the whole process is shown in figure 4.1, for a one component system.

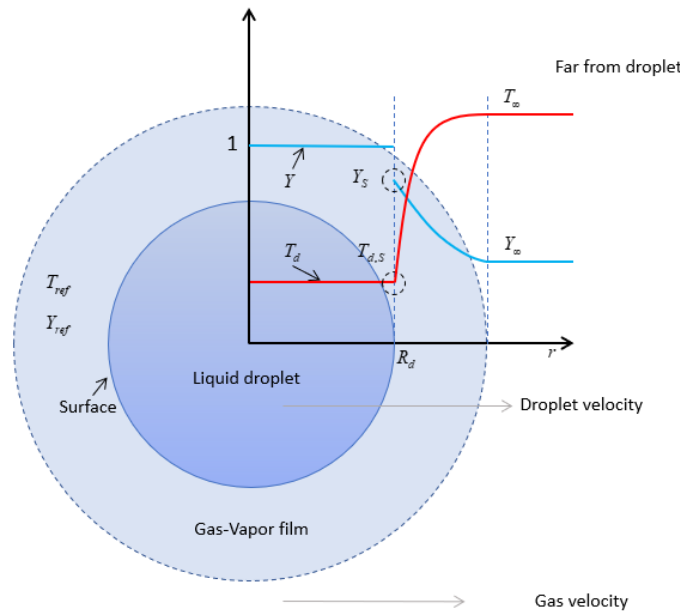


Figure 4.1: Schematic representation of an evaporating droplet surrounded by gas with vapour mass fraction and temperature distributions along the radial direction.

Basically, the existing literature on single-droplet vaporization can be classified into two major categories [48, 43]. In the first category, droplet spherical symmetry is assumed and there are six types of droplet evaporation models. In order of increasing complexity they are i) constant droplet temperature model (which yields the d^2law), ii) infinite-liquid-conductivity model (uniform but time varying temperature of liquid phase), iii)

spherically symmetric transient droplet heating/ conduction limit model, iv) effective-conductivity model, v) vortex model or droplet heating, and vi) Navier-Stokes solution. In the second category, the investigations are based on an axisymmetric model which include the Prakash-Sirignano model (1978, 1980) and the Tong-Sirignano model (1983). The latter consider 2D or 3D modeling and because of their increased effort, they are excluded from this study. Below, an overview of standard single droplet heat transfer and vaporizing models is given. The order in which the subsequent models are introduced below is in increasing complexity.

4.1 Introduction existing evaporation models

The various differences among the models are based on the treatment of the heating of the liquid phase that is usually the rate controlling phenomenon in droplet vaporization. In the first five models a quasi steady gas phase (steady gas phase, unsteady liquid phase) is often considered but that feature is not necessary; models can be constructed to include unsteady gas phases. Generally, the thermal diffusivity in the gas phase is much larger than the liquid phase thermal diffusivity. This implies that transient liquid heating takes longer than the gas phase transient. The first three models can be applied directly in case of no relative motion between the droplet and the ambient gas or in which a correction based on the Reynolds number can be applied to account for convective heat transfer from the gas to the liquid [48].

Constant droplet temperature model: d^2 law

This model applies for a non heating evaporating droplet. A spherical symmetric and isolated droplet immersed in an infinite environment, without convection effects, is considered resulting in a 1D problem of constant and uniform droplet temperature (wet bulb temperature). The liquid does not move relative to the droplet center, the surface regresses into the liquid as vaporization occurs implying that heat and mass transfer in the liquid occurs only due to diffusion within a moving boundary (droplet surface). The d^2 law only holds for single component fuel species thus there is no diffusion term and no ability to analyze liquid phase heat and mass transport, making this model only a gas phase model. The well known d^2 law is the relation in which the square of the droplet radius or diameter, d^2 , reduces linearly in time. See equation 4.1 where $d(t)$ and $d(0)$ are the varying and initial droplet diameter respectively and B_M is the Spalding mass transfer coefficient. The ρ_g , ρ_l and D_g are the density of the gas phase, density of the liquid phase and the diffusion coefficient of fuel vapor in the gas phase respectively.

$$d^2(t) = d^2(0) - \left(8 \frac{\rho_g}{\rho_l} D_g \ln(1 + B_M)\right)t \quad (4.1)$$

Infinite conductivity model ICM/ Rapid mixing model RMM

Two extensions on the d^2 law model are the transient droplet heating phenomena and the diffusion model for multicomponent fuels, which have quite a significant effect on the evaporation process. As a result, the evaporation rate is coupled with a time-dependent energy equation, making use of the infinite liquid conductivity hypothesis. The latter assumes that the droplet has a uniform, but time varying temperature [85, 44] requiring a very small timescale for liquid mixing. Therefore it is applicable in case of very strong internal circulation or extremely small Biot number: $Bi \ll 0.1$ [84]. The volatile components are continuously brought to the droplet surface where they are vaporized.

Further assumptions which can be made are that the liquid mixture vaporizes as an ideal mixture and that there is equal diffusivities between all components (independent of concentration) [43, 48]. When a single species droplet is evaporating, the evaporation rate is determined by the temperature and the rate at which the fuel vapour diffuses away from the surface [38].

Finite conductivity model FCM/ Diffusion limit model DLM

The FCM approach is considered as the most exact model for a spherically symmetric droplet behavior [85]. The RMM model is extended to take into account the spatial (radial) temperature gradient effects, however internal circulation can still be disregarded entirely.

Effective conductivity model ECM

Shear at the vapor-liquid interface causes motion of the liquid at the droplet surface resulting in recirculation of liquid near the surface finally resulting in internal circulation. Heat is transported symmetrically in the liquid phase and purely by conduction. The ECM is an extension of the FCM to account the effect of the internal liquid circulation, by correcting (by an empirical correlation) the liquid thermal conductivity coefficient [43].

Vortex models and Navier-Stokes solution

In vortex model the internal liquid circulation is modeled using a predefined velocity field. The temperature of the liquid-gas interface is uniform but changing in time. More generally Navier-Stokes equations are solved which enables a precise, but quite complex modeling of the evaporation of a droplet [48].

The last two model solve the Navier-Stokes equations and requires high computational time. They cannot be used in spray and turbulent computations and are thus not mentioned further. So either the RMM or the FCM models can be applied. A decision of which of these to select can be made by considering the (heat transfer) Biot number (Bi), defined as in equation 4.2.

The Biot number check

The Biot number, equation 4.2, should be evaluated at the highest temperatures used in further computations, since the thermal conductivity of most liquids decrease with temperature and the number there will be the highest. The h_T stands for heat transfer coefficient, the l_C stands for a characteristic length and the k_L stands for thermal conduction of the liquid phase. Evaluation is carried out at around $T = 500K$ (this estimation was altered during evaporation modeling). The h_T is set to a constant equalling $150 W/m^2K$ [19] (this value is checked again in the procedure to formulate the surrogate oil, i.e. target properties matching). The k_L , is estimated by the Sato-Riedel method, equation 4.3, for the compounds, acetic acid, hydroxypropanone, phenol, eugenol and levoglucosan, while values for water are obtained from the Nist Webbook [91]. In the Sato-Riedel equation, the critical temperatures, $T_{c,i}$, are obtained by the Joback group contribution method as will be explained in section 4.4. The liquid mole fraction, $\chi_{L,i}$, is obtained from equation 4.4. Table 4.1 summarizes the aforementioned.

$$Bi = \frac{h_T l_C}{k_L} \quad (4.2)$$

$$k_L = \frac{\left(\frac{1.11}{\sum \chi_{L,i} M_i}\right) 3 + 20 \left(1 - \frac{T}{\chi_{L,i} T_{c,i}}\right)^{2/3}}{3 + 20 \left(1 - \frac{\chi_{L,i} T b_i}{\chi_{L,i} T_{c,i}}\right)^{2/3}} \quad (4.3)$$

$$\chi_{L,i} = \frac{Y_{L,i}}{\sum_i \frac{Y_{L,i}}{M_i}} \quad (4.4)$$

Table 4.1: Liquid mole fraction and critical temperature of each component as obtained by the Joback method. $T_{c,i}$ and $\chi_{L,i,init}$ stands for the critical temperature and liquid mole fraction of species i .

Component	$\chi_{L,i,init}$	$T_{c,i}$ [K]
Water	0.0632	647.10
Acetic acid	0.1453	593.15
Hydroxypropanone	0.1434	589.06
Phenol	0.569	694.25
Eugenol	0.2185	699.84
Levoglucozan	0.3727	856.72

The obtained thermal conductivity is 0.38 W/mK . For spheres the $l_C = \frac{\text{radius}}{3}$. Assuming a droplet diameter between $50 - 300 \mu\text{m}$, the Bi numbers of $8.721 \cdot 10^{-5}$ to 0.0523 are obtained. Thus the RMM model can be applied.

4.2 Effects and assumptions

Based on the RRM model (the classical model), two extensions include additional effects as discussed below.

Abramzon - Sirignano: Gas-vapor film surrounding the droplet

Due to multicomponent evaporation, mass flux at the droplet boundary in the outward normal direction causes a flow away from the drop, i.e. the Stefan flow. Abramzon and Sirignano [45, 48, 60] revised the ICM to incorporate the effects of Stefan flow on heat and mass transfer, which results in the thickening of the thermal and mass diffusional films. This improvement in the advective transport treatment was achieved by adding two correction factors in the Nusselt and Sherwood number calculations, namely F_T and F_M , which represent the relative change of the thermal and diffusional film thicknesses due to the Stefan flow, in order to take into consideration the fact that a surface blowing results in the thickening of the thermal and mass boundary layers. The finite liquid phase processes can be characterized in terms of liquid Lewis number (Le), defined as the ratio of thermal diffusivity to mass diffusivity used to characterize fluid flows where there is simultaneous heat and mass transfer, or the Peclet number (Pe), which is the ratio of the thermal energy convected to the fluid to the thermal energy conducted within the fluid; if Pe is small, conduction is important. A Lewis number of unity indicates that thermal boundary layer and mass transfer by diffusion are comparable, that temperature and concentration boundary layers almost coincide with each other and thus also that the time scale of thermal and mass diffusion is the same. Mass diffusivity or diffusion

coefficient is a proportionality constant between the molar flux due to molecular diffusion and the gradient in the concentration of the species (or the driving force for diffusion).

Bellan and Harstad: non equilibria at the interface

Till so far is assumed gas-liquid equilibrium at the droplet interface, but for the consideration of small droplets, below 50 μm , and a high difference in droplet velocity and gas velocity (slip velocity), the non-equilibrium phenomenon become significant. Bellan and Harstad [44] proposed a non-equilibrium evaporation model. Generally in the equilibrium case, the Clausius Clapeyron relation is used to obtain surface molar fraction, but in non-equilibrium case, the mole fraction of the fuel vapour at the droplet surface is modified through the non-equilibrium Langmuir-Knudsen law.

Discussion of the previous models

For the high ambient temperature conditions, the heat and mass transfer within the droplet during the vaporization process have also been extensively studied [48]. Aggarwal et al. compared the infinite-diffusion model and diffusion-limited model for the stagnant droplet vaporizing under high temperatures and pressures. It was found that the vaporization curve for these two models are very similar. At the same time, Aggarwal et al. found that the predicted vaporization behavior is significantly more sensitive to the droplet heating than the component distribution within the droplet. This is because the mass transfer rate of the fuel components is much larger than the heat transfer rate within the droplet. In practice, it is necessary to consider the compromise between the computational accuracy and efficiency. From the aspects of saving computational cost and achieving satisfactory predictions, the surface temperature model is particularly important for practical engineering applications. Pinheiro et al. [65] evaluated results from numerical simulations (classical models) against experimental data and their three relevant conclusions were: 1) the Abramzon-Sirignano model is the only one which does not overestimate the evaporation rate for any ambient conditions, 2) incorporating a correction factor for energy transfer reduction due to evaporation in the classical evaporation model results in no difference between this model and the non-equilibrium one even if the initial droplet diameter is small. Therefore the Abramzon-Sirignano model is recommended.

4.3 Theoretical model

4.3.1 Physical model

Figure 4.1 qualitatively illustrates the profiles in the liquid and gas phase: as dictated by the thermodynamics, the temperature is continuous at the interface, but with discontinuous derivative, whereas the species mole fraction has a jump across the interface. A schematic representation of the heat and mass transfer across the droplet interface are included in figure 4.2 and 4.3 respectively. In the latter, the heat of polymerization is becoming available in the droplet volume.

The evaporation of an isolated droplet can thus be explained in the next four steps; i) the heat in the gas phase diffuses to the droplet surface, ii) the heat arriving to the droplet surface is diffused inside the droplet, iii) the molecules of fuel detach from the droplet surface due to their increased internal energy (vaporization process) and iv) the gaseous fuel is diffused from the droplet surface to the surrounding gas.

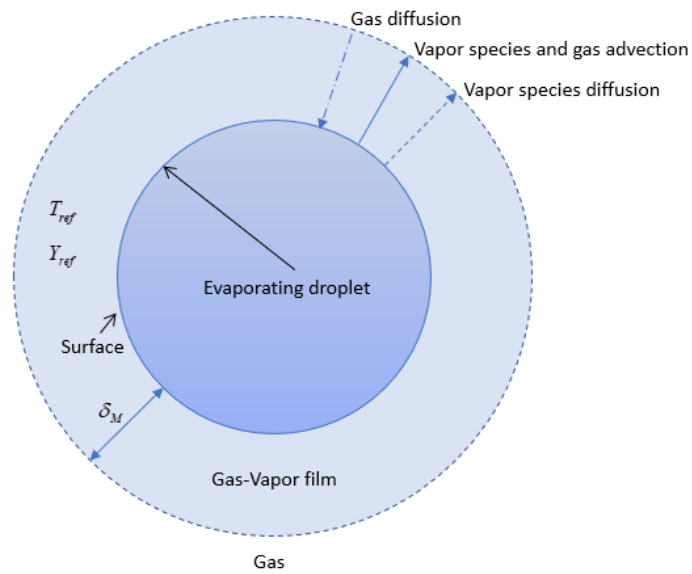


Figure 4.2: Schematic representation of the mass transfer during evaporation of a droplet.

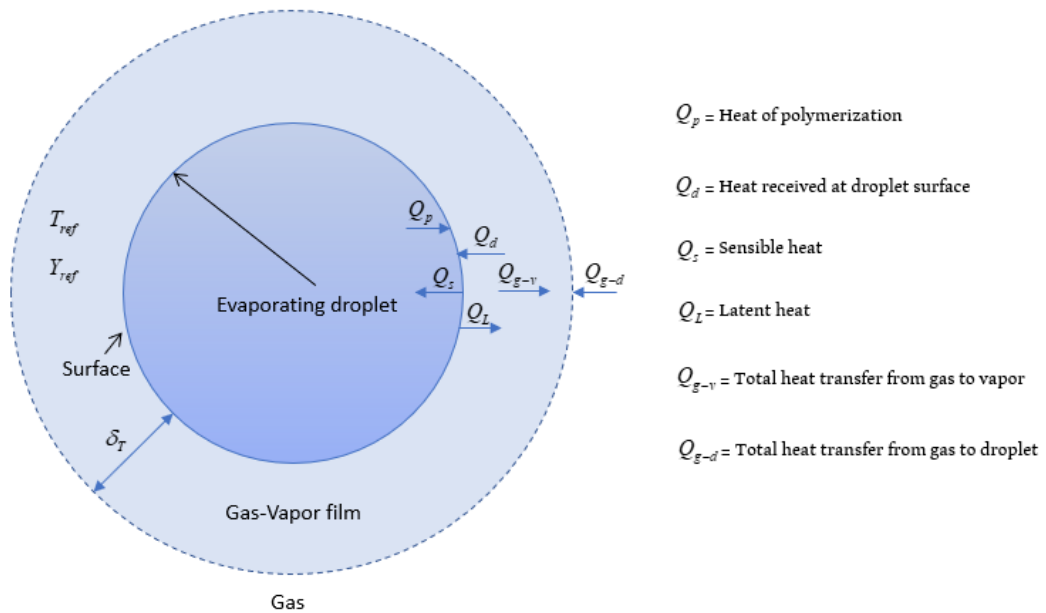


Figure 4.3: Schematic representation of the heat transfer during evaporation of a droplet.

4.3.2 Droplet environment

Modeling is carried out from the point of the droplet and therefore the assumptions made are listed below. The following assumptions made for the Classical Model are as follows:

- Isolated (non interacting) and stagnant single droplet in still air;
- No forced convection.
- The Soret and Dufour effects are neglected
- A zero gravity environment;
- Constant atmospheric pressure field for both environment and droplet phase;
- Surrounding gas, which is consisting of gas (air) and vapor is considered to behave as ideal gas;
- Gas far away from the droplet surface, at ∞ , has a fixed temperature and uniform pressure field ; pressure and temperature for conditions are $p = p_\infty = 101,325 \text{ kPa}$ and $T_\infty = 800 \text{ K}$ respectively;
- Thermodynamic equilibrium prevails at the droplet surface. This holds only for low to moderate pressures, which is also the case;
- Diffusion of the vapor in the gas phase is binary;
- Heat and mass transport in the gas phase are quasi-steady. This assumption indicates that the gas-phase immediately adjusts itself to the local boundary conditions and droplet size at each instant of time;
- The components in liquid phase are well mixed;
- Initial droplet size is $100 \text{ }\mu\text{m}$;
- Gas is not soluble in the liquid phase;

4.3.3 Evaporation Model

Mass diffusion model

Variable thermophysical properties have to be used inside the droplet and surrounding gas to account for the variation of temperature and concentration during the evaporation process. Assuming that the gas phase is insoluble in the liquid phase, the oil mass balance at the droplet surface is given as in equation 4.5 [48]. Here, \dot{m}_S , \dot{m}_d and $\sum_i J_{S,i}$ stands for the mass flow of the fuel vapor at the droplet surface, the total exchanged mass flow at the droplet surface which equals the liquid mass flow due to Stefan flow at the droplet surface, and the diffusive mass flux respectively.

$$\dot{m}_S = \dot{m}_d + \sum_{i=1}^7 J_i \quad (4.5)$$

Introducing the diffusive mass flux (for species i in the fuel) expressed by Ficks law, equation 4.6, equation 4.7 is obtained in which R , ρ_V , D_i and $\frac{\partial Y_i}{\partial r}$ stands for droplet radius, the vapor mixture density, the binary diffusion coefficient of vapour in air and

the change of the vapor mass fraction Y_i of species i from the surface of the droplet in the radial direction respectively. Furthermore, the \overline{D}_F stands for the fuel vapor average diffusion coefficient into the vapor-gas mixture surrounding the droplet. For the (fuel) vapor-gas mixture surrounding the droplet, the empirical $\frac{1}{3}$ rule is applied, see equation 4.11, in which subscripts S , ∞ and ref stand for the droplet surface, far away from the droplet surface and reference conditions respectively.

$$J_i = -4\pi R^2(\rho_V D_i)_{ref} \frac{\partial Y_i}{\partial r} \quad (4.6)$$

$$\dot{m}_d = Y_{S,F}(\dot{m}_d) + 4\pi R^2(\rho_V \overline{D}_F)_{ref} \frac{\partial Y_F}{\partial r} \Big|_{r=R=S} \quad (4.7)$$

Introducing the Spalding mass transfer number (to take into account the Stefan flow effect), equation 4.8, and the Sherwood number, equation 4.9, equation 4.10 is obtained [48]. Equation 4.10 accounts for the total mass evaporating from the droplet surface.

$$B_M = \frac{Y_{S,F} - Y_\infty}{1 - Y_{S,F}} \left(= \frac{\rho_{V,S} - \rho_{V,\infty}}{\rho_{g,S}} \right) \quad (4.8)$$

$$Sh = -\frac{2R}{Y_{S,F} - Y_\infty} \frac{\partial Y_{S,F}}{\partial r} \Big|_{r=R=S} \quad (4.9)$$

$$\dot{m}_d = -2\pi R(\rho_V \overline{D}_F)_{ref} Sh B_M \quad (4.10)$$

$$T_{ref} = T_S + \frac{1}{3}(T_\infty - T_S); \quad Y_{ref} = Y_S + \frac{1}{3}(Y_{\infty,F} - Y_{S,F}) \quad (4.11)$$

The unknown Sherwood number is determined by integrating the mass balance in the normal direction of the width of the boundary layer resulting in equation 4.12, where after equation 4.13 is obtained.

$$\frac{Sh}{Sh_0} = \frac{\ln(1 + B_M)}{B_M} \quad (4.12)$$

$$\dot{m}_d = -2\pi R(\rho_V \overline{D}_F)_{ref} Sh_0 \ln(1 + B_M) \quad (4.13)$$

Equations 4.5 to 4.13 hold for the case if the fuel is a single component fuel. These equations are now modified for the multicomponent case where the species mass evaporation rate, \dot{m}_i , is obtained. The total mass balance for the mass leaving at the surface of the droplet is now expanded for each species leaving the droplet by introducing the species evaporation ratio ϵ_i , as in equation 4.14. Here, $Y_{S,i}$ and \dot{m}_i stands for the surface vapor mass fraction of species i and the species mass evaporation from the droplet surface respectively. Assuming that the mixture of vapour species can be treated as a separate gas, similar to treating the mixture of nitrogen, oxygen and carbon dioxide as air, the following holds $Y_S = \sum_i Y_{S,i}$. Using the definition of vaporization rate fraction, equation 4.7 can now be rewritten as in equation 4.15.

$$\epsilon_i = \frac{\dot{m}_i}{\dot{m}_d} = \frac{Y_{S,i}}{\sum_i Y_{S,i}}; \quad \sum_{i=1}^n \epsilon_i = 1 \quad (4.14)$$

$$\epsilon_i \dot{m}_d = Y_{S,i} \dot{m}_d + 4\pi R^2 D_i \frac{\partial Y_{S,i}}{\partial r} \quad (4.15)$$

According to the quasi-steady assumption for the gas phase and considering mass conservation of each species i in the vapor phase, ε_i is constant along the radial direction. Assuming constant diffusivity and density and integrating equation 4.15 from the drop surface $r = R$ to infinity, the species mass evaporation from the droplet surface is obtained as in equation 4.16. Here $d = 2R$ is the droplet diameter, $B_{M,i}$ is the species Spalding mass transfer number as in equation 4.17, $Sh_{i,0}$ is the species dependent Sherwood number and D_i is the diffusion coefficient of species i in the vapor-gas mixture surrounding the droplet.

$$\dot{m}_i = \dot{m}_d \varepsilon_i = -\pi \varepsilon_i d \rho_{V,S} D_i Sh_{i,0} \ln(1 + B_{M,i}) \quad (4.16)$$

$$B_{M,i} = \frac{Y_{S,i} - Y_{\infty,i}}{\varepsilon_i - Y_{S,i}} \quad (4.17)$$

No equal diffusivities of the components is assumed so there will be a time dependent species concentration in the droplet and at the droplet surface. In equations 4.14 and 4.17 the vapor mass fraction at the surface, $Y_{S,i}$, is determined by the mean molecular weight of the vapor mixture definition and the ideal gas law, as in equation 4.18. The latter is carried out under the assumption of vapor liquid equilibrium existence between the liquid and gas phases at the interface resulting that the vapor mass fraction at the interface equals the saturated vapor mass fraction. The vapor mass fraction far away from the droplet, $Y_{\infty,i} = 0$ for pure vaporization because of the dilution with surrounding air.

The $Y_{S,i}$ is related to the (saturated) vapour mole fraction of each species i at the droplet surface, $\chi_{S,i}$, as in equation 4.18. For vapor phase, air is seen as the 8th component. The $\chi_{S,i}$ the ratio between the partial vapour pressure of the species i and total pressure. At atmospheric pressure partial pressure can be obtained by the phase equilibrium assumption at the droplet interface, which relates the mole fractions of the component in both phases at the phase interface (drop surface) needs to be used as in equation 4.19. $p_{V,i}$ is the partial vapor pressure of species i which is a function of the droplet temperature T_d . More detail on how the $p_{V,i}$ is obtained is given in section 4.4.

$$Y_{S,i} = \frac{\chi_{S,i} M_i}{\sum_i \chi_{S,i} M_i}; \quad \chi_{S,8} = 1 - \sum_{i \neq 8} \chi_{S,i}; \quad i = 1 \dots 7, 8 \quad (4.18)$$

$$\chi_{S,i} = \chi_{L,i} \frac{p_{V,i}(T_d)}{p_{\infty}} \quad (4.19)$$

The liquid mole fraction, $\chi_{L,i}$, is obtained from equation 4.4 and T_d is the droplet temperature which will be obtained through solving the differential equation as explained later.

In equation 4.16, $\rho_{V,S}$ is the density of the gas and vapor mixture and D_i is the diffusion coefficient of species i into the vapor-gas mixture surrounding the droplet consisting of 1. water, 2. acetic acid, 3. hydroxypropanone, 4. phenol, 5. eugenol, 6. levoglucosan, 7. dimer and 8. air. To account for external convection around the droplet in for e.g. a combustor, this value is corrected using the Ranz-Marshall correlation, equation 4.20.

$$Sh_{i,0} = 2 + 0.552 Re_g^{1/2} Sc_{i,g}^{1/3} \quad (4.20)$$

In which the gas Reynolds number, Re_g , and the species dependent Schmidt number, $Sc_{i,g}$, are determined from equation 4.21 and 4.22 respectively.

$$Re_g = \frac{\rho_g |\mathbf{u}_g - \mathbf{u}_d| d}{\mu_m} \quad (4.21)$$

$$Sc_{i,m} = \frac{\mu_m}{\rho_g D_{i,m}}; \quad (4.22)$$

In the Reynolds number, $|\mathbf{u}_g - \mathbf{u}_d|$ is the slip velocity; the difference in the free stream gas velocity, \mathbf{u}_g , and the droplet velocity, \mathbf{u}_d . A stagnant droplet having a $\mathbf{u}_d = 0$ resulting in $Re_g = 0$ and $Sh_{i_0} = 2$ (this holds for the stagnant spherical droplet in a static atmosphere).

The change of droplet diameter with time is determined by taking time derivative of equation 4.16 resulting into equation 4.23; the first differential to be solved. If the T_{react} is reached, the mass of LG in the droplet (liquid phase) $m_{6(new)}$ will decrease due to its disappearance to form the Dimer. A very fast reaction is governed by mass transfer, but a very slow reaction is governed by kinetics. In equation 4.23, ρ_L stands for the liquid density. Updating of ρ_L can lead to thermal swelling, $d(new) > d(old)$. If the reactions starts, the droplet will consists of a solid-liquid mixture. The ρ_{eff} in the second part of equation 4.23 stands for the effective density of the solid-liquid mixture considering both liquid and solid phase and is obtained by equation 4.24. Here, ρ_S , V_L and V_S stands for the solid dimer density, the liquid volume and the solid volume respectively.

$$\left\{ \begin{array}{l} T_d < T_{react}, \\ \frac{dd}{dt} = \frac{2 \sum_i \dot{m}_i}{\pi \rho_L d^2}; \quad i = 1 \dots 6 \\ \\ T_d \geq T_{react}, \\ \frac{dd}{dt} = \frac{2 \sum_i \dot{m}_i}{\pi \rho_{eff} d^2}; \quad i = 1 \dots 7 \\ \\ \frac{d(m_6)}{dt} = - \left[\frac{d[LG(t)]}{dt} \right] \cdot \frac{1}{6} \pi d^3 M_6 = - \left[k_2 \cdot \left(\frac{Y_{L,6} m_d}{\frac{1}{6} \pi d^3 M_6} \right)^2 \right] \cdot \frac{1}{6} \pi d^3 M_6 \\ \\ \frac{d(m_7)}{dt} = - \frac{d(m_6)}{dt} \end{array} \right. \quad (4.23)$$

$$\rho_{eff} = \left(\frac{V_L}{V_L + V_S} \right) \rho_L + \left(1 - \left(\frac{V_L}{V_L + V_S} \right) \right) \rho_S \quad (4.24)$$

Heat diffusion model

The heat diffusion is studied only at the droplet interface. Several energy contributing terms exists which can be divided in heat going from the surrounding gas to the droplet and the heat released from the droplet, see figure 4.3. Broken down, the needed heat terms are: the heat needed for evaporation, latent heat: $Q_L = L_V \sum_i \dot{m}_i$, the heat needed for heating up the droplet, sensible heat: $Q_S = m_d C_{p,L} \frac{dT_d}{dt}$, the convective heat transfer from the gas phase to the liquid phase, $Q_d = h_m A (T_{ref} - T_d)$ and the heat released consists of the heat released due to polymerization reaction, see equation 4.25.

$$Q_p = \Delta H_p \frac{d(m_7)}{dt} \frac{1}{M_7}; \quad \text{for } T_d \geq T_{react} \quad (4.25)$$

Liquid phase convective and conductive heat and gas phase conductive heat are neglected. Rearranging those terms and introducing the Nusselt number, Nu in equation 4.27, the second differential equation 4.26 to be solved is obtained. The Re_g is calculated as in equation 4.21 and the Prandtl number, Pr , needed for the Nu is calculated by equation 4.28. Additionally, the Nusselt number is defined as $Nu = \frac{hd}{k_g}$, where h and k_g stands for the convective heat transfer coefficient and the thermal conductivity of the vapor-gas mixture respectively.

Some assumptions made for arranging the heat balance at the droplet interface are as follows:

- Several researchers have shown that except for large droplets (mm size) of the very heavy fuel oils, radiant heat transfer from the hot gas or from adjacent droplets is negligible;
- Thermal energy transfer between liquid and gaseous phases is assumed to occur only through convection (neglecting radiation and internal recirculation flow);
- Thermal conduction from the gas phase (surrounding droplet) to the liquid phase is neglected;
- Thermal conduction in the liquid phase occurs infinitely fast;
- Since internal circulation is neglected, the thermal convection in the liquid phase is neglected too;
- The enthalpy diffusion flux in the multicomponent energy equation is a well-known yet frequently neglected term. It accounts for energy changes associated with compositional changes resulting from species diffusion. In the gas phase, enthalpy diffusion is neglected due to its small contribution in the energy phase. In the liquid phase, the energy transport by conduction is so large that the enthalpy term can also be neglected.

$$\begin{cases} T_d < T_{react}, \\ \frac{dT_d}{dt} = \frac{\pi d Nu_0 k_m G}{C_{p,L} m_d} (T_{ref} - T_d) + \frac{L_{V,m}}{C_{p,L}} \sum_i \frac{\dot{m}_i}{m_d} \\ \\ T_d \geq T_{react}, \\ \frac{dT_d}{dt} = \frac{\pi d Nu_0 k_m G}{C_{p,eff} m_d} (T_{ref} - T_d) + \frac{L_{V,m}}{C_{p,eff}} \sum_i \frac{\dot{m}_i}{m_d} + \frac{\Delta H_p}{C_{p,eff} m_d} \frac{d(m_7)}{dt} \frac{1}{M_7} \end{cases} \quad (4.26)$$

$$Nu_0 = 2 + 0.552 Re_g^{1/2} Pr_m^{1/3} \quad (4.27)$$

$$Pr_m = \frac{C_{p,m} \mu_m}{k_m} \quad (4.28)$$

In equation 4.26, subscript m stands for vapor-gas mixture and $C_{p,L}$, k_m , L_V and G stands for the specific heat of the liquid mixture, the vapor phase thermal conductivity,

the latent heat and the heat transfer correction factor respectively. The latter is included to take into account a decrease in heat transfer from the surrounding gas to the droplet as a result from the Stefan flow of vapor around the droplet surface). The G factor is calculated as in equation 4.29 in which β is a non-dimensional evaporation parameter calculated as in equation 4.30. Following from equation 4.21, the Reynolds number for a stagnant droplet (in still air) is zero resulting in a $Nu_0 = 2$.

$$G = \frac{\beta}{e^{\beta} - 1} \quad (4.29)$$

$$\beta = -\frac{(\sum_i \dot{m}_i) c_{p,m}}{2\pi k_m d} \quad (4.30)$$

After the reaction starts, the effective heat capacity ($C_{p,eff}$ in equation 4.26) is defined to consider both liquid and solid phase and is obtained by equation 4.31 [105].

$$C_{p,eff} = \left(\frac{V_L}{V_L + V_S} \right) C_{p,L} + \left(1 - \left(\frac{V_L}{V_L + V_S} \right) \right) C_{p,S} \quad (4.31)$$

where $C_{p,S}$ stands for the specific solid dimer heat capacity.

4.3.4 Abramzon-Sirignano model

An extension now made is that the droplet now has a relative velocity with respect to its surrounding gas (moving droplet with a velocity parallel to the gas velocity). In this situation a higher droplet evaporation rate is expected. The Nu_0 and the Sh_0 from the Ranz-Marshall correlation are will now ≥ 2 since the Re_g is now a nonzero term.

The classical gas-film theory assumes that the resistance to heat and mass transfer from the non-vaporizing particle and gas flow may be modeled by introducing diffusional and thermal boundary layer of constant thickness. But this does not include the Stefan flow (blowing effect) which thickens the laminar boundary layer and thereby modifies the heat and mass transfer process. The mass transfer in the outward normal flow caused by the Stefan flow, now causes a gaseous film and thickening of the film both for thermal energy and mass transfer. The film conditions are the same as the reference conditions as defined by equation 4.11. The correction factors for the thicknesses of the diffusional and thermal films, F_M and F_T are calculated using equations 4.32 [65]. Here the B_M is calculated from equation 4.8. The B_T is the heat transfer number calculated as in equation 4.33 to 4.35.

$$F_M = (1 + B_M)^{0.7} \frac{\ln(1 + B_M)}{B_M}; \quad F_T = (1 + B_T)^{0.7} \frac{\ln(1 + B_T)}{B_T}; \quad (4.32)$$

$$B_T = (1 + B_M)^{\varphi} - 1 \quad (4.33)$$

$$\varphi = \frac{c_{p,V}}{c_{p,g}} \frac{Sh^*}{Nu^*} \frac{1}{Le_m} \quad (4.34)$$

$$Le = \frac{k_m}{c_{p,m} D_{V,m} \rho_m} \quad (4.35)$$

In equation 4.35 the Lewis number is calculated based on the mixture-averaged diffusion coefficient, \overline{D}_i . Now the 'modified' Sherwood number Sh^* and Nusselt number Nu^* can

be calculated as in equation 4.36

$$Sh^* = 2 + \frac{Sh_0 - 2}{F_M}; \quad Nu^* = \frac{Nu_0 - 2}{F_T} \quad (4.36)$$

In the mass and energy diffusion model, equation 4.23 and 4.26 respectively, instead of the Sh_0 and the Nu_0 , the modified numbers Sh^* and Nu^* corrected for Stefan flow must be applied. The thermal and mass film thickness are obtained by equation 4.37.

$$\delta_T = F_T \frac{d}{Nu_0 - 2}; \quad \delta_M = F_M \frac{d}{Sh_0 - 2} \quad (4.37)$$

The heat transfer correction factor G is now determined as in equation 4.38. The Nusselt number Nu_0 in droplet temperature change, equation 4.26, should be substituted with the real Nusselt number now from equation 4.39. The same hold for the Sherwood number Sh_0 from equation 4.23 that should be substituted with the Sh from equation 4.39.

$$G = \frac{\ln(1 + B_T)}{B_T}; \quad (4.38)$$

$$Nu = \frac{\ln(1 + B_T)}{B_T} Nu^*; \quad Sh = \frac{\ln(1 + B_M)}{B_M} Sh^* \quad (4.39)$$

As in other approximate models, the film model assumes that the distribution of the temperature and fuel vapor concentrations along the droplet surface are uniform. This assumption may cause some under estimation of the droplet vaporization rate since the nonlinearity of the relationship between the local surface temperature and fuel vapor pressure (Clausius- Clapeyron equation) does not justify the usage of the same relation for the surface-averaged values [42].

4.4 Evaluation of thermophysical properties

The evaporation model is strongly dependent on the thermophysical properties, therefore optimal methods should be applied in obtaining those properties. The different methods available to obtain the relevant thermodynamic (T_c , p_c , p_V , ρ , c_p and L) and transport properties (k , μ and $D_{i,m}$) are discussed in this section. Methods discussed here are methods which are valid for the temperature range used in the evaporation model and methods which are most accurate (for organic molecules) as stated in literature. Mixture properties are obtained by firstly determining the species properties using the methods discussed below, and secondly by applying the mixing rules from table B.1.

4.4.1 Thermodynamic properties

Normal boiling point

The normal boiling point of a fluid is the temperature in Kelvin at which the vapor pressure is equal to one atmospheric pressure.

Yuan method

The method proposed by Yuan et al. [99] is as in equation 4.40.

$$T_b = 218.49 \cdot \ln(CN) - 6.933 \quad (4.40)$$

where CN is the number of carbon atoms in the molecules.

Reid's method

Another one is the model proposed by Reid et al. (as mentioned earlier) is based on the group contributions method, see Appendix ($T_b = 198 + \sum_k N_k \cdot T_{b_k}$), where N_k represents the number of the contributing groups of atoms and T_{b_k} the boiling temperature of each of the groups, see table B.2

Critical properties

There are a large number of other group/ bond/ atom methods for estimating critical properties. From ref. [55], they either are restricted to only certain types of substances such as paraffins, perfluorinated species, alcohols, etc., or they are of lower accuracy.

Joback method

Critical pressure p_c and critical temperature T_c are used as key inputs for physical properties approximations. One method is based on the Joback group contribution method as in tables B.3 and B.4.

Constantinou and Gani method

Constantinou and Gani [55] developed an advanced group contribution method based on the UNIFAC groups which allow for more sophisticated functions of the desired properties and also for contributions at a "Second Order" level. The latter includes the position and connectivity of each group by a formulation of a function $[F]$ of a property F is and is given as in equation 4.41.

$$F = f \left[\sum_k N_k (F_{1k}) + W \sum_j M_j (F_{2j}) \right] \quad (4.41)$$

where f can be a linear or nonlinear function (see equation 4.42 for critical temperature $[K]$ and 4.43 for critical pressure $[bar]$), N_k is the number of First-Order groups of type k in the molecule; F_{1k} is the contribution for the First-Order group labeled $1k$ to the specified property, F , M_j is the number of Second-Order groups of type j in the molecule, and F_{2j} is the contribution for the Second-Order group labeled $2j$ to the specified property, F . The value of W is set to zero for First-Order calculations and set to unity for Second-order calculations.

$$T_c = 181.128 \cdot \ln \left[\sum_k N_k (T_{c_{1k}}) + W \sum_j M_j (T_{c_{2j}}) \right] \quad (4.42)$$

$$p_c = \left[\sum_k N_k (p_{c_{1k}}) + W \sum_j M_j (p_{c_{2j}}) + 0.10022 \right]^{-2} + 1.3705 \quad (4.43)$$

Note that T_c does not require a value for T_b and has a somewhat higher error than the Joback method, which also holds for the p_c [55]. Due to the latter and the more intense Constantinou and Gani method, the Joback method is chosen to work with.

Latent heat

Many estimation methods for the enthalpy of vaporization of pure compounds have been reported based on abundant experimental data. Some equations for estimating the enthalpy of vaporization are derived from the slope of vapor pressure equations according to the Clausius-Clapeyron equation, such as the Antoine equation and the Wagner equa-

tion. However, these methods require polynomial constants (from experimental data), which are scarce for most pyrolysis oil components. Furthermore, the use of these equations is limited to the range of original vapor pressure equations, and the estimation accuracy also depends on them.

Relations for the latent heat of vaporization at boiling point, L_{V_b} , are given below followed by relations for the variations in latent heat.

Riedel method [55]

The Riedel at normal boiling method has the least absolute average deviation percent compared with experimental data. The Tr_b in equation 4.44 stands for the reduced boiling point temperature and the p_c is in bar. The reduced temperature equals $T_r = \frac{T}{T_c}$.

$$L_{V_b} = 1.093 \cdot R_g T_c Tr_b \left(\frac{\ln p_c - 1.013}{0.93 - Tr_b} \right) \quad (4.44)$$

Giacalone method [99]

$$L_{V_b} = R_g T_c \left(Tr_b \frac{\ln(p_c/1.01325)}{1 - Tr_b} \right) \quad (4.45)$$

Chen method [99]

$$L_{V_b} = R_g T_c Tr_b \frac{3.978 Tr_b - 3.958 + 1.555 \ln(p_c)}{1.07 - Tr_b} \quad (4.46)$$

Joback method [99]

The Joback method, on the other side is a group contribution method. To estimate the L_{V_b} , see table B.2 for the contributing groups and table B.3 for the equation.

The relations below are for the variations in latent heat with temperature.

Watson method

The latent heat of vaporization L_V can be determined by the Watson relation [55], see equation 4.47, in which the boiling point is chosen as reference point.

$$L_V = L_{V_b} \left(\frac{1 - Tr}{1 - Tr_b} \right)^q \quad (4.47)$$

The q in equation 4.47 is a constant equal to 0.38.

Fishtine [98] pointed out that q is dependent on the Tr_b of the compound, as in equation 4.48.

$$q = \begin{cases} 0.740 Tr_b - 0.116 & (0.57 < Tr_b < 0.71) \\ 0.30 & (Tr_b < 0.57) \\ 0.41 & (Tr_b > 0.71) \end{cases} \quad (4.48)$$

Viswanath and Kuloor [98] suggested that q can be expressed as in equation 4.49.

$$q = (0.00264 \frac{L_{V_b}}{R_g T_b} + 0.8794)^{10} \quad (4.49)$$

Fish and Lielmezs method

The Fish and Lielmezs method [98] is a model in which the value of the enthalpy of vaporization at the normal boiling point is assigned as the reference state, see equation 4.50.

$$L_V = L_{V_b} \cdot \frac{T_r(X + X^q)}{T_{rb}(1 + X^p)} \quad (4.50)$$

where the X is defined as in equation 4.51.

$$X = \frac{T_{rb}}{T_r} \frac{1 - T_r}{1 - T_{rb}} \quad (4.51)$$

For organic compounds, q and p are 0.35298 and 0.13856, respectively.

Pitzer's approximation

The Three-Parameter Corresponding-States Principle are also often used. The Pitzer's approximation is as in equation 4.52.

$$\frac{L_V}{R_g T_c} = 7.08(1 - T_r)^{0.354} + 10.95\omega(1 - T_r)^{0.456} \quad (4.52)$$

The acentric factor, ω in equation 4.52, is defined as in equation 4.53.

$$\omega = -1.000 - \log_{10} \frac{p^{sat}}{p_c} \quad (4.53)$$

where p^{sat} is the vapor pressure at temperature T where $T/T_c = 0.7$. However, for a close correlation, the Pitzer's approximation should be used for high temperature predictions where $0.6 < T_r < 1.0$ as claimed in ref. [99]. The T_r range for the selected components from the initial droplet temperature of 300 k varies between 0.3984 to 0.5102 and thus this method is not used for further calculations.

Vapor pressure*Clausius-Clapeyron equation*

The Clausius-Clapeyron equation assumes ideal gas behavior of the vapor and neglects the liquid volume. It can be used to determine the pure component vapor pressure, p_v , as in equation 4.54.

$$\frac{p_v}{p_\infty} = \exp \left[\frac{L_{V_b} M}{R_g} \left(\frac{1}{T_{b,i}} - \frac{1}{T_d} \right) \right] \quad (4.54)$$

In equation 4.54, R_g is the gas constant ($R_g = 8314 \text{ J/kmol} \cdot \text{K}$). Antoine believed that Clausius-Clapeyron equation cannot be accurately applied over the larger range of temperature (specifically for $T_r > 0.75$ and for the fluids with low boiling point). At boiling point the $p_v = p_\infty$. The error-producing assumptions made in the derivation of the equation are: (1) The latent heat of vaporization of any substance is constant; (2) the volume of the liquid is negligible in comparison with that of the vapor obtained therefrom; and (3) the ideal gas law holds. However, often the Clausius-Clapeyron equation is used in heating and evaporation modeling under equilibrium conditions.

Pitzer expansion in Lee-Kesler form

The Lee-Kesler method [99] is one of the very successful methods to predict the vapor

pressure. It requires the knowledge of critical pressure, critical temperature and acentric factor of the fluid as inputs, see equations 4.55 to 4.57. The $f^{(0)}$ and $f^{(1)}$ are the Pitzer's functions which are functions of T_r .

$$\ln(p_{vr}) = f^{(0)}(T_r) + \omega f^{(1)}(T_r) \quad (4.55)$$

$$f^{(0)} = 5.92714 - \frac{6.09648}{T_r} - 1.28862 \ln(T_r) + 0.169347 T_r^6 \quad (4.56)$$

$$f^{(1)} = 15.2518 - \frac{15.6875}{T_r} - 13.4721 \ln(T_r) + 0.43577 T_r^6 \quad (4.57)$$

where p_{vr} is the reduced vapor pressure = p_V/p_c , and the ω is the acentric factor (represents the acentricity or nonsphericity of a molecule) which can be found in [55] or computed using equation 4.58. Actually some large values (e.g., for alcohols) are more closely related to polarity than acentricity. However, for higher molecular weight molecules, ω increases. It also rises with polarity. At boiling point the $p_V = p_\infty$.

$$\omega = \frac{\alpha}{\beta} \quad (4.58)$$

where α and β are calculated as in equations 4.59 and 4.60.

$$\alpha = -\ln(p_c) - 5.97214 + 6.09648 \left(\frac{T_b}{T_c}\right)^{-1} + 1.28862 \ln\left(\frac{T_b}{T_c}\right) - 0.169347 \left(\frac{T_b}{T_c}\right)^6 \quad (4.59)$$

$$\beta = 15.2518 - 15 : 6875 \left(\frac{T_b}{T_c}\right)^{-1} - 13.4721 \ln\left(\frac{T_b}{T_c}\right) + 0.43577 \left(\frac{T_b}{T_c}\right)^6 \quad (4.60)$$

Vapor phase density

Ideal gas law

The density from the vapour phase of species i is computed using the ideal gas law, equation 4.61 in which the $R'_g = 0.082057 \cdot \frac{m^3 \cdot atm}{kmol \cdot K}$ while the density of the vapor mixture is by applying mixing rules (table B.1).

$$\rho_{V,S_i} = \frac{p_\infty M_i}{R'_g T_{ref}} \quad (4.61)$$

Liquid phase density

Grain method

The Grain method [94] is a method to estimate from normal boiling point data using equation 4.62. Here $V_{b,i}$ is the molar volume at the boiling point in $cm^3(gmol)^{-1}$ and n is 0.25 for alcohols and 0.31 for other organic compounds. The V_b is determined using the Schroeder's method [94], as in equation 4.63 of which data is obtained from table B.11. Here n_k and n_k^{extra} count the number of their occurrences per molecule and the V_b and V_b^{extra} are the corresponding contributions. The final mixture density ρ_L is obtained by applying the mixing rule from table B.1.

$$\rho_L = M_i (V_b)^{-1} \left(3 - 2 \frac{T_d}{T_b} \right)^n \quad (4.62)$$

$$V_b = \sum n_k(V_b) + \sum n_k^{extra} V_b^{extra} \quad (4.63)$$

Liquid phase specific heat

Chueh and Swanson method

$C_{p,L}$ is the specific heat of the liquid mixture and is calculated from the Chueh and Swanson method as explained in Appendix B.3. This method is a group contribution method in which firstly the specific heat of each contributing group of each species C_{p_k} is identified and then the final species $C_{p,i}$ is determined by $C_{p,i} = (\sum_k N_k \cdot C_{p_k})/M_i$. The N_k stands for the number of group appearing in the species i . The $C_{p,i}$ is thus constant, but the $C_{p,L}$ will change with temperature since it is dependent on the component mass fractions. A constant specific heat is obtained, not dependent on the temperature, and is valid for temperatures below 80 % of the critical temperature and this study does not focus on near-critical phenomena. The m_d stands for the droplet mass.

Vapor phase specific heat

Joback method

The specific heat for the vapor phase C_{pV} is calculated from table B.2 and B.3.

4.4.2 Transport properties

Gas phase diffusivity

Fairbanks and Wilke expression

The Fairbanks and Wilke [88] expression is used for the diffusion coefficients of species i into the vapor-gas mixture, D_i , see equation 4.64.

$$D_i = \frac{1 - \chi_{S,i}}{\sum_{\substack{j=1 \\ i \neq j}}^n \frac{\chi_{S,j}}{D_{i,j}}}; \quad (4.64)$$

Chapman-Enskog theory

Before calculating the D_i in equation 4.64, the binary diffusion coefficient for all the species pairs must be determined. The Chapman-Enskog theory can be used for determining the binary diffusion coefficients, see equation 4.65.

$$D_{i,j} = D_{j,i} = 1.8583 \cdot 10^{-7} \frac{T_{ref}^{3/2} (M_i^{-1/2} + M_j^{-1/2})}{p_\infty \sigma_{i,j}^2 \Omega_D} \quad (4.65)$$

where the Ω_D represents the collision integral for the two molecules for mass diffusivity (dimensionless) from [93] and is calculated as in Appendix . The $\sigma_{i,j}$ stands for the molecular collision diameter, which is determined by $\sigma_{i,j} = \frac{\sigma_i + \sigma_j}{2}$ [93]. However, not all $\sigma_{i,j}$ and Ω_D data is found for the molecules used in this study. Therefore the method below is applied.

Fuller-Schettler-Giddings correlation

The Fuller-Schettler-Giddings correlation [90], equation 4.66, is used since it includes data for, in this case, all organic molecules as well. The v_i is the diffusion volume for the atomic component as given in table B.10.

$$D_{ij} = D_{ji} = \frac{0.001 \cdot T_{ref}^{1.75} \left(\frac{1}{M_i} + \frac{1}{M_j} \right)^{-1/2}}{p_\infty \left[\sum_k v_i^{1/3} + \sum_k v_j^{1/3} \right]^2} \quad (4.66)$$

Gas phase thermal conductivity

Roy and Thodos method

The Roy and Thodos technique is used to calculate the species thermal conductivity k_i , while the mixing rule included in table B.1 is used to calculate the gas mixture thermal conductivity k_m . The Roy and Thodos method is also a group contribution method, which is explained in Appendix B.5. Determination of the k_m requires calculating the vapor phase viscosity. The Roy-Thodos correlation requires only the critical temperature and pressure. Reid et al. [55] recommends this method for polar compounds against other methods to estimate the gas phase thermal conductivity (i.e. the Eucken equation, the modified Eucken and the Chung, et al. modification, see Chapter 10.3 of [55]).

Gas phase viscosity

Reichenberg method

The vapor phase viscosity is obtained by the Reichenberg method, which is a group contribution method for among others organic vapors. This procedure is included in section B.4 in the appendices.

Dimer properties: solid phase

Relevant properties of the dimer are summarized in table A.2 and are assumed to be constant through out the evaporation process.

4.5 Development and implementation of evaporation model

First the evaporation model excluding polymerization reaction is developed and next after the evaporation model including the reaction. The simultaneous change of mass and temperature of the droplet is solved using a fourth order Runge-Kutta method in MATLAB (ver. 2017b) is to compute the temporal change in diameter and temperature of the droplet. No MATLAB built-in solver (e.g. the ode45) is used, to have better control of the inner workings of the program, i.e. variable coefficients, the step size, maximum error level, time limit, etc. The model procedure is given in figure 4.4. The time step h is chosen 0.0001 s. A summary of the steps is as follows:

1. The ambient temperature and pressure are set to 800 K and 1 atm, respectively, which are typical conditions in many combustion devices (e.g., engines) [41]. The initial droplet temperature and diameter are set to 300 K and 100 μm respectively;
2. All relevant properties are firstly calculated for the pure species. Secondly, based on the initial liquid (Y_{L_i}) and mole (χ_{L_i}) mass fractions, the mixing rules as in table B.1 are applied to obtain mixture properties;
3. The Runge Kutta 4th order coefficients are determined based on the first part in equations 4.23 and 4.26;

4. The droplet temperature T_d and diameter d are then updated via the Runge Kutta scheme;
5. The new droplet mass and density are determined by equations 4.67 and 4.68 respectively. Also the new Y_{L_i} is determined by equation 4.69. Mass conservation is checked based on $\sum_i Y_{L_i} = \sum_i \varepsilon_i = 1$;
6. Based on the new T_d and Y_{L_i} , the previous steps are iterated. If the reaction temperature is reached, the second part of equations 4.23 and 4.26 is used in which the mass and heat diffusion model are corrected for regarding the polymerization reaction;
7. The droplet is evaporated when the relative temperature and mass changes are respectively $\frac{|T_d^{\Delta t+1} - T_d^{\Delta t}|}{T_d^{\Delta t+1}} < 10^4$ and $\frac{|\dot{m}_d^{\Delta t+1} - \dot{m}_d^{\Delta t}|}{\dot{m}_d^{\Delta t+1}} < 10^4$.

$$m_d^{\Delta t+1} = m_d^{\Delta t} + \dot{m}_d^{\Delta t} \cdot h \quad (4.67)$$

$$\rho_L^{\Delta t+1} = \frac{\dot{m}_d^{\Delta t} \cdot h \cdot \frac{6}{\pi} + \rho_L^{\Delta t} \cdot (d^{\Delta t})^3}{(d^{\Delta t+1})^3} \quad (4.68)$$

$$Y_{L_i}^{\Delta t+1} \rho_L^{\Delta t+1} \frac{4}{3} \pi \left(\frac{d^{\Delta t+1}}{2} \right)^3 = Y_{L_i}^{\Delta t} \rho_L^{\Delta t} \frac{4}{3} \pi \left(\frac{d^{\Delta t}}{2} \right)^3 - \dot{m}_i 4\pi \left(\frac{d^{\Delta t}}{2} \right)^2 \Delta t \quad (4.69)$$

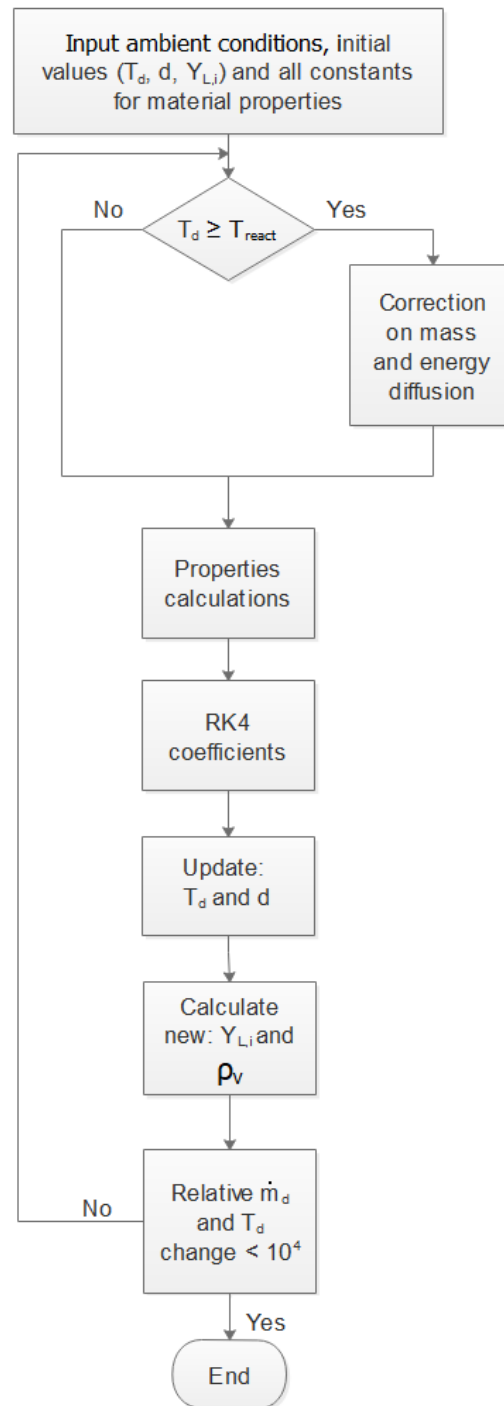


Figure 4.4: Flowchart of the droplet evaporation model.

Chapter 5

Results and Discussion

This chapter first evaluates the methods used for the estimation of the thermophysical properties. Validation is done as far as possible with experimental data, if available, or with other correlations. Secondly, the obtained results without the polymerization reaction are validated with literature data. Thirdly, the results obtained with the polymerization reaction are compared with the model without the polymerization reactions and discussed.

5.1 Thermophysical properties estimation methods

For most of the components, the calculation of important properties, i.e. heat capacity, latent heat, vapor (saturation) pressure and thermal conductivity, were carried out based on approximations. Data is needed for the range of the surface temperature of the droplet.

5.1.1 Thermodynamic properties

In this section the data and correlations on the difference of the normal boiling point, critical properties, latent heat, vapor pressure, liquid phase density, liquid phase specific heat and vapor phase specific heat are presented.

Normal boiling point

For the boiling points (at atmospheric pressure) the aforementioned methods are used for estimations and tested against data available by NIST [56] and summarized in table 5.1.

Table 5.1: Boiling point temperatures [K]

Component	Yuan method	Joback method	Database
Water			373.15 [97]
Acetic acid	447.40	391.21	391.05 [97], 391.20 [56]
Hydroxypropanone	516.98	418.97	
Phenol	553.48	460.25	455.0 [56]
Eugenol	687.44	540.06	526.41 [56]
Levogluconan	658.26	577.64	

The NIST database consists of many correlations used for determining the property based on experimental studies; in table 5.1 the value with the minimum uncertainty is included. It can be seen, that for the species of which database value were available, the Yuan method overpredicts the boiling point. Therefore, the Joback method is used

for further calculations.

Critical properties

Table 5.2 summarizes critical point data for all the components obtained by the Joback method.

Table 5.2: Critical point data estimated by the Joback method. In between the brackets are values found from databases.

Component	T_c [K]	p_c [bar]
Water ¹	647	221
Acetic acid	588 (594.75 [94])	57.3 (57.9 [94])
Hydroxypropanone	595	54.8
Phenol	702 (694.25 [91])	61.4 (59.30 [91])
Eugenol	753 (699.844 [56])	32.8 (30.54 [56])
Levogluconan	733	57.0

¹ Aspen

Latent heat

Table 5.3 summarizes the calculated latent heat at boiling point and figure 5.1 summarizes the latent heat variation with temperature. Figure 5.2 includes the latent heat of acetic acid determined by the Watson and the Fish and Lielmezs method and also experimental data from the Dortmund data bank [92].

Table 5.3: Latent heat at boiling point [kJ/kg].

Component	Riedel	Giacalone	Chen	Joback	Database
Water	2333.27	2188.28	2346.74	-	2259.36 [97]
Acetic acid	677.58	651.99	665.91	772.73	644.36 - 716.07 [56]
Hydroxypropanone	674.06	629.30	646.26	668.47	
Phenol	501.87	483.82	494.95	736.58	684.31 [56]
Eugenol	347.75	336.09	334.90	368.51	351.40 - 402.56 [56]
Levogluconan	693.82	564.82	575.55	541.69	

A comparison of the values from the different methods shows that the Riedel method values are closest to the Database values, and therefore this method is chosen for further calculations.

Figure 5.1 includes predicated latent heat values versus temperature obtained by both the Fish and Lielmezs and the Watson method. It can be seen that both methods have a similar prediction of latent heat for almost all of the components. Experimental data were found only for acetic acid is found (from the Dortmund Databank [92]), see figure 5.2, which shows that the predicted latent heat values by the two methods do not agree well with the data. Since the scarce experimental data of the variation of latent heat vs. temperature for the (other) selected components, the Fish and Lielmezs methods is used for further calculations.

It can be seen that the latent heat of water is much higher than other components, while other components have close values of latent heat. It means that high amount of water can significantly impact the vaporization rate. The similar latent heat of other components indicates that these components may have similar behaviors in heat absorption. Therefore, it is expected that the high water content will strongly affect the vaporization behavior of the droplet.

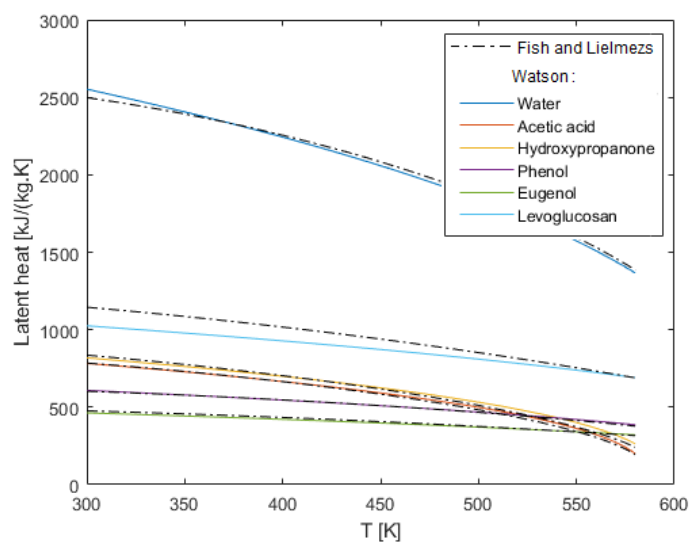


Figure 5.1: Latent heat variation with temperature of the pure components.

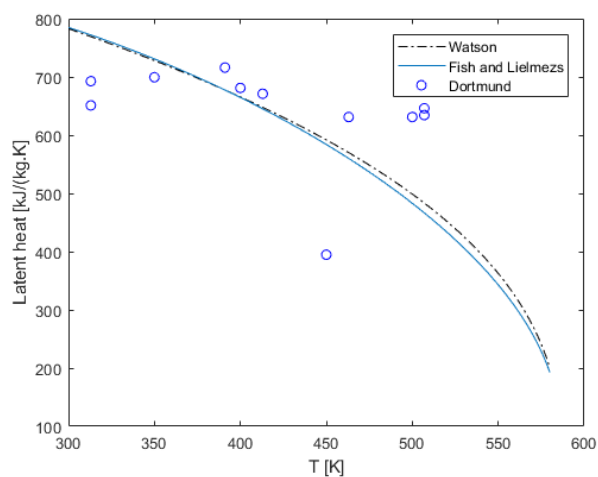


Figure 5.2: Latent heat variation with temperature of pure acetic acid.

Vapor pressure

Figure 5.3 presents the variation of vapor pressure of the pure components with temperature of both the Pitzer expansion in Lee Kesler form and the Clausius Clapeyron equation.

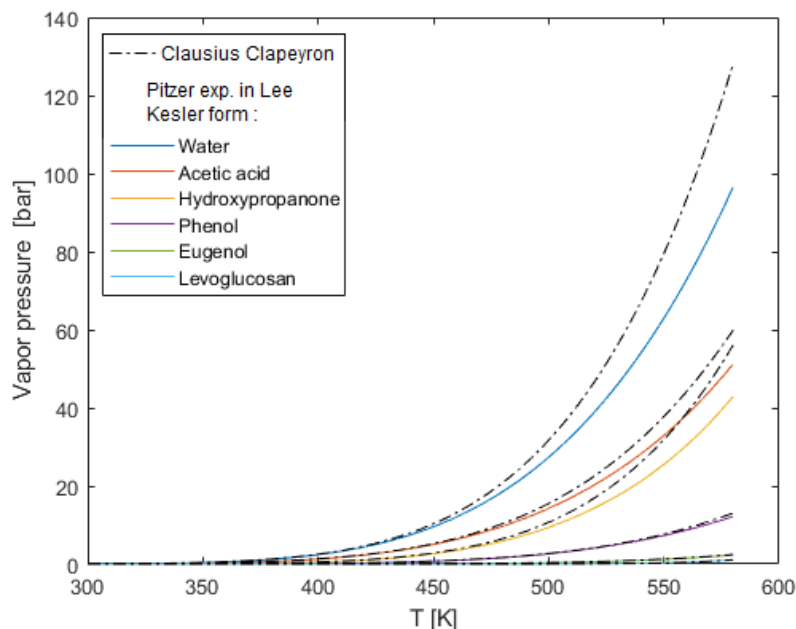


Figure 5.3: Vapor pressure of the pure components variation with temperature.

Figure 5.4, 5.5 and figure 5.6 include the vapor pressure for water, acetic acid and levoglucosan respectively. Each plot also includes experimental data (experimental data is only found in literature for these components in the specified temperature range) from Dortmund Databank [92]. For water, it can be seen that at lower temperatures, the experimental data follows the Clausius-Clapeyron equation, and from about 350 K it follows the Lee-Kesler method. The same trend is seen for levoglucosan where experimental data from Oja and Suuberg [102] follows the Lee-Kesler method from about 400 K. For acetic acid, only low temperature experimental data was available, and as expected it also follows the Clausius-Clapeyron equation. The aforementioned, together with the comment of Antoine on the Clausius-Clapeyron equation about its inaccuracy on the larger range of temperature (specifically for $T_r > 0.75$ and for the fluids with low boiling point [99]) and the evaporation temperature range for this study, results in the application of the Lee-Kesler method for further calculations.

It can be seen that water has the highest vapor pressure and levoglucosan has the lowest vapor pressure among all the components. Since it is expected that components with higher vapor pressure vaporize earlier, results in figure 5.3 will have implications in the vaporization order of the components in general. The results show that below 400 K, the vapor pressures of the components are almost zero, indicating the low volatility of these components. Higher vapor pressure means a faster vaporization rate.

Liquid phase density

Figure 5.7 includes the variations of the liquid density of the pure components obtained by the Grain method. Except for water, which is determined by Aspen Hysis [97] for a limited temperature range. Figure 5.8 includes predicted data and experimental data of ref. [94] for pure acetic acid and a relatively good agreement is found. The droplet

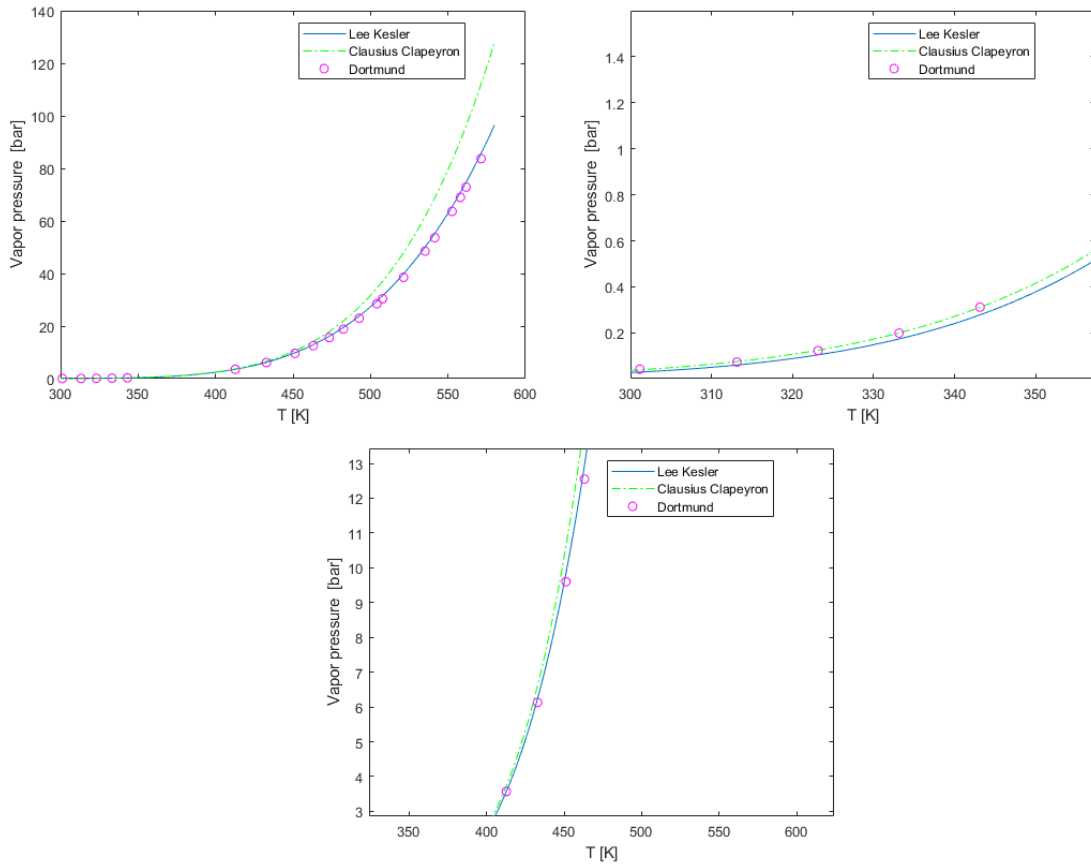


Figure 5.4: Vapor pressure of pure water variation with temperature.

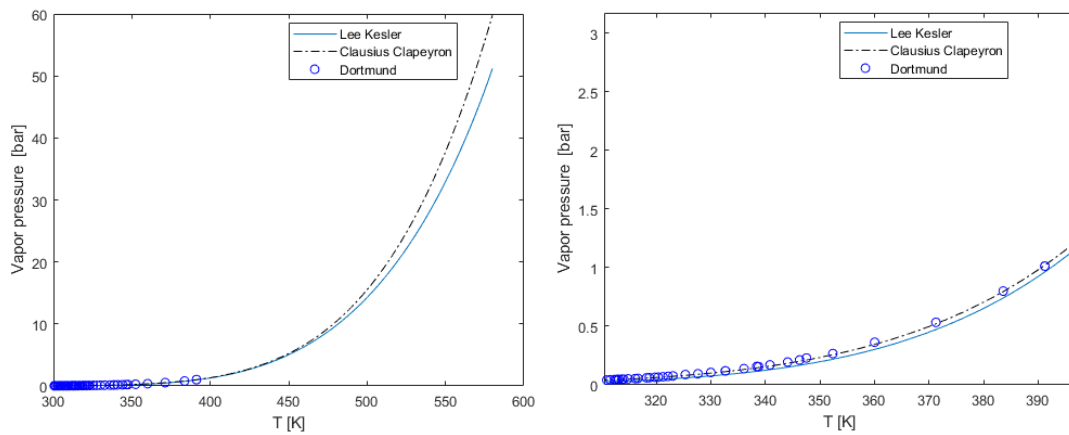


Figure 5.5: Vapor pressure of pure acetic acid variation with temperature.

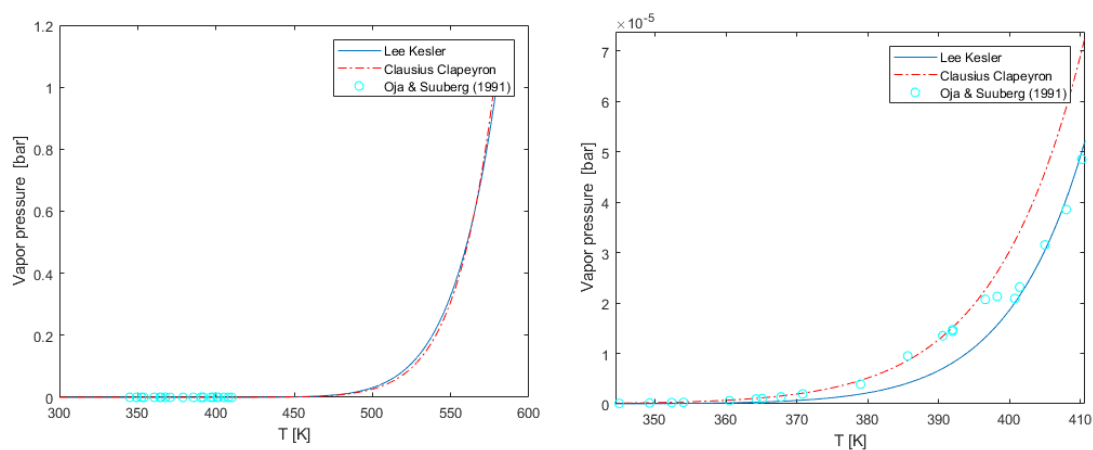


Figure 5.6: Vapor pressure of pure levoglucosan variation with temperature.

density is thus also expected to decrease with increasing temperatures.

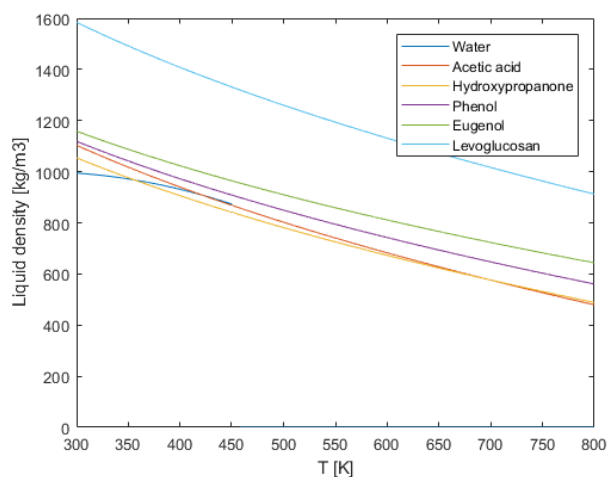


Figure 5.7: Liquid density variations with temperature of pure components.

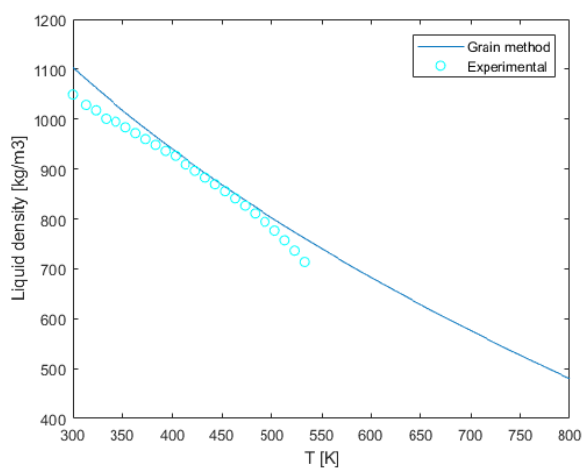


Figure 5.8: Liquid density variations with temperature of pure acetic acid.

Liquid phase specific heat

Table 5.4 summarizes the obtained liquid phase specific heats. Also is included experimental data for components found from the Nist Webbook [91]. A good agreement is shown for the components of which experimental data is available.

Table 5.4: Liquid phase specific heat [kJ/kgK].

Component	Chueh and Swanson	Database
Water	4.186	4.186 [91]
Acetic acid	1.945	2.043 [91]
Hydroxypropanone	2.202	
Phenol	1.584	1.437 [91]
Eugenol	1.918	2.090 [91]
Levogluosan	2.310	

Vapor phase specific heat

The dependence of specific heat for vapor phase is (not as the case for liquid phase) strongly dependent on the temperature. Figure 5.9 represents the vapor phase specific heats of all the pure components, except for water, obtained by the Joback method. The specific heat for water is calculated using Apsen Hysis [97]. The gas phase specific heat is used for the G factor in the heat diffusion model (section 4.3.3-equation 4.29 and section 4.3.4-equation 4.38).

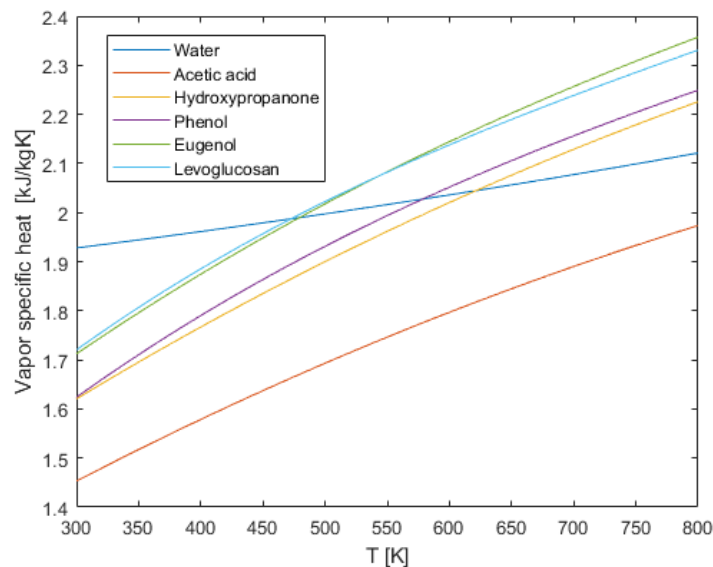


Figure 5.9: Vapor phase specific heat of pure components.

Figure 5.10 represents the specific heat of pure acetic acid including experimental data from NIST [91], the coefficients from Reid et al. [55] and the method of Constantinou and Gani. A relatively good agreement is found especially between the Joback method and the Constantinou and Gani method. A comment on the NIST data placed is that the uncertainty of 0.052 to 0.089 kJ/kgK . That figure also includes data obtained by the Joback method and the use of coefficients of Reid et al. for pure phenol, here also a relatively good agreement is found. An insignificant difference is also observed for the other 5 components. The NIST data also shows a relatively good agreement with the predicted values for acetic acid, while for the other 5 components no experimental data was available. Decided is to work further with the Joback method.

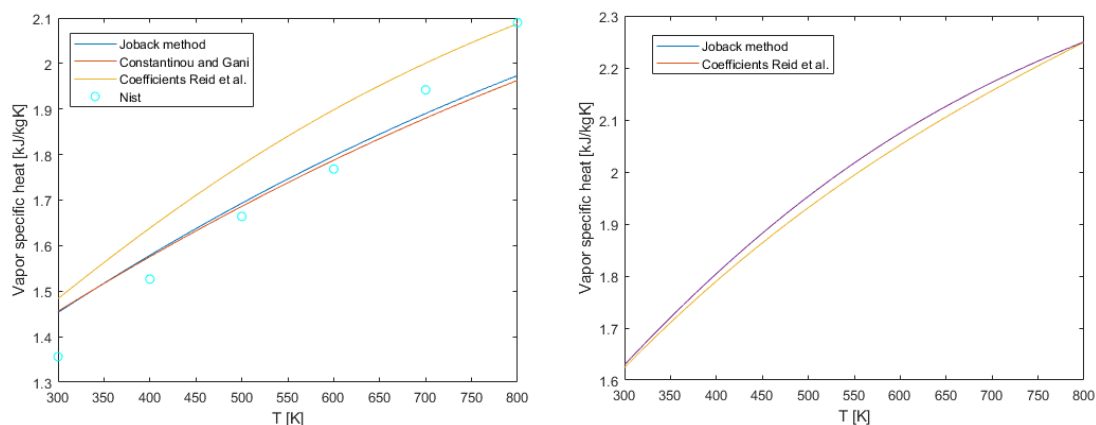


Figure 5.10: Left: Vapor phase specific heat of pure acetic acid. Right: Vapor phase specific heat of pure phenol.

5.1.2 Transport properties

In this section the data and correlations on the difference of the vapor phase viscosity, vapor phase thermal conductivity and the gas phase diffusivity are presented.

Vapor phase viscosity

Figure 5.11 represents the vapor phase viscosity of all the pure components, except for water, obtained by the Joback method. Figure 5.12 includes data obtained from the Joback method and experimental data from [94]. No experimental data for the other components were found.

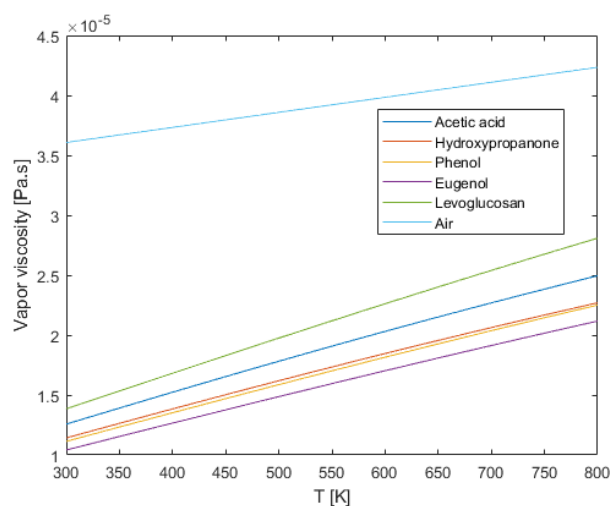


Figure 5.11: Vapor phase viscosity of pure components.

Vapor phase thermal conductivity

Figure 5.13 includes the vapor phase thermal conductivity of all the pure components which are calculated by the Roy and Thodos method, except for water and air. The latter is calculated by Aspen Hysis [97]. It can be seen that at higher temperatures, the larger components have a significantly higher thermal conductivity. Figure 5.14 includes data predicted by the Roy and Thodos method and some experimental data from [92].

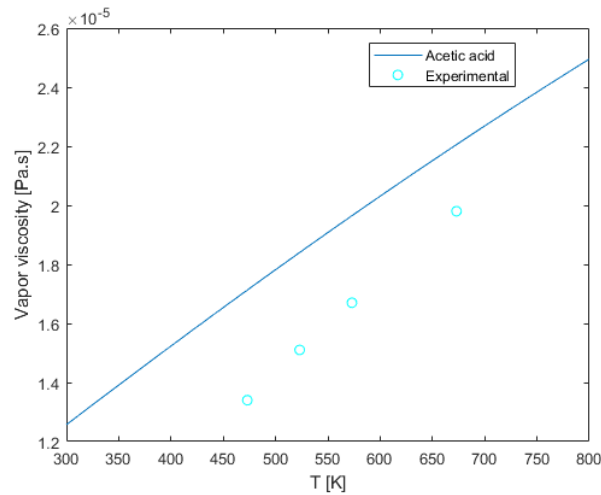


Figure 5.12: Vapor phase viscosity of pure acetic acid.

No experimental data of the other components were found.

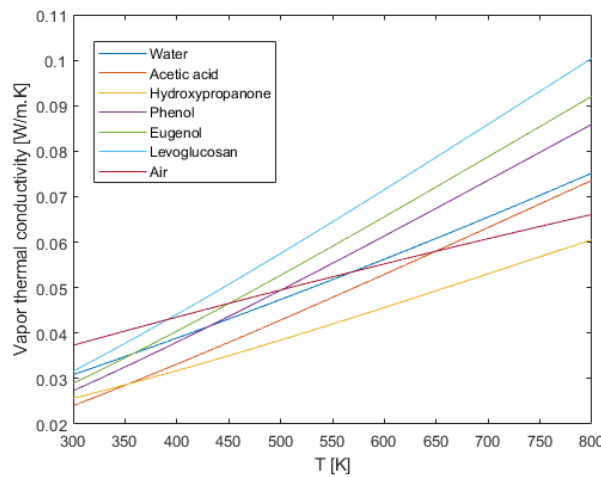


Figure 5.13: Vapor phase thermal conductivity of pure components.

Gas phase species diffusivity

The diffusion coefficient of species i in the vapor-gas mixture (D_i) is based on temperature dependent surface vapor mole fraction of species i and its binary diffusion coefficients ($D_{ij}=D_{ji}$) of species i into each of the other vapor and gas phase species j . As mentioned earlier, the D_i differs for each of the species and is not considered to be constant. Figures 5.15, 5.16 and 5.17 includes the obtained D_i values by the Fuller and Giddings correlation. For some species, also other database values are indicated for comparison. Figure 5.15 contains experimental data from [90].

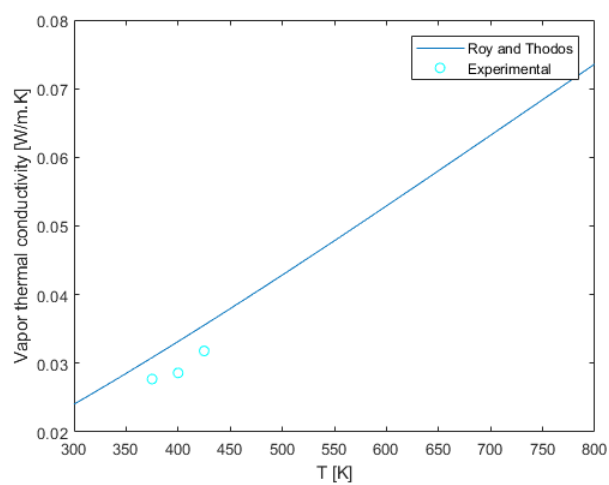


Figure 5.14: Vapor phase thermal conductivity of pure acetic acid.

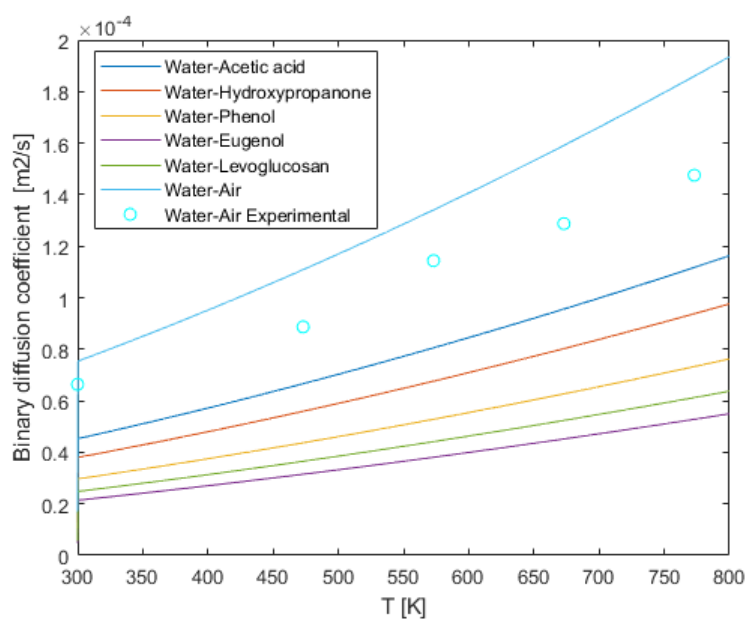


Figure 5.15: Binary diffusion coefficient of water vapor into the other species in the vapor-gas mixture.

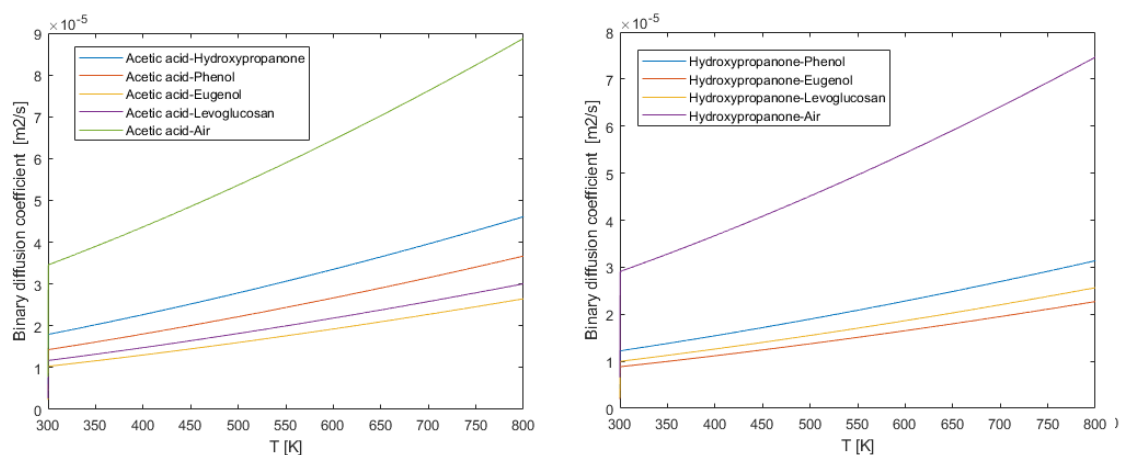


Figure 5.16: Left: Binary diffusion coefficient of acetic acid vapor into the other species in the vapor-gas mixture. Right: Binary coefficient of hydroxypropanone vapor into the other species in the vapor-gas mixture.

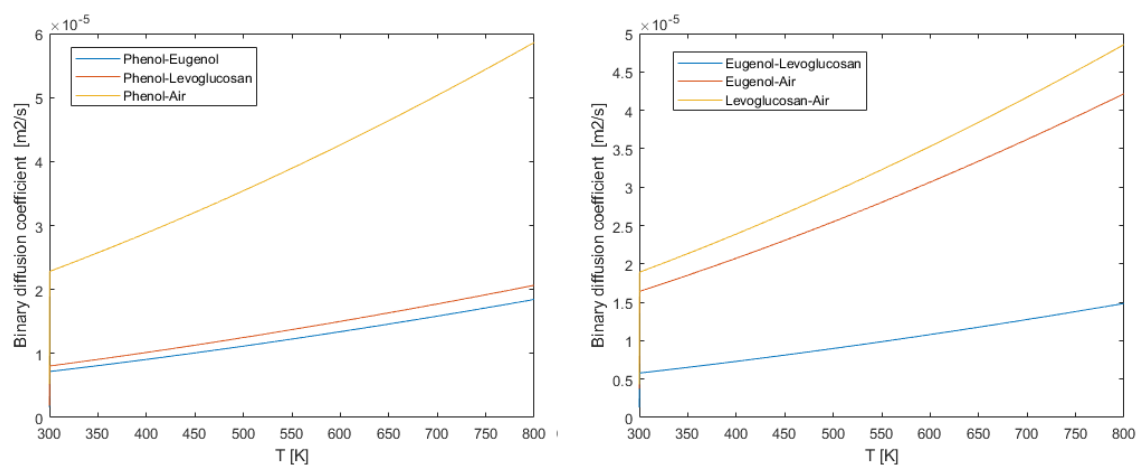


Figure 5.17: Left: Binary diffusion coefficient of phenol vapor into the other species in the vapor-gas mixture. Right: Binary coefficient of eugenol and levoglucosan vapor into the other species in the vapor-gas mixture.

5.2 Evaporation in absence of polymerization reaction

This section firstly presents the results of the evaporation model in the absence of polymerization reaction. Secondly, these results are validated, as far as possible, with literature data.

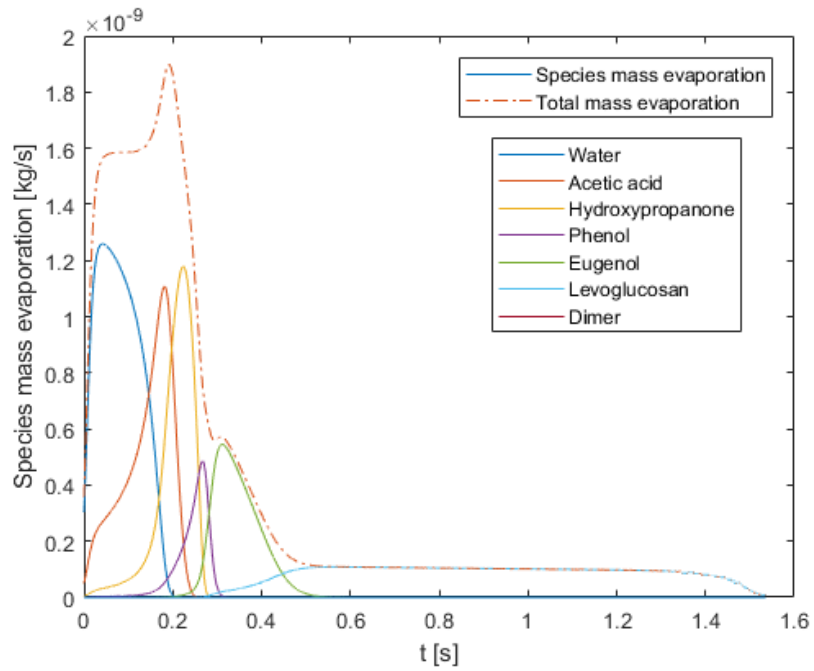
5.2.1 Stagnant droplet in still air

The initial diameter for the droplet equals $d_0 = 100 \mu m$, the initial temperature $T_{d0} = 300 K$ and the initial composition is as in table 2.3. Conditions at infinity are set as $p_\infty = 1 atm$ and $T_\infty = 800 K$.

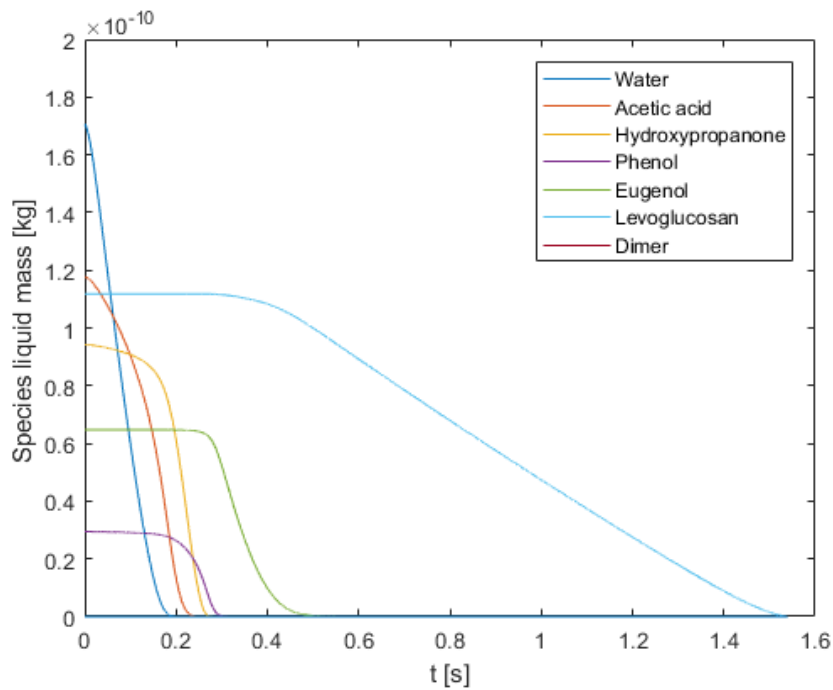
Figure 5.18 represents both the mass evaporation rates and the change in liquid mass for each component. Figure 5.19 represents the liquid species mass fractions with time. As can be seen, water is the first component to vaporize due to its relatively high vapor pressure. As the water content decreases, other components experience an increase in their mass fractions in the drop. After disappearance of water, the next most volatile component (acetic acid) starts to evaporate more rapidly. The same trend holds successively for the rest of the components. The rapid reduction in mass fraction in the liquid phase is observed after a lighter component has disappeared from the droplet and they reach temperatures closer to their boiling points. As expected, levoglucosan is the last component to evaporate from the droplet due to its relatively low vapor pressure and high boiling point. Furthermore it can be observed that the decrease in mass occurs faster for the more volatile components, while for the heaviest component, levoglucosan, the slowest rate is observed.

Figure 5.20 represents the change of droplet temperature and diameter in time. Initially the droplet starts heating without species evaporation. This period is observed to be negligible, due to the fact that water already starts to evaporate at quite small amounts. After vaporization starts, the drop temperature continues to increase. The droplet temperature plot is not smooth, as would be the case for a single component behaving in accordance with the d^2law . Figure 5.21 represents the variation of diameter squared ratio with time. For single component fuels, such a plot would be a constant line with a negative slope. Due to the multicomponent composition, the obtained plot has different slopes. Each slope in this plot defines the component which dominates the evaporation behaviour in a certain time range. Like a single component droplet, the droplet lifetime reaches the end before the boiling temperature of the heaviest component is reached; that component will heat till it reaches its saturation (wet bulb) temperature and then evaporate further. Simultaneously, the drop size decreases due to the drop components' migration from liquid phase to gas phase. From both figure 5.18 and 5.20 it can be seen that levoglucosan dominates the evaporation process for about 2/3 of the droplet lifetime.

The evaporation rate decreases with time, as the heavier compounds evaporate. Figure 5.21 shows three main regions. The first region is the increasing evaporation rate with time (till about 0.3 s) where the light volatiles, such as water, acetic acid, hydroxypropanone and phenol, dominate the evaporation process. After these components have fully evaporated, figure 5.21 shows a lower evaporation rate (around 0.3-0.5 s); in this time range, phenol dominates the evaporation process. After this, an even a lower evaporation rate is observed, here levoglucosan dominates the evaporation process.



(a) Species and total evaporation mass rates.



(b) Species liquid mass inside droplet.

Figure 5.18: Species mass fractions variations with time.

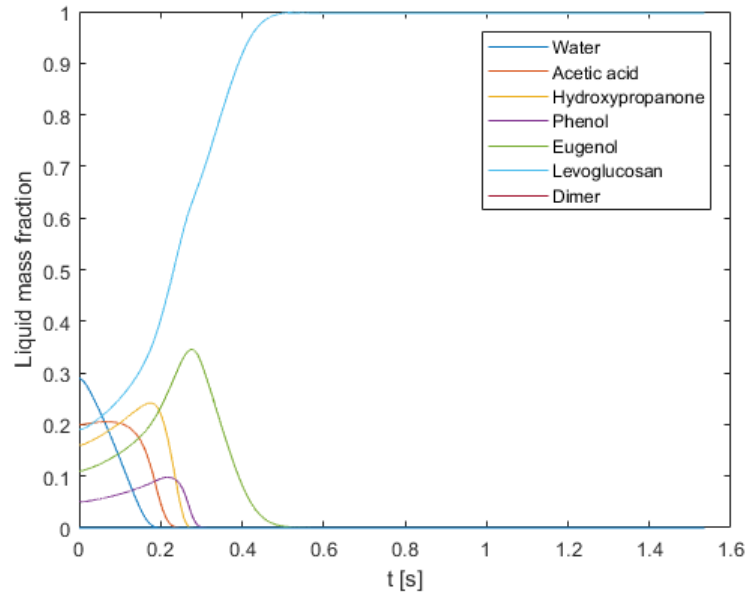
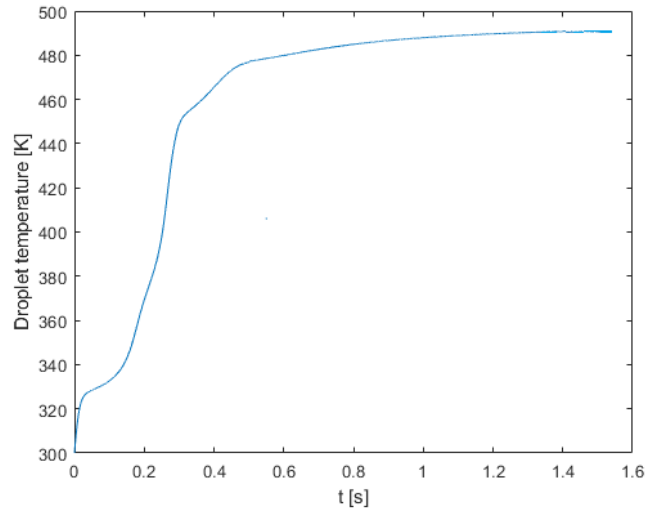
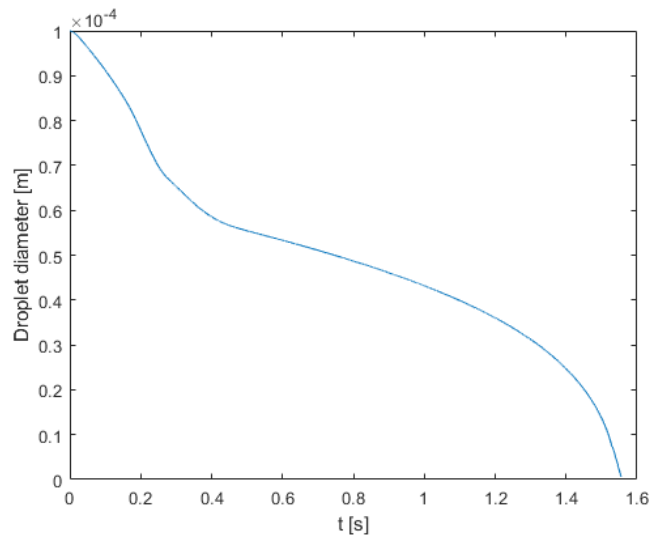


Figure 5.19: Variation of liquid mass fractions with time.

Figure 5.22 represents the variation of contributions to the heat flow rate over time. The sensible heat ($10^{-10} \leq Q_S [kJ/s] \leq 10^{-14}$) of the droplet is shown as a flat line while the convective ($10^{-6} \leq Q_C [kJ/s] \leq 10^{-8}$) and latent heat ($-10^{-6} \leq Q_L [kJ/s] \leq -10^{-8}$) term account basically for the heat balance during evaporation. These contributing terms are included in figure 4.3 and equation 4.26.



(a) Variation of droplet temperature with time.



(b) Variation of droplet diameter with time.

Figure 5.20: Variation of droplet temperature with time.

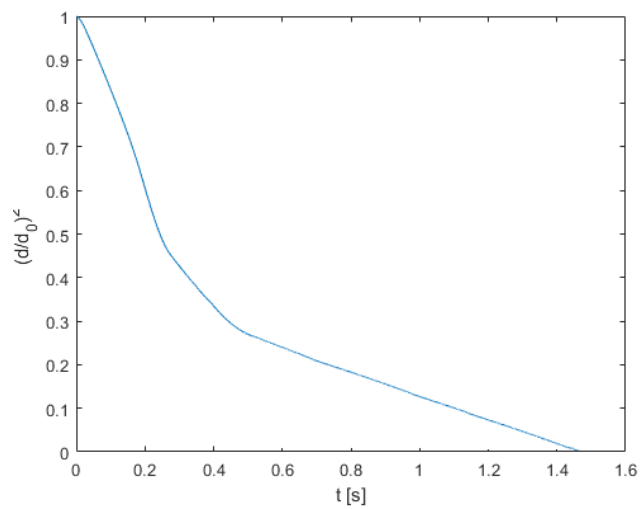


Figure 5.21: Variation of diameter squared ratio with time.

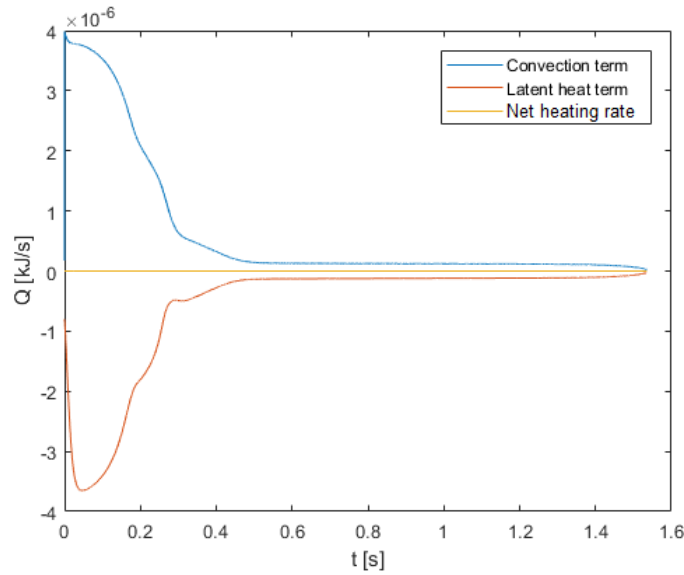


Figure 5.22: Variation of heat transfer rate at the droplet surface with time.

5.2.2 Validation against literature experimental data

Since the effect of internal bubbling (neglected in the current model) has an impact on the droplet diameter with time history, this term is explained graphically with experimental data. Arash et. al. [87] included experimental data of a 50% binary heptane and hexadecane droplet and observed internal bubbling during the evaporation process, see figure 5.23. The more volatile component, heptane, still exists in the droplet while the droplet temperature exceeds the boiling point of heptane. Under this condition, the saturated or superheated vapor of heptane appears in the form of bubbles which can move outward. This unusual phenomenon is reported as internal boiling, superheating, or bubbling [87].

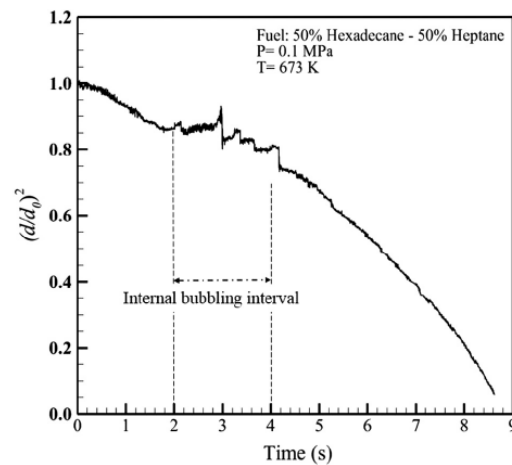


Figure 5.23: Definition of the internal bubbling interval during the vaporization process of a binary-component 50–50% volume percentage heptane-hexadecane droplets, $d_0 = 1.1 \text{ mm}$, $T_\infty = 673 \text{ K}$, $T_{d_0} = 300 \text{ K}$, $p_{1\infty} = 1 \text{ atm}$ [87].

Very few detailed experimental data on pyrolysis oil evaporation are found in literature. Two cases are considered, one with real pyrolysis oil [17] and one with a binary (hydrocarbon) system [106].

In an investigation of the combustion behavior of biomass-derived liquids, Wornat et. al. [27] have performed single droplet experiments with two biomass oils (produced from the pyrolysis of oak and pine) in a laminar flow reactor. They released the droplets downward and used a stoichiometric $H_2 - CH_s - O_2 - N_2$ mixture to generate the reactor flame. The characteristic of their oil are found to be similar to the surrogate oil from this study. The experiments are conducted at 1600 K on 320 μm diameter droplets. The temperature is twice as high as the temperature used for evaporation in this study, also the droplet diameter is more than three times bigger than in this study. Evaporation at higher temperatures is expected to occur faster, while evaporation for larger droplets is expected to occur slower due to the larger droplet mass and area. Furthermore, in the case of Wornat et. al., the droplet has a slip velocity. The Re , equation 4.21, will thus not equal zero. A consequence is thus that the Sh_{i0} , equation 4.20, will now be higher than two, resulting in a higher species evaporation rate (equation 4.16) and a faster droplet decrease in time (equation 4.23).

Figure 5.24 includes the droplet squared diameter with time obtained by Wornat et. al. [27]. It can be seen that there is no linear relationship between the squared droplet diameter and time (as would be the case for a single component fuel). It can be concluded that the real pyrolysis oil, containing a wide range of components, has a qualitatively different trend than the surrogate oil of this study. The real pyrolysis oil shows an (constant) increasing evaporation rate with time, while the surrogate oil shows different evaporation rates which are decreasing in time.

An explanation of the aforementioned can be given as summarized below.

- The twice as high temperature used in their experiments increases the evaporation rate. When the fuel is injected at a higher temperature than the saturation temperature corresponding to the ambient pressure, the fuel is under superheated conditions and vaporization occurs first through the boiling process, and then changes to normal evaporation later in the droplet lifetime. For the vaporization of multi-component fuels, the droplets are more frequently in the boiling situation due to the high volatility of the light-end components of the fuel. For realistic predictions of the vaporization of multi-component fuels under typical engine operating conditions, both boiling and normal evaporation modes must be considered and the prediction of a smooth transition between those two modes is desirable;
- The droplets have a slip velocity, which also increases the evaporation rate;
- In the real evaporation process differs from the evaporation process as modeled in this study.

The real evaporation process does not occur (partially) preferentially, i.e. that lighter components start evaporating first and later on the heavier components start to evaporate. The light and heavy components evaporate simultaneously due to the following. Light components can still be trapped inside the droplet at the early evaporation process and if the evaporation proceeds, then these light components are evaporated, thereby increasing the evaporation rate even at a later time in the process. The same holds for the heavy components. They can evaporate simultaneously with the (very) light components at the beginning of the process, because they were already available on the droplet surface. This results in a decreasing evaporation rate in the early evaporation process;

- A consequence of the aforementioned is internal bubbling, as in figure 5.23, which

can decrease the evaporation rate during the bubbling interval;

- The surrogate oil does not fully represent the real BPO composition. Adding more components (for each time zone as in table 2.2) would qualitatively produce a different droplet diameter squared over time trend;

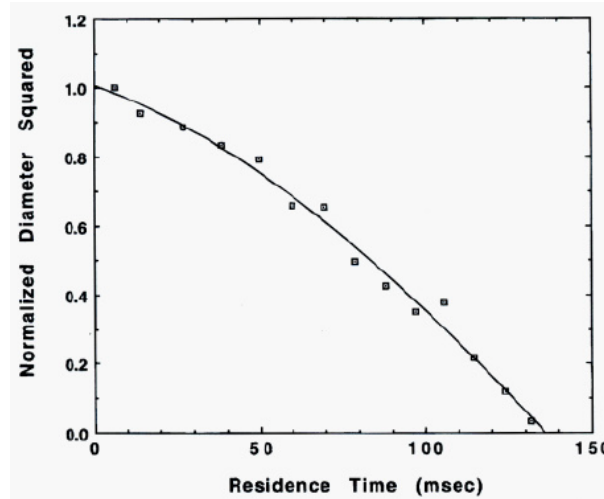


Figure 5.24: Normalized droplet diameter squared as a function of residence time in the reactor [27]. The points are experimental data points, while the solid line is the best fit.

Torres et. al. [106] studied, amongst other, the variations of normalized squared droplet radius with the time for a heptane-decane droplet. The experimental data they used are experiments based on single droplet suspended by a 0.2 mm diameter quartz fibre. Figure 5.25 includes experimental data for the binary system. Two data sets are included in the figure have the following conditions. Data 6: $d_0 = 1.334 \text{ mm}$, $T_{d_0} = 294 \text{ K}$, $T_\infty = 348 \text{ K}$ and the gas velocity to which the droplet is subjected is $U_\infty = 3.10 \text{ m/s}$. Data 7: $d_0 = 1.042 \text{ mm}$, $T_{d_0} = 292 \text{ K}$, $T_\infty = 341 \text{ K}$ and $U_\infty = 3.36 \text{ m/s}$. The effects taken into account by the the model they used to predict the values as in figure 5.25, are listed in table 5.5.

Table 5.5: Main differences between assumptions/ effects of the model of Torres et. al. [106] and the model of the current study.

Assumption Effect	Torres model	Current study model
Moving droplet in flowing gas	Yes	Stagnant droplet in still air
Liquid enthalpy diffusion	Considered	Not considered
Internal circulation	Considered	Not considered
Temperature gradient liquid phase	Yes (discretized using 10 points)	No
Concentration gradient liquid phase	Yes (discretized using 10 points)	No

Temporal and spatial variations in liquid droplet composition and temperature were not modelled but solved (using a conservative finite volume scheme) for by discretizing the interior of the droplet. The 10 points in the interior of the fuel droplet are distributed so that more points lie near the surface of the droplet [106]. Torres et. al. found that the interior discretization is necessary to correctly compute the evolution of the droplet composition and have relatively good agreements with experimental data.

The experimental and the predicted data in figure 5.25 also show a higher evaporation rate at the beginning of the evaporation process and a lower evaporation late at the end

of the process. The same trend as is obtained for this study. The droplet temperature profile does not increase constant towards the highest droplet temperature, the same trend which is also observed for this study. The time needed for evaporation in the case of Torres et. al. is relatively higher than for the case of this study, which is due to the larger droplet size and the much lower gas phase temperature.

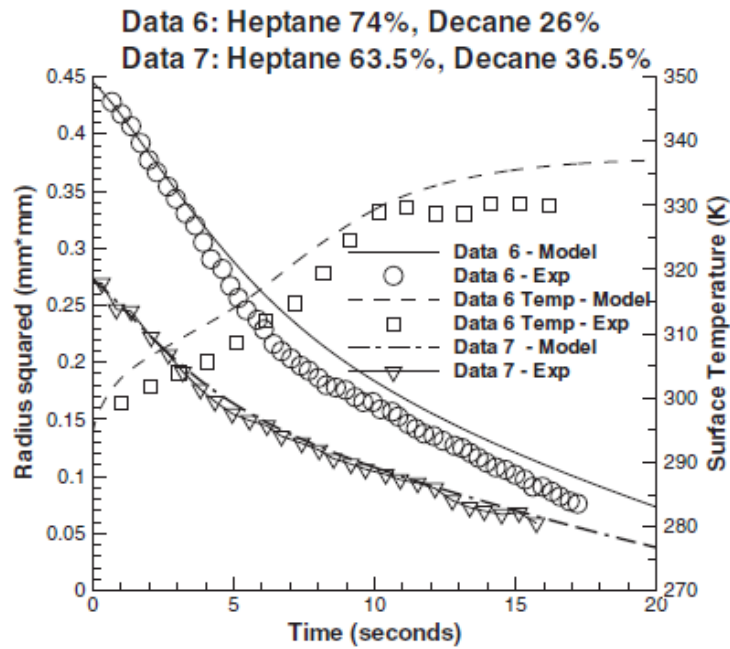


Figure 5.25: Temperature and droplet lifetime comparison between predicted and experimental data from Torres et. al. [106].

5.3 Evaporation including polymerization reaction

This section represents the results obtained by the model including polymerization reaction are presented.

5.3.1 Stagnant droplet in still air

Figure 5.26 represents the mass evaporation rates and the liquid mass fractions with time. The reaction starts at 463 K, when phenol is in its last stages of evaporation and levoglucosan in its first stages. Levoglucosan has an earlier disappearance (at 1.148 s) than in absence with polymerization reaction (1.153 s).

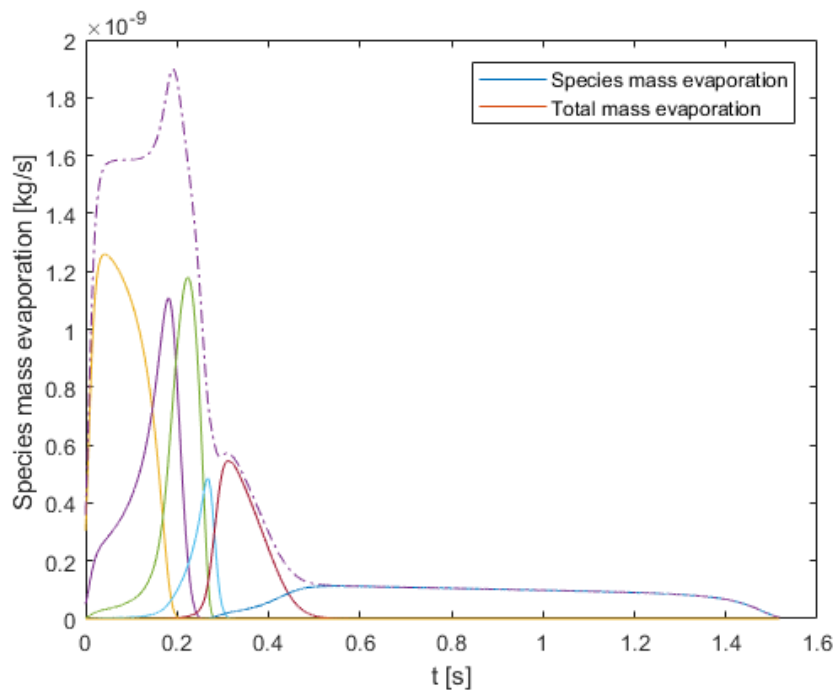
Figure 5.27 represents the liquid mass fractions with time. This gives a more clear view of how mass changes during evaporation and polymerization of levoglucosan. Now, the levoglucosan liquid mass fraction will not reach unity, since the polymerization reaction starts before phenol has disappeared. The relative difference of disappearance (with and without reaction) for levoglucosan is 0.4 %. Such a small difference means that the polymerization reaction does not influence the evaporation rate of levoglucosan.

Figure 5.28 represents the droplet temperature and diameter with time. The marker in the figures stands for the reaction starting point. Before this point is reached, no changes are observed in droplet diameter and temperature. For the droplet temperature, relative to the model without reaction, a higher temperature increase during the period of levoglucosan evaporation is observed. The specific heat of the dimer ($C_p = 1.45 \text{ kJ/kgK}$) is lower than that of the liquid phase levoglucosan ($C_p = 2.31 \text{ kJ/kgK}$). The less levoglucosan is remained in the droplet, the lower the specific heat of the solid-liquid mixture (equation 4.31) and thus the faster the droplet will heat up. That is presented at the end of the droplet temperature curve in figure in figure 5.28.

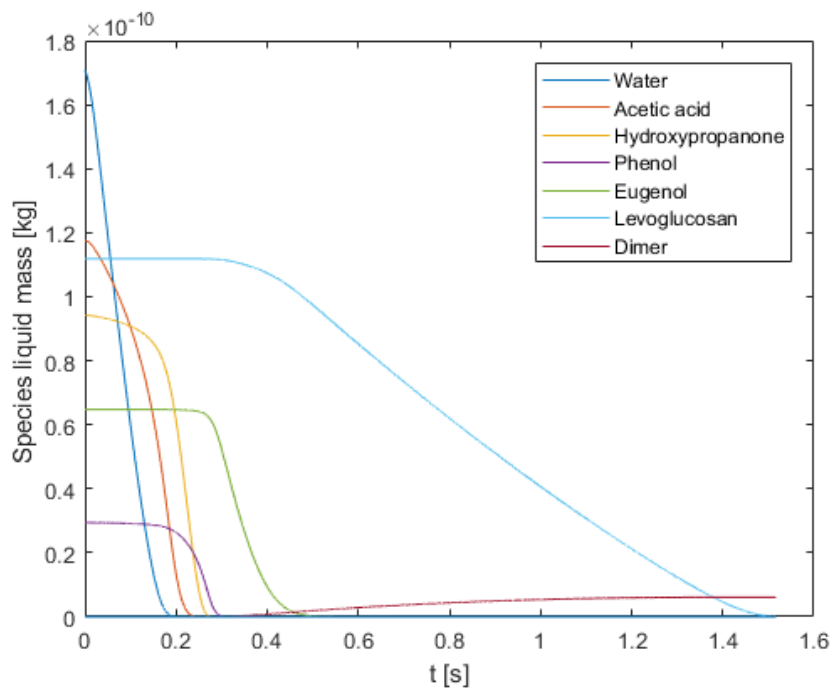
Figure 5.29 represent the heat flow terms with time. The dimer starts forming about the same time levoglucosan starts evaporating. Simultaneous evaporation and reaction, causes a steeper decline of levoglucosan.

5.3.2 Influence ambient temperature

Figure 5.30 shows the influence of variation of ambient temperature on the droplet evaporation including polymerization reaction. If the temperature is lowered (see 600 K), the maximum wet bulb temperature the droplet will reach is lower than the reaction temperature and therefore will not influence the evaporation process. For 600 K, reaction takes place very late during the evaporation process, while for the higher temperatures the reaction start earlier in the evaporation process. Furthermore, observed is, the higher the ambient temperature, the higher end wet bulb temperature during evaporation and the shorter the droplet lifetime.



(a) Variation of mass evaporation rate with time.



(b) Variation of species mass inside the droplet with time.

Figure 5.26: Species mass fractions variations with time including polymerization reaction.

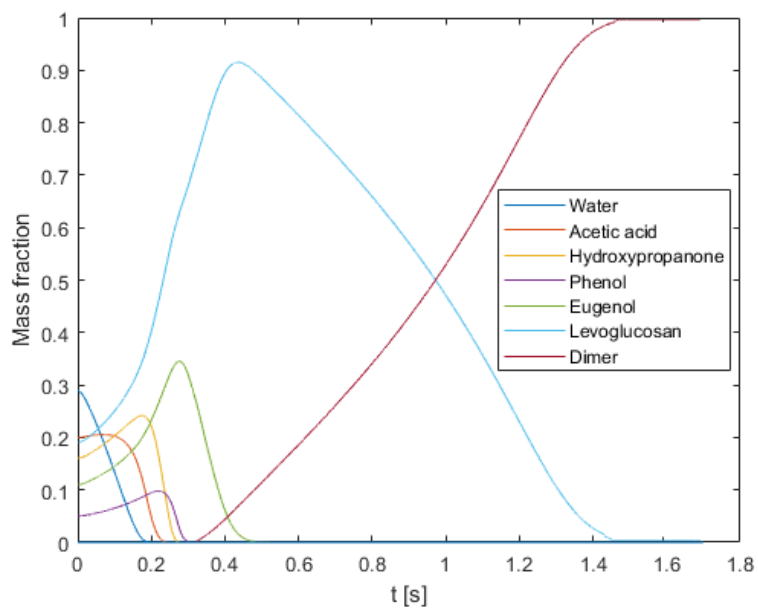
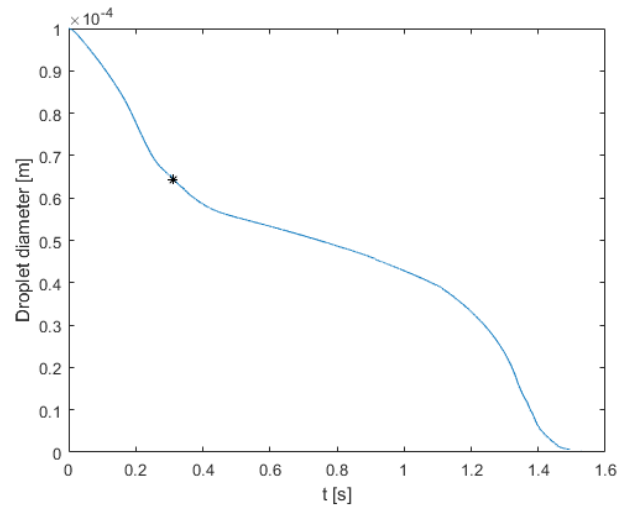
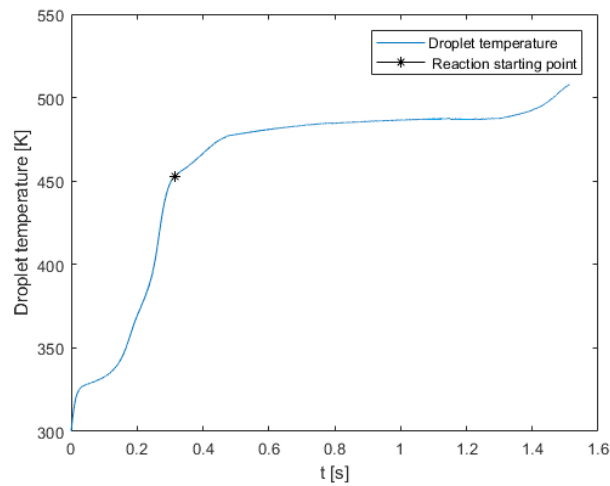


Figure 5.27: Variation of species mass fraction inside the droplet with time including polymerization reaction.



(a) Variation of droplet diameter with time.



(b) Variation of droplet temperature with time.

Figure 5.28: Species mass fractions variations with time including polymerization reaction.

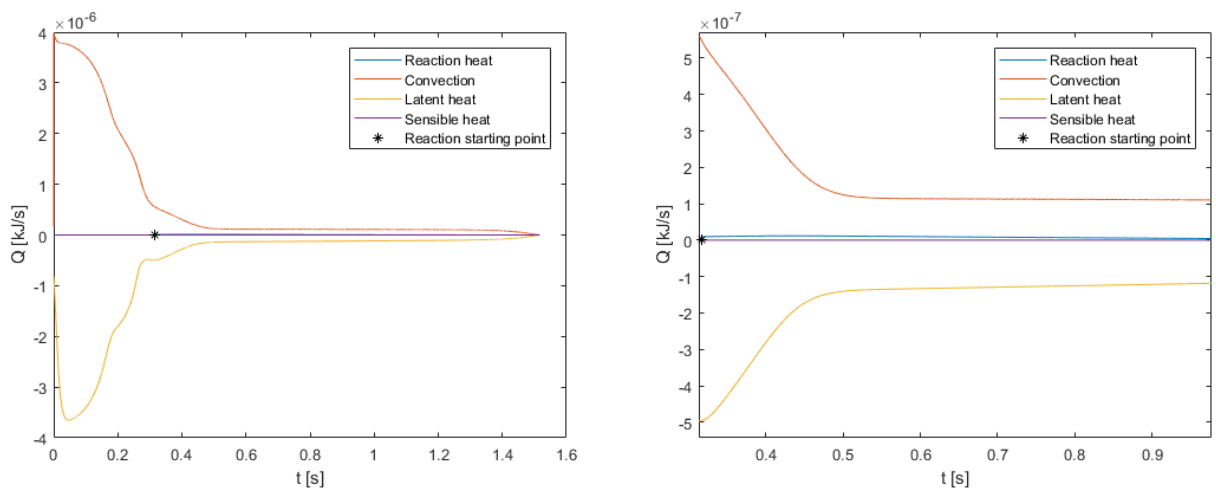


Figure 5.29: Variation of heat terms with time. Left: over the whole time range. Right: a close up of the time range where the reaction is most active.

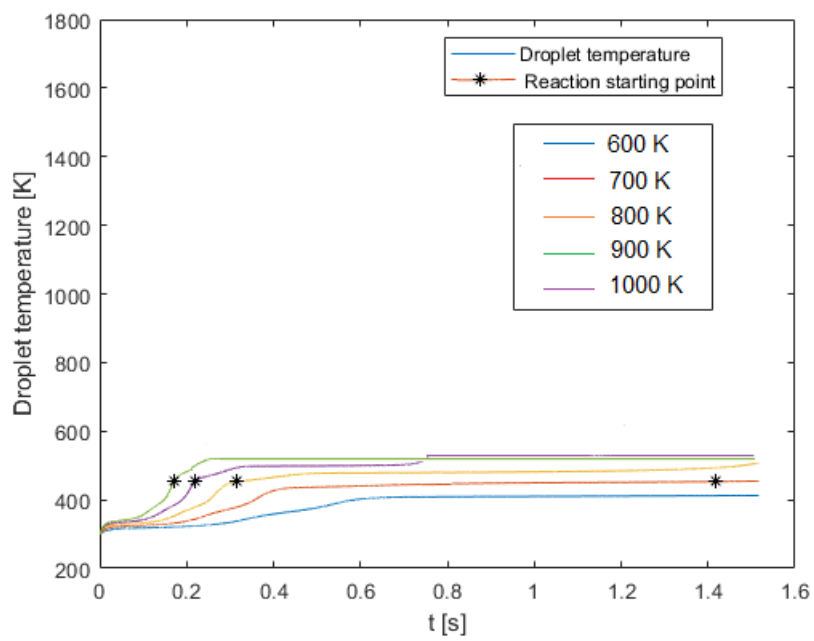


Figure 5.30: Influence of ambient temperature on droplet evaporation including polymerization reaction.

Chapter 6

Conclusions and Recommendations

This chapter presents conclusions and recommendations on the three main objectives of this study: i) the formulation of the surrogate oil, ii) the determination of the thermal physical properties and iii) the formulation of the evaporation model including liquid phase polymerization reaction.

6.1 Conclusions

6.1.1 Conclusions on formulation of the surrogate oil

Due to the complex composition of BPO and its unknown full representation in literature, a surrogate oil is formulated. The formulation is based on a discrete component model. The study of Branca et. al. [17] is used, in which the devolatilization (weight loss vs. temperature) curve of a BPO derived from woody biomass indicates six main temperature zones. For each zone, Branca et. al. experimentally identified a set of components of the BPO. The component having the highest weight loss in each of the six temperature zone is chosen and the mixture thermophysical properties are checked if they are (iteratively) matched with the properties of a real BPO. The initial liquid mass fraction is based on the mass loss of each of the six main zone, and is altered only to match the properties. The results of the model of this study show that the evaporation of water, acetic acid, hydroxypropanone, and phenol happens during the early evaporation process and shortly after each other; they are all behaving as (very to) light components. On the other hand eugenol and especially levoglucosan evaporate slow and very slow with respect to the light components. There is no gradual transition from (very) light components to heavy (very) components.

6.1.2 Conclusions on determination of the thermal physical properties

The evaporation model directly depends on the thermophysical properties, therefore different methods and, for as far as possible, experimental data is collected and compared. Relevant properties considered are: normal boiling point, critical properties, latent heat, vapor pressure, liquid phase density, liquid phase specific heat, vapor phase specific heat, vapor phase viscosity, vapor phase thermal conductivity and the gas phase diffusivity. Each method is checked on its accuracy in the temperature range (of the droplet surface temperature), its validation with experimental data and its accuracy (from literature) for polar components. Most of the experimental data is found only for acetic acid, of which no values for the whole temperature range or only for a few values spanning the

temperature range are found. Thus no clear conclusion could be drawn on the accuracy of the predicted values for acetic acid, and there is no insight on the accuracy of the approximation of the thermophysical properties for the other components .

6.1.3 Conclusions on the formulation of the evaporation model

For all the components Branca et. al. [17] identified, and for all the selected components for the surrogate oil in this study, only reaction kinetics for thermal polymerization of levoglucosan is found. Because the dimerization of levoglucosan results in a solid dimer, the reaction product was limited to only dimer formation.

The evaporation model used is the Rapid Mixing Model, which assumes infinitely fast thermal conductivity in the liquid phase and uniform but time varying droplet temperature making it only applicable in the case of very strong internal circulation or extremely small Biot number. Another assumption is ideal behaviour of the liquid mixture during evaporates. The species are evaporated at their saturated (wet bulb) temperature, resulting in a partially preferential evaporation process. The latter implies that the most volatile species start to evaporate first where after the less volatile species start to evaporate. The model is applied on a single stagnant droplet in still air. For the case of evaporation in absence of polymerization, a higher evaporation rate is observed during the early evaporation process and a slower evaporation rate for the further process. For the case including the reaction, the relative disappearance of levoglucosan is about 0.4% and no effect of the reaction on the evaporation rates is observed.

The trend of the droplet diameter squared with time (in absence of the reaction) is not in agreement with the experimental case of a real BPO, but does qualitatively agree with the experimental case of a binary hydrocarbon fuel. This can be due to: i) no full representation of the real BPO by the surrogate oil (the surrogate oil has more components which behave as light components and does not have a gradual transition from light to heavy components), ii) no temperature and composition gradient in the liquid phase, resulting in less accurate predictions, iii) no consideration of a droplet having a slip velocity and internal circulation (both result in a higher evaporation rate), iv), v) no consideration of internal bubbling is made; internal bubbling decreases the evaporation rate during the bubbling period.

In simple cases, i.e. heating and evaporating of relatively small set of components having close boiling points and molecular structure, the current model is suitable. However, in the case for a real BPO, due to a wide range of boiling points, internal bubbling can occur, which is totally neglected by the rapid mixing model. Furthermore, the endothermic polymerization reaction will promote (expected to be very small for the reaction defined in this case) local internal bubbling.

6.2 Recommendations

6.2.1 Recommendations on formulation of the surrogate oil

To have a better representation of the surrogate oil in the context of this study, it is recommended to include more components for each of the six main temperature zones based on the same procedure used in this study. In an iterative procedure for evaporation modeling, more components can be added to gain a more gradual transition between the light and heavy components.

6.2.2 Recommendations on determination of the thermal physical properties

The scarce literature experimental data of thermophysical properties of BPO components indicate that some experiments can be carried out to gain more insight in the accuracy of the predicted data. Also, more methods can be collected from literature and compared against data obtained by correlations used in this study.

6.2.3 Recommendations on the formulation of the evaporation model

Internal bubbling can have a significant effect on the droplet evaporation process. To take this effect into account, the current model needs to be expanded. A fully transient approach with variable properties in terms of time and space (both gas and liquid phase) is required in which the quasi-steady gas phase assumption still applies. The mass and energy diffusion models are now a function of both time (except gas phase) and radial direction (spherical symmetry).

Appendix A

Relevant properties of air and dimer

Table A.1 lists the important properties for air.

Table A.1: Relevant properties air at 1.01325 bar [97].

Property	Relation
$\rho [\frac{kg}{m^3}]$	$4.531115 \cdot 10^{-17} T_g^6 - 1.728796 \cdot 10^{-13} T_g^5 + 2.779958 \cdot 10^{-10} T_g^4 - 2.440042 \cdot 10^{-7} T_g^3 + 1.261352 \cdot 10^{-4} T_g^2 - 3.836228 \cdot 10^{-2} T_g + 6.347374 \cdot 10^1$
$C_p [\frac{J}{kgK}]$	$-3.653516 \cdot 10^{-15} T_{ref}^6 + 1.382918 \cdot 10^{-11} T_{ref}^5 - 2.105270 \cdot 10^{-8} T_{ref}^4 + 1.595370 \cdot 10^{-5} T_{ref}^3 + 5.903588 \cdot 10^{-3} T_{ref}^2 + 1.019694 \cdot 10^1 T_{ref} + 9.380278 \cdot 10^2$
$k [\frac{W}{mK}]$	$-1.638599 \cdot 10^{-14} T_{ref}^4 + 4.890989 \cdot 10^{-11} T_{ref}^3 - 6.427437 \cdot 10^{-8} T_{ref}^2 + 9.829044 \cdot 10^{-5} T_{ref} + 1.263900 \cdot 10^{-3}$
$\mu [\frac{Ns}{m^2}]$	$-1.719701 \cdot 10^{-17} T_{ref}^4 + 5.412211 \cdot 10^{-14} T_{ref}^3 - 7.503758 \cdot 10^{-11} T_{ref}^2 + 7.963081 \cdot 10^{-8} T_{ref} + 8.777670 \cdot 10^{-8}$

Table A.2 lists two important properties for the dimer as approximated by [89].

Table A.2: Relevant properties solid dimer at 1.01325 bar [89].

Property	Value
$\rho [\frac{kg}{m^3}]$	1250
$C_p [\frac{kJ}{kgK}]$	1.45

Appendix B

Property estimation methods

B.1 Mixing rules for thermophysical properties of the liquid- and gas mixture

The mixing rules applied to obtain the vapor-gas mixture or liquid mixture properties from the pure species properties are listed in table B.1.

Table B.1: Mixing rules applied to obtain properties for the liquid and gas phase.

Property	Mixing rule	Reference
Liquid phase		
Density	$\rho_L = \frac{1}{\sum_i (Y_{L_i} / \rho_{L_i})}$	Reid et al. [55]
Heat capacity	$C_{pL} = \sum_i (Y_{L_i} C_{pL,i})$	Reid et al. [55]
Viscosity	$\ln \mu_L = \sum_i (\chi_{L_i} \ln \mu_{L_i})$	Reid et al. [55]
Thermal conductivity	$k_L = \sum_i (Y_{L_i} k_{L,i}^2)^{-1/2}$	Reid et al. [55]
Gas phase		
Density	$\rho_V = \frac{1}{\sum_i (Y_{S_i} / \rho_{V_i})}$	Reid et al. [55]
Heat capacity	$C_{pV} = \sum_i (Y_{S_i} C_{pV,i})$	Reid et al. [55]
Viscosity	$\mu_V = \sum_i \frac{\chi_{S,i} \mu_i}{\sum_{j \neq i} \chi_{S,j} \phi^{ij}}$	Bird et al. [96]
Thermal conductivity	$k_V = \sum_i \frac{\chi_{S,i} k_i}{\sum_j \chi_{S,j} \phi^{ij}}$	Bird et al. [96]
	$\phi^{ij} = \frac{1}{\sqrt{8}} \left(1 + \frac{M_i}{M_j}\right)^{-1/2} \left[\left(1 + \frac{\mu_{V,i}}{\mu_{V,j}}\right)^{1/2} \left(\frac{M_i}{M_j}\right)^{1/4} \right]^2$	Bird et al. [96]
Diffusion coefficient	$D_{i,g} = \frac{1 - \chi_{S_i}}{\sum_{j \neq i} \frac{\chi_{S,j}}{D_{ij}}}$	Reid et al. [55]
Latent heat of evaporation	$L_V = \sum_i (\varepsilon_i L_{V,i})$	Reid et al. [55]

B.2 Joback group contribution method

The corresponding chemical bonds for selected components are listed in table B.2, except for water whose properties are obtained from the fluid data base of ref. [97]. The R , P , and A denote a ring, a phenol, and an alcohol, respectively. The number in between brackets counts the groups appearing in the molecule.

Table B.2: Contributing groups of selected components.

Acetic acid	-CH ₃ - (1)	C = O(1)	OH-A (1)					
Hydroxypropanone	-CH ₃ - (1)	C=O (1)	OH-A (1)	-CH ₂ - (2)				
Phenol	OH-P (1)	=CH-R (5)	=C-R (1)					
Eugenol	OH-P (1)	-CH ₃ - (1)	-O- (1)	=CH- (1)	=CH ₂ (1)	=CH-R (3)	=C-R (3)	-CH ₂ - (1)
Levoglucosan	OH-P (3)	-O- (2)	CH-R (5)	-CH ₂ - (1)				
Dimer	OH-P (5)	-O- (4)	CH-R (10)	-CH ₂ - (2)	OH-A (1)			

The relevant properties obtained from the Joback method are listed in table B.3. Here N_{atoms} is the number of atoms in the molecule, and the T in $C_{p,V}$ is the T_{ref} . Table B.4 lists data for each contributing group for each property.

Table B.3: Relevant property estimation functions obtained from table C.1 from [55].

Property	Function
Boiling temperature [K]	$T_b = 198 + \sum_k N_k \cdot T_{b_k}$
Critical temperature [K]	$T_c = T_b [0.5840.965 \sum_k T_{c,k} - (T_{c,k})^2]$
Critical pressure [bar]	$p_c = 0.113 + 0.0032 N_{atoms} - \sum_k N_k p_{c,k}$
Melting temperature [K]	$T_m = 122 + \sum_k N_k \cdot T_{m_k}$
Latent heat of vaporization [J/mol]	$H_v = 15.30 + \sum_k N_k \cdot \Delta H_{v_k} \cdot 0.004184$
Isobaric specific heat gas phase [J/mol · K]	$C_{p,V} = [\sum_k C_{p,ak} - 37.93] + [\sum_k N_k C_{p,bk} + 0.21]T$ $+ [\sum_k N_k C_{p,ck} - 3.91 \cdot 10^{-4}]T^2 + [\sum_k N_k C_{p,dk} + 2.06 \cdot 10^{-7}]T^3$

Table B.4: Property estimation data obtained from table C.1 from [55].

Group	T_{b_k} [K]	T_{m_k} [K]	T_{c_k} [K]	$p_{c,k}$ [bar]	ΔH_{v_k} [J/mol]	ΔH_{m_k} [J/mol]	$C_{p,ak}$ [$\frac{J}{mol \cdot K}$]	$C_{p,bk}$ [$\frac{J}{mol \cdot K}$]	$C_{p,ck}$ [$\frac{J}{mol \cdot K}$]	$C_{p,dk}$ [$\frac{J}{mol \cdot K}$]
-CH ₂ -	22.88	11.27	0.0189	0.000	2225.888	2589.896	-0.909	9.50E-02	-5.44E-05	1.19E-08
>CH-	21.74	12.64	0.0164	0.0020	1690.336	748.936	23.000	2.04E-01	-2.65E-04	1.20E-07
>C<	18.25	46.43	0.0067	0.0043	635.968	-1460.216	66.200	4.27E-01	-6.41E-04	3.01E-07
-CH ₃ -	23.58	-5.10	0.0141	-0.0012	2372.328	907.928	19.500	-8.08E-03	1.53E-04	-9.67E-08
=CH ₂ <	18.18	-4.32	0.0113	-0.0028	1723.808	-472.792	-23.600	-3.81E-02	1.72E-04	-1.03E-07
=CH-	24.96	8.73	0.0129	-0.0006	2204.968	2690.312	-8.000	1.05E-01	-9.63E-05	3.56E-08
>C=	24.14	11.14	0.0117	0.0011	2138.024	3062.688	28.100	2.08E-01	-3.06E-04	1.46E-07
-O-(non ring)	22.42	22.23	0.0168	0.00115	2410	1188	2.55E+01	-6.32E-02	1.11E-04	-5.48E-08
>C=O	76.75	61.2	0.038	0.0031	8972	4189	6.45	6.70E-02	-3.57E-05	2.86E-09
=C<R	31.01	37.02	0.0143	0.0008	3059	2394	-8.25	1.01E-01	-1.42E-04	6.78E-08
=CH-R	26.73	8.13	0.0082	0.0011	2544	1101	-2.14	5.74E-02	-1.64E-06	-1.59E-08
-OH (P)	76.34	82.83	0.024	0.0184	12499	4490	-2.81	1.11E-01	-1.16E-04	4.94E-08
-OH (A)	92.88	44.45	0.0741	0.0112	16826	2406	2.57E+01	-6.91E-02	1.77E-04	-9.88E-08

B.3 Chueh and Swanson group contribution data for specific heat liquid phase calculations

To calculate the liquid phase isobaric specific heat, the Chueh and Swanson correlation is used of which molecule groups contribution data is included in table B.5.

B.4 The Reichenberg method for vapor phase viscosity calculations

The vapor phase viscosity, μ_V , is obtained by equation B.1.

$$\mu_V = \frac{M^{1/2} T_{ref}}{a^* [1 + \frac{4}{T_c}] [1 + 0.36 * T_r (T_r - 1)]^{1/6}} \frac{T_r (1 + 270 \mu_{dp,r}^4)}{T_r + 270 \mu_{dp,r}^4} \quad (\text{B.1})$$

Here $\mu_{dp,r}$ is the reduced dipole moment defined in equation B.2 (dipole moment in debyes, p_c in bar and T_c is Kelvin), in which the dipole moments μ_{dp} are listed in table B.7. The parameter a^* is defined as in equation B.3. Here C_k is the group obtained from table B.6.

$$\mu_{dp,r} = 52.46 \frac{\mu_{dp}^2 p_c}{T_c^2} \quad (\text{B.2})$$

$$a^* = \sum_k n_k C_k \quad (\text{B.3})$$

Table B.5: Chueh and Swanson group contributions data [$kJ/kmol \cdot K$] for liquid heat capacity at 293.15 K [95].

Group	Value	Group	Value
		O —C—O—	60.71
—CH ₃	36.84	—CH ₂ OH	73.27
—CH ₂ —	30.40	— CHOH	76.20
— CH—	20.93	— COH	111.37
— C—	7.37	—OH	44.80
		—ONO ₂	119.32
==CH ₂	21.77		
==C—H	21.35	Halogen	
==C—	15.91	—Cl (first or second on a carbon)	36.01
		—Cl (third or fourth on a carbon)	25.12
—C≡H	24.70	—Br	37.68
—C≡	24.70	—F	16.75
		—I	36.01
		Nitrogen	
		H H—N—	58.62
— CH=	18.42	H —N—	43.96
— C= or — C—	12.14	—N—	31.40
—C=	22.19	—N≡ (in a ring)	18.84
—CH ₂ —	25.96	—C≡N	58.70
		Sulphur	
—O—	35.17	—SH	44.80
—C=O	53.00	—S—	33.49
—C—O H	53.00	Hydrogen	
—C—OH	79.97	H— (for formic acid, formates, hydrogen cyanide, etc.)	14.65

Add 18.84 for any carbon group which fulfils the following criterion: a carbon group which is joined by a single bond to a carbon group connected by a double or triple bond with a third carbon group. In some cases a carbon group fulfils the above criterion in more ways than one; 18.84 should be added each time the group fulfils the criterion.

Exceptions to the above 18.84 rule:

1. No such extra 18.84 additions for —CH₃ groups.
2. For a —CH₂— group fulfilling the 18.84 addition criterion add 10.47 instead of 18.84. However, when the —CH₂— group fulfils the addition criterion in more ways than one, the addition should be 10.47 the first time and 18.84 for each subsequent addition.
3. No such extra addition for any carbon group in a ring.

Table B.6: Values of the Group Contributions C_k for the Estimation of a^* (Reichenberg, 1971) [55]

Group	Contribution C_k	Group	Contribution C_k
—CH ₃	9.04	\backslash C=(ring)	3.59
\backslash CH ₂ (nonring)	6.47	—F	4.46
\backslash CH—(nonring)	2.67	—Cl	10.06
\backslash C (nonring)	-1.53	—Br	12.83
=CH ₂	7.68	—OH (alcohols)	7.96
=CH—(nonring)	5.53	\backslash O (nonring)	3.59
\backslash C—(nonring)	1.78	\backslash C=O (nonring)	12.02
≡CH	7.41	—CHO (aldehydes)	14.02
≡C—(nonring)	5.24	—COOH (acids)	18.65
\backslash CH ₂ (ring)	6.91	—COO—(esters) or HCOO (formates)	13.41
\backslash CH—(ring)	1.16	—NH ₂	9.71
\backslash C (ring)	0.23	\backslash NH (nonring)	3.68
=CH—(ring)	5.90	≡N—(ring)	4.97
		—CN	18.15
		\backslash S (ring)	8.86

Table B.7: Dipole moments of the selected components in vapor phase [89].

Component	μ_{dp} [Debye]
Water	1.85
Acetic acid	1.74
Hydroxypropanone	2.19
Phenol	1.45
Eugenol	2.02
Levoglucosan	3.32

B.5 Roy and Thodos method for vapor phase thermal conductivity calculations

The reduced thermal conductivity is expressed as in equation B.5 [55].

$$\tau = 210 \cdot \left[\frac{T_c M^3}{p_c^4} \right]^{1/6} \quad (\text{B.4})$$

The reduced thermal conductivity was employed by Roy and Thodos separated the thermal conductivity calculation into two parts. The first, attributed only to translational energy and this part varies only with the reduced temperature. In the second, the contribution from rotational, vibrational interchange, etc., was related to the reduced temperature and a specific constant estimated from group contributions. The final equation may be written as in equations B.5, B.6, B.7

$$k_v = (\lambda\tau)_{tr} + (\lambda\tau)_{int} \quad (\text{B.5})$$

$$(\lambda\tau)_{tr} = 8.757 \cdot [\exp(0.0464T_r) - \exp(-0.2412T_r)] \quad (\text{B.6})$$

$$(\lambda\tau)_{int} = C \cdot fn(T_r) \quad (\text{B.7})$$

Relations for $fn(T_r)$ are shown in table B.8. The constant C is specific for each material, and it is estimated by a group contribution technique as shown below.

Table B.8: Recommended $fn(T_r)$ equations for the Roy-Thodos Method [55].

Saturated hydrocarbons†	$-0.152T_r + 1.191T_r^2 - 0.039T_r^3$
Olefins	$-0.255T_r + 1.065T_r^2 + 0.190T_r^3$
Acetylenes	$-0.068T_r + 1.251T_r^2 - 0.183T_r^3$
Naphthalenes and aromatics	$-0.354T_r + 1.501T_r^2 - 0.147T_r^3$
Alcohols	$1.000T_r^2$
Aldehydes, ketones, ethers, esters	$-0.082T_r + 1.045T_r^2 + 0.037T_r^3$
Amines and nitriles	$0.633T_r^2 + 0.367T_r^3$
Halides	$-0.107T_r + 1.330T_r^2 - 0.223T_r^3$
Cyclic compounds‡	$-0.354T_r + 1.501T_r^2 - 0.147T_r^3$

† Not recommended for methane.

‡ For example, pyridine, thiophene, ethylene oxide, dioxane, piperidine.

Table B.9: Roy and Thodos group contribution data [55].

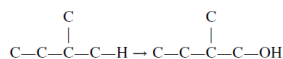
Type: 1	2	3	4
Paraffinic Hydrocarbons			
Base group, methane	0.73		
First methyl substitution	2.00		
Second methyl substitution	3.18		
Third methyl substitution	3.68		
Fourth and successive methyl substitutions	4.56		

For example, C for n -octane is equal to $C = \Sigma\Delta C = [0.73 + 2.00 + 3.18 + 3.68 + 4(4.56)] = 27.8$

Alcohols. Synthesize the corresponding hydrocarbon with the same carbon structure and calculate C as noted above. Replace the appropriate hydrogen atom by a hydroxyl group and correct C as noted:

Type of —OH substitution	ΔC
On methane	3.79
1 → 1	4.62
2 → 1	4.11
3 → 1	3.55
4 → 1	3.03
1 → 2 → 1	4.12

The notation is the same as that used earlier; for example, 3 → 1 indicates that the —OH group is replacing a hydrogen atom on a type 1 carbon which is adjacent to a type 3 carbon:

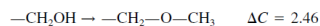


These rules apply only to aliphatic alcohols, and they are incomplete even for them.

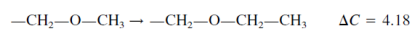
Aldehydes and Ketones. Synthesize the hydrocarbon analog with the same number of carbon atoms and calculate C as noted above. Then form the desired aldehyde or ketone by substituting oxygen for two hydrogen atoms:

	ΔC
—CH ₂ —CH ₃ → —CH ₂ —CHO	1.93
—CH ₂ —CH ₂ —CH ₂ — → —CH ₂ —CO—CH ₂	2.80

Ethers. Synthesize the primary alcohol with the longest carbon chain on one side of the ether oxygen. Convert this alcohol to a methyl ether.



Extend the methyl chain, if desired, to an ethyl.



Although Roy and Thodos do not propose extensions beyond the ethyl group, presumably more complex chains could be synthesized by using ΔC values obtained from paraffinic and isoparaffinic contributions.

Acids and Esters. Synthesize the appropriate ether so as to allow the following substitutions:

	ΔC
—CH ₂ —O—CH ₃ → —CH ₂ —O—C=O	0.75
—CH ₂ —O—CH ₂ — → —CH ₂ —O—C(=O)—	0.31

Cyclics. Synthesize the ring, if possible, with the following contributions (not substitutions):

Group	ΔC
—CH ₂ —	4.25
—CH=	3.50
—NH—	4.82
—N=	3.50
—O—	3.61
=S=	7.01

B.6 Fuller-Schettler-Giddings atomic diffusion volumes data for binary diffusion coefficient calculations

Table B.10 represents the atomic diffusion volumes to calculate the binary diffusion coefficient. In the upper part of the table are listed the diffusion volume increments to be summed when applying the method to organic vapors other than simple gases (such as N_2 , CO_2 , etc.). The values for the simple gases are listed in the lower part [90].

Table B.10: Atomic diffusion volumes [cm^3] [90].

Atomic and Structural Diffusion Volume Increments			
C	16.5	(Cl)	19.5
H	1.98	(S)	17.0
O	5.48	Aromatic or Hetero-	
(N) ^b	5.69	cyclic rings	−20.2
Diffusion Volumes of Simple Molecules			
H ₂	7.07	CO ₂	26.9
D ₂	6.70	N ₂ O	35.9
He	2.88	NH ₃	14.9
N ₂	17.9	H ₂ O	12.7
O ₂	16.6	(CCl ₂ F ₂)	114.8
Air	20.1	(SF ₆)	69.7
Ne	5.59		
Ar	16.1	(Cl ₂)	37.7
Kr	22.8	(Br ₂)	67.2
(Xe)	37.9	(SO ₂)	41.1
CO	18.9		

^a $b = 1.75$.

^b () indicates that listed value is based on only a few data points.

B.7 Schroeder's Method atomic contribution volumes data for latent heat at boiling calculations

Table B.11 represents the atomic contribution volumes to calculate the latent heat at the boiling point.

Table B.11: V_b Contributions in Schroeder's Method [94].

Atom	$(V_b)_k^a$	Atom	$(V_b)_k^a$	Ring/Bond	$(V_b)_k^{\text{extra } a}$
H	7	F	10.5	Ring	-7
C	7	Cl	24.5	Single bond	0
N	7	Br	31.5	Double bond	7
O	7	I	38.5	Triple bond	14
S	21				

^a $(V_b)_k$ in $\text{cm}^3 (\text{mol})^{-1}$.

Bibliography

- [1] Demirbas & Ayhan. *Biofuels: Securing the Planet's Future Energy Needs*, ISBN-13: 978-1848820104, Springer, London, UK, 2009.
- [2] B. Maddi, S.Viamajala, S Varanasi, Comparative study of pyrolysis of algal biomass from natural lake blooms with lignocellulosic biomass, *Journal of Bioresource Technology* 102 (2011): 11018–11026.
- [3] D. Mohan, C. U. Pittman, Jr., P. H. Steele, Pyrolysis of Wood/Biomass for pyrolysis oil: A Critical Review, *Journal of Energy & Fuels* 20 (2006): 848-889.
- [4] Y. M. Isa, E. Ti. Ganda, pyrolysis oil as a potential source of petroleum range fuels, *Journal of Renewable and Sustainable Energy Reviews* 81 (2018): 69–75.
- [5] V. Dhyani, T. Bhaskar, A comprehensive review on the pyrolysis of lignocellulosic biomass, *Journal of Renewable Energy* xxx (2017): 1-22.
- [6] K. Li, L. Zhang, L. Zhu, X. Zhu, A comprehensive review on the pyrolysis of lignocellulosic biomass, *Journal of Bioresource Technology* 234 (2017): 48–52.
- [7] J. L. H. P. Sallevelt, A. K. Pozarlik, G. Brem, Numerical study of pyrolysis oil combustion in an industrial gas turbine, *Journal of Energy Conversion and Management* 127 (2016) 504–514.
- [8] A. Frassoldati, A Cuoci, A. Stagni, T. Faravelli, R. Calabria, P. Massoli, THERMO-PHYSICAL CHARACTERIZATION OF FPBO AND PRELIMINARY SURROGATE DEFINITION, Residue2Heat Consortium, 2017.
- [9] A.R.K. Gollakotaa, N. Kishoreb, S. Gua, A review on hydrothermal liquefaction of biomass, *Journal of Renewable and Sustainable Energy Reviews* 81 (2018) 1378–1392.
- [10] A. Ganesh, K. Raveendran, Biomass selection criteria for pyrolytic conversion processes, *Prog. Thermochem. Biomass Convers.* (2001) 1025-1033.
- [11] R. E. Guedesa, A. S. Lunaa, A. R.Torres, Operating parameters for pyrolysis oil production in biomass pyrolysis: A review, *Journal of Analytical and Applied Pyrolysis* 129 (2018) 134–149.
- [12] P. Basu , *Biomass Gasification and Pyrolysis*, Elsevier Inc, ISBN: 978-0-12-374988-8, 2010.
- [13] S. Arnold, K. Moss, M. Henkel, R. Hausmann, Biotechnological Perspectives of Pyrolysis Oil for a Bio-Based Economy, *Trends in Biotechnology* Volume 35, Issue 10, October 2017, Pages 925-936.

- [14] S. A. Ashter, *Technology and Applications of Polymers Derived from Biomass* 1st Edition, Elsevier Inc, ISBN: 9780323511155, 2017.
- [15] L. M. L. Laurens, T. A. Dempster, H. D. T. Jones, E. J. Wolfrum, S. Van Wychen, J. S. P. McAllister, M. Rencenberger, K. J. Parchert, L. M. Gloe, Algal Biomass Constituent Analysis: Method Uncertainties and Investigation of the Underlying Measuring Chemistries, *Journal of Anal. Chem.*, 2012, 84 (4), pp 1879–1887.
- [16] A. Oasmaa, S. Czernik, Fuel Oil Quality of Biomass Pyrolysis Oils State of the Art for the End Users, *Journal of Energy Fuels*, 1999, 13 (4), pp 914–921.
- [17] C. Branca, A. Albano, C. D. Blasi, Critical evaluation of global mechanisms of wood devolatilization, *Journal of Thermochimica Acta* Volume 429, Issue 2, 15 May 2005, Pages 133-141.
- [18] A. H. Mahmoudia, A. K. Pozarlik E. van der Weide, S. R. A. Kersten, S. Luding, G. Breme, Effect of char on the combustion process of multicomponent bio-fuel, *Journal of Chemical Engineering Science* Volume 175, 16 January 2018, Pages 286-295.
- [19] S. Wu, H. Yang, J. Hu, D. Shen, H. Zhang, R. Xiao, The miscibility of hydrogenated pyrolysis oil with diesel and its applicability test in diesel engine: A surrogate (ethylene glycol) study, *Journal of Fuel Processing Technology* Volume 161, 15 June 2017, Pages 162-168.
- [20] R. C. Brown, K. Wang, *Fast Pyrolysis of Biomass: Advances in Science and Technology*, Green Chemistry Series No. 50, The Royal Society of Chemistry, 2017.
- [21] M. I. Jahirul, M. G. Rasul, A. A. Chowdhury, N. Ashwath, Biofuels Production through Biomass Pyrolysis — A Technological Review, *Journal of Energies* 2012, 5(12), 4952-5001.
- [22] J. Yanik, R. Stahl, N. Troeger, A. Sinag, Pyrolysis of algal biomass, *Journal of Analytical and Applied Pyrolysis*, Volume 103, September 2013, Pages 134-141.
- [23] F. Monlau, C. Sambusiti, A. Barakat, M. Quéméneur, E. Trably, J. -P. Steyer, H. Carrère, Do furanic and phenolic compounds of lignocellulosic and algae biomass hydrolyzate inhibit anaerobic mixed cultures? A comprehensive review, *Journal of Biotechnology Advances* 32 (2014) 934–951.
- [24] D. Shen, R. Xiao, S. Gu, H. Zhang, The Overview of Thermal Decomposition of Cellulose in Lignocellulosic Biomass, *InTechOpen*, 2013.
- [25] J. L. H. P. Sallevelt, A. K. Pozarlik, G. Brem, Characterization of viscous biofuel sprays using digital imaging in the near field region, *Journal of Applied Energy* Volume 147, 1 June 2015, Pages 161-175.
- [26] C. Branca, C. D. Blasi, C. Russo, Devolatilization in the temperature range 300–600 K of liquids derived from wood pyrolysis and gasification, *Journal of Fuel* Volume 84, Issue 1, January 2005, Pages 37-45.
- [27] M. J. Wornat, B. G. Porter, N. Y. C. Yang, Single Droplet Combustion of Biomass Pyrolysis Oils, *Journal of Energy & Fuels* 1994, 8, 1131-1142.
- [28] M. S. Wu, S. I. Yang, Combustion characteristics of multi-component cedar pyrolysis oil/kerosene droplet, *Journal of Energy* 113 (2016) 788-795.

- [29] G. van Rossum, B. M. Güell, R. P. B. Ramachandran, K. Seshan, L. Lefferts, W. P. M. Van Swaaij, S. R. A. Kersten, *Evaporation of Pyrolysis Oil: Product Distribution and Residue Char Analysis*, American Institute of Chemical Engineers, Wiley InterScience, 2010.
- [30] S. Czernik, A. V. Bridgwater, *Overview of Applications of Biomass Fast Pyrolysis Oil*, *Journal of Energy Fuels*, 2004, 18 (2), pp 590–598.
- [31] K. Li, L. Zhang, L. Zhu, X. Zhu, *Comparative study on pyrolysis of lignocellulosic and algal biomass using pyrolysis-gas chromatography/mass spectrometry*, *Journal of Bioresource Technology* 234 (2017) 48–52.
- [32] R. A. Voloshin, M. V. Rodionova, S. K. Zharmukhamedov, T. N. Veziroglu, S. I. Allakhverdiev, *Review: Biofuel production from plant and algal biomass*, *International Journal of Hydrogen Energy* 41 (2016) 17257-7273.
- [33] Y. Chen, Y. Wu, D. Hua, C. Li, M. P. Harold, J. Wanga, M. Yanga, *Thermochemical conversion of low-lipid microalgae for the production of liquid fuels: challenges and opportunities*, *Journal of RSC Advances* 5 (2015) 18673-18701.
- [34] A. V. Bridgwater, G. V. C. Peacocke, *Fast pyrolysis processes for biomass*, *Journal of Renewable and Sustainable Energy Reviews* 4 (2000) 1-73.
- [35] Y. Chhiti, S. Salvador, J. Commandré, F. Broust, *Thermal decomposition of bio-oil: Focus on the products yields under different pyrolysis conditions*, *Journal of Fuel* Volume 102, December 2012, Pages 274-281.
- [36] A. R. Teixeira, R. J. Hermann, J. S. Kruger, W. J. Suszynski, L. D. Schmidt, D. P. Schmidt, P. J. Dauenhauer, *Microexplosions in the Upgrading of Biomass-Derived Pyrolysis Oils and the Effects of Simple Fuel Processing*, *Journal of ACS Sustainable Chem. Eng.* 2013, 341348.
- [37] T. N. Trinh, P. A. Jensen, K. Dam-Johansen, N. O. Knudsen, H. R. Sørensen, S. Hvilsted, *Comparison of Lignin, Macroalgae, Wood, and Straw Fast Pyrolysis*, *Journal of Energy Fuels* 2013, 3991409.
- [38] J. Brett, A. Ooi, J. Soria, *The effect of internal diffusion on an evaporating bio-oil droplet - The chemistry free case*, *Journal of biomass and bioenergy* 34 (2010) 1134-1140.
- [39] T. Kitano, J. Nishio, R. Kurose, S. Komori, *Effects of ambient pressure, gas temperature and combustion reaction on droplet evaporation*, *Journal of Combustion and Flame* 161 (2014) 551–564.
- [40] Chungen Yin, *Modelling of heating and evaporation of n-Heptane droplets: Towards a generic model for fuel droplet/particle conversion*, *Journal of Fuel* Volume 141, 1 February 2015, Pages 64-73.
- [41] L. Zhang, S. Kong, *Multicomponent vaporization modeling of bio-oil and its mixtures with other fuels*, *Journal of Fuel* Volume 95, May 2012, Pages 471-480.
- [42] B. Abramzon, W. A. Sirignano, *Droplet vaporization for model spray combustion calculations*, *Int. J. Heat Mass Transfer* 32(9):1605–1618, 1989.
- [43] N. A. Beishuizen, *PDF modelling and particle-turbulence interaction of turbulent spray flames*, Phd., 2007.

- [44] R. S. Miller, K. Harstad, J. Bellan, Evaluation of equilibrium and non-equilibrium evaporation models for many-droplet gas-liquid flow simulations, *International Journal of Multiphase Flow* 24:1025-1055, 1998.
- [45] B. Abramzon, W. A. Sirignano, Droplet vaporization for model spray combustion calculations, *Int. J. Heat Mass Transfer* 32(9):1605–1618, 1989.
- [46] D. B. Spalding, *Combustion and Mass Transfer* 1st Edition, eBook ISBN: 9781483136356, 1979.
- [47] C. K. Law, RECENT ADVANCES IN DROPLET VAPORIZATION AND COMBUSTION, *Prog, Energ Combust. Sci.*, Vol. 8. pp. 171-201, 1982.
- [48] W. A. Sirignano, *Fluid Dynamics and Transport of Droplets and Sprays* Second Edition, ISBN: 978-0-521-88489-1 (hardback), 2010.
- [49] W.L.H.Hallett, N.A.Clark, A model for the evaporation of biomass pyrolysis oil droplets, *Journal of Fuel* Volume 85, Issue 4, March 2006, Pages 532-544.
- [50] J. D. Brett, A. Ooi, J. Soria, Numerical simulations of an evaporating bio-oil droplet, 16th Australasian Fluid Mechanics Conference Crown Plaza, Gold Coast, Australia 2-7 December 2007.
- [51] F. M. Hossain, M. N. Nabi, T. J. Rainey, T. Bodisco, M. M. Rahman, K. Suara, S. M. A. Rahman, T. C. Van, Z. Ristovski, R. J. Brown, Investigation of microalgae HTL fuel effects on diesel engine performance and exhaust emissions using surrogate fuels, *Journal of Energy Conversion and Management* Volume 152, 15 November 2017, Pages 186-200.
- [52] C. Branca, P. Giudicianni, C. D. Blasi, GC/MS Characterization of Liquids Generated from Low-Temperature Pyrolysis of Wood, *Journal of Ind. Eng. Chem. Res.* 2003, 42, 3190-3202.
- [53] N. Hashimoto, H. Nomura, M. Suzuki, T. Matsumoto, H. Nishida, Y. Ozawa, Evaporation characteristics of a palm methyl ester droplet at high ambient temperatures, *Fuel* Volume 143, 1 March 2015, Pages 202-210.
- [54] X. Chen, E. Khani, C. P. Chen, A unified jet fuel surrogate for droplet evaporation and ignition, *Fuel* 182 (2016) 284–291.
- [55] R. C. Reid, J. M. Prausnitz, B. E. Poling, *The Properties of Gases & Liquids*, 4th ed, New York: McGraw-Hill; 1987.
- [56] Hazardous Substances Data Bank (HSDB), September, 2018..
- [57] C. J. Mueller, W. J. Cannella, T.J. Bruno, B. Bunting, H. D. Dettman, J. A. Franz, M. L. Huber, M. Natarajan, W. J. Pitz, M. A. Ratcliff, K. Wright, Methodology for Formulating Diesel Surrogate Fuels with Accurate Compositional, Ignition-Quality, and Volatility Characteristics, *Energy Fuels*, 2012, 26 (6), pp 3284–3303.
- [58] G. L. Juste, J.J. S. Monfort, Preliminary test on combustion of wood derived fast pyrolysis oils in a gas turbine combustor, *Ignition-Quality, and Volatility Characteristics*, *Biomass and Bioenergy* 19 (2000) 119-128.

- [59] T. Tzanetakis, N. Farra, S. Moloodi, W. Lamont, A. McGrath, M. J. Thomson, Spray Combustion Characteristics and Gaseous Emissions of a Wood Derived Fast Pyrolysis Liquid-Ethanol Blend in a Pilot Stabilized Swirl Burner, Ignition-Quality, and Volatility Characteristics, *Energy Fuels* 2010, 24, 5331–5348.
- [60] Sergei S. Sazhin, Modelling of fuel droplet heating and evaporation: Recent results and unsolved problems, *Fuel* 196 (2017) 69–101.
- [61] C. Tsekos, Fast Pyrolysis of Woody Biomass in a Pyroprobe Reactor: Effect of Torrefaction on the Pyrolysis Products, Master Thesis, Technical University Delft, 2016.
- [62] A. Cavarzere, M. Morini, M. Pinelli, P. R. Spina, A. Vaccari, M. Venturini, Experimental Analysis of a Micro Gas Turbine Fuelled with Vegetable Oils from Energy Crops, *Energy Procedia* Volume 45, 2014, Pages 91-100.
- [63] M. Beran, Pyrolysis oil application in opra gas turbines 2011.
- [64] M. Beran, L. Axelsson, Development and Experimental Investigation of a Tubular Combustor for Pyrolysis Oil Burning, *Journal of Engineering for Gas Turbines and Power* 137(3), 031508 (Oct 07, 2014).
- [65] A. P. Pinheiro, J. M. Vedovoto, Evaluation of Droplet Evaporation Models and the Incorporation of Natural Convection Effects, *Flow, Turbulence and Combustion*, 25 July 2018.
- [66] S. I. Yang, M. S. Wu, The droplet combustion and thermal characteristics of pinewood bio-oil from slow pyrolysis, *Journal of Energy* Volume 141, 15 December 2017, Pages 2377-2386 .
- [67] C. A. Mullen, A. A. Boateng, Chemical Composition of Bio-oils Produced by Fast Pyrolysis of Two Energy Crops, *Journal of Energy Fuels*, 2008, 22 (3), pp 2104–2109.
- [68] Z. Abdel-Qader, W. L. H. Hallett, The role of liquid mixing in evaporation of complex multicomponent mixtures: modelling using continuous thermodynamics, *Journal of Chemical Engineering Science* Volume 60, Issue 6, March 2005, Pages 1629-1640 .
- [69] N. V. Legault, W. L. H. Hallett, Modelling biodiesel droplet evaporation using continuous thermodynamics, *Journal of Fuel* 90 (2011) 1221–1228 .
- [70] A. Oasmaa, E. Kuoppala, Y. Solantausta, Fast Pyrolysis of Forestry Residue. 2. Physicochemical Composition of Product Liquid, *Journal of Energy Fuels* 2003, 17, 433-443 .
- [71] E. C. Okoroigwe, Z. Li, S. Kelkar, C. Saffron, S. Onyegegbu, Fast Pyrolysis of Forestry Residue. 2. Physicochemical Composition of Product Liquid, *Journal of Energy in Southern Africa*, Vol 26 No 2, May 2015.
- [72] A. Oasmaa, D. C. Elliott, S. Müller, Quality Control in Fast Pyrolysis Bio-Oil Production and Use, *Journal of Environmental Progress Sustainable Energy* (Vol.28, No.3).
- [73] A. Oasmaa, C. Peakcocke, A guide to physical property characterisation of biomass derived fast pyrolysis liquids, Technical Research Center of Finland, ESPOO 2001.

- [74] T. Ba, A. Chaala, M. Garcia-Perez, C. Roy, Colloidal Properties of Bio-Oils Obtained by Vacuum Pyrolysis of Softwood Bark. *Storage Stability, Energy Fuels* 2004, 18, 188-201.
- [75] G. W. Huber, S. Iborra, A. Corma, Synthesis of Transportation Fuels from Biomass: Chemistry, Catalysts, and Engineering, *Chem. Rev.*, 2006, 106 (9), pp 4044–4098.
- [76] C. Branca, C. Di Blasi, R. Elefante, Devolatilization and Heterogeneous Combustion of Wood Fast Pyrolysis Oils, *Ind. Eng. Chem. Res.* 2005, 44, 799-810.
- [77] J. P. Diebold, S. Czernik, Additives To Lower and Stabilize the Viscosity of Pyrolysis Oils during Storage, *Energy Fuels*, 1997, 11 (5), pp 1081–1091.
- [78] X. Hu, Y. Wang, D. Mourant, R. Gunawan, C. Lievens, W. Chaiwat, M. Gholizadeh, L. Wu, X. Li, C. Li, Polymerization on Heating up of Bio-Oil: A Model Compound Study, March 2013 Vol. 59, No. 3 *AIChE Journal*.
- [79] R. Ginell, R. Simha, On the Kinetics of Polymerization Reactions. I. First Order Initiation Reaction (1), *J. Am. Chem. Soc.*, 1943, 65 (4), pp 706–715.
- [80] X. Bai, P. Johnston, S. Sadula, R. C. Brown, Role of levoglucosan physiochemistry in cellulose pyrolysis, *Journal of Analytical and Applied Pyrolysis* Volume 99, January 2013, Pages 58-65.
- [81] Y. Houminer, S. Patai, Thermal Polymerization of Levoglucosan, *Journal of Polymer Science: Part a1* vol. 7, 3005-3014 (1969).
- [82] J. P. Diebold, A Review of the Chemical and Physical Mechanisms of the Storage Stability of Fast Pyrolysis Bio-Oils, NREL/SR-570-27613, January 2000.
- [83] D. L. Purich, *Enzyme Kinetics: Catalysis and Control: A Reference of Theory and Best-Practice Methods*, Elsevier, 16 Jun 2010, pages 206-207.
- [84] G. Lupo, C. Duwig, A Numerical Study of Ethanol–Water Droplet Evaporation, *Journal of Engineering for Gas Turbines and Power*, Vol. 140/ 021401-1, 2018.
- [85] W. A. Sirignano, FUEL DROPLET VAPORIZATION AND SPRAY COMBUSTION THEORY, *Progress in Energy and Combustion Science*, Vol. 9, pp. 291-322, 1983.
- [86] T. T. B. Nguyen, S. Mitra, M. J. Sathe, V. Pareek, J. B. Joshi, G. M. Evans, Evaporation of a suspended binary mixture droplet in a heated flowing gas stream, *Journal of Experimental Thermal and Fluid Science* 91:329–344, 2018.
- [87] A. Arabkhalaj, A. Azimi, H. Ghassemi, R. S. Markadeh, A fully transient approach on evaporation of multi-component droplets, *Journal of Applied Thermal Engineering* 125:584–595, 2017.
- [88] D. F. Fairbanks, C. R. Wilke, Diffusion Coefficients in Multicomponent Gas Mixtures, *Journal of Industrial and Engineering Chemistry* Vol. 42, No. 3.
- [89] C. L. Yaws, P. K. Narasimhan, *Thermophysical Properties of Chemicals and Hydrocarbons*, ISBN 978-0-8155-1596-8, 2009.

- [90] E. N. Fuller, P. D. Schettler, J. C. Giddings, New method for prediction of binary gas phase diffusion coefficients, *Journal of Industrial and Engineering Chemistry*, 1966, 58 (5), pp 18–27.
- [91] NIST Chemistry WebBook, SRD 69.
- [92] Dortmund Data Bank, September 2018.
- [93] S. Mostafa Ghiaasiaan, *TWO-PHASE FLOW, BOILING AND CONDENSATION IN CONVENTIONAL AND MINIATURE SYSTEMS*, ISBN-13 978-0-521-88276-7, 2008.
- [94] M. Reinhard, A. Drefahl, *Handbook for estimating Physicochemical properties of Organic compounds*, ISBN 0-471-17264-2, 1999.
- [95] R. K. Sinnott, J. M. Coulson, *Chemical Engineering Design*, Volume 6 fourth edition, ISBN 0 7506 6538 6, 2005.
- [96] R.B. Bird, W.E. Stewart, E.N. Lightfoot, *Transport phenomena*. 2nd. New York, 2002.
- [97] Aspen HYSYS V8.4, 2018.
- [98] P. Li, Y. Liang, P. S. Ma, Ch. Zhu, Estimations of enthalpies of vaporization of pure compounds at different temperatures by a corresponding-states group-contribution method, *Fluid Phase Equilibria*, Volume 137, Issues 1–2, November 1997, Pages 63-74 .
- [99] H. An, W. M. Yang, A. Maghbouli, S. K. Chou, K. J. Chua, Detailed physical properties prediction of pure methyl esters for biodiesel combustion modeling, *Applied Energy* Volume 102, February 2013, Pages 647-656.
- [100] R. E. Guedesa, A. S. Lunaa, A. R. Torres, Operating parameters for bio-oil production in biomass pyrolysis: A review, *Journal of Analytical and Applied Pyrolysis* 129 (2018) 134–149.
- [101] A. V. Bridgwater, D. Meier, D. Radlein, An overview of fast pyrolysis of biomass, *Organic Geochemistry* 30 (1999) 1479±1493.
- [102] V. Oja, E. M. Suuberg, Vapor Pressures and Enthalpies of Sublimation of d-Glucose, d-Xylose, Cellobiose, and Levoglucosan, *J. Chem. Eng. Data*, 1999, 44 (1), pp 26–29.
- [103] S. Kelkar, Z. Li, J. Bovee, K. D. Thelen, R. M. Kriegel, C. M. Saffron, Pyrolysis of North-American grass species: Effect of feedstock composition and taxonomy on pyrolysis products, *Biomass and Bioenergy* Volume 64, May 2014, Pages 152-161 .
- [104] J. Yanika, R. Stahl, N. Troeger, A. Sinag, Pyrolysis of algal biomass, *Journal of Analytical and Applied Pyrolysis* 103 (2013) 134–141.
- [105] L. Zhou, B. Wang, X. Peng, X. Du, Y. Yang, On the Specific Heat Capacity of CuO Nanofluid, Hindawi Publishing Corporation *Advances in Mechanical Engineering* Volume 2010, Article ID 172085, 4 pages.
- [106] D. J. Torres, P. J. O'Rourke, A. A. Amsden, Efficient multicomponent fuel algorithm, *Article in Combustion Theory and Modelling*, *Combust. Theory Modelling* 7 (2003) 67–86.

